Probing the Spin Dimensionality in Single-Layer CrSBr Van Der Waals Heterostructures by Magneto-Transport Measurements

Carla Boix-Constant, Samuel Mañas-Valero,* Alberto M. Ruiz, Andrey Rybakov, Krzysztof Aleksander Konieczny, Sébastien Pillet, José J. Baldoví, and Eugenio Coronado*

Supplementary Information
Probing the spin dimensionality in single-layer CrSBr van der Waals heterostructures by magneto-transport measurements

Carla Boix-Constant,[a] Samuel Mañas-Valero,[a] Alberto M. Ruiz,[a] Andrey Rybakov,[a] Krzysztof Aleksander Konieczny,[b] Sébastien Pillet,[b] José J. Baldoví,[a] Eugenio Coronado.[a*]*

[a] Instituto de Ciencia Molecular (ICMol), Universitat de València, Catedrático José Beltrán 2, Paterna 46980, Spain.

[b] Université de Lorraine, CNRS, CRM2, 54500 Nancy, France.

e-mail: samuel.manas@uv.es, eugenio.coronado@uv.es

This file contains the following sections:

1. Crystal growth and bulk characterization.

1.1. Synthesis and powder characterization.

High quality CrSBr crystals were synthesized by chemical vapor transport (CVT) and characterized by powder crystal X-Ray diffraction, energy dispersive X-Ray analysis (EDX), high-resolution TEM, SQUID magnetometry and temperature-dependent single crystal. The crystals were prepared by direct reaction of their components in a stoichiometric ratio, mixing chromium (99.99 %, Alfa-Aesar), sulfur (99.99 %, Sigma-Aldrich) and bromine (99.9 %, Sigma-Aldrich), with a 3 % in mass excess of bromine, which acts as a transport agent.[1] They were sealed in an evacuated quartz ampoule (length: 250 cm, internal diameter: 14 mm; P: 2×10^{-5} mbar) and heated from room temperature to 700 °C in 6 h. The obtained material was placed in a three-zone furnace, stablishing a 940 °C/800 °C gradient in 12 hours and kept for one week. As a result, we obtained black, needle-like crystals.

The weight concentration of elements obtained by EDX was Cr: (31.6 ± 0.3) %, S: (19.3 ± 0.3) % and Br: (49.1 ± 0.4) %. These values are in good agreement with the expected ones (Cr: 31.7 %, S: 19.6 % and Br: 48.8 %). Phase purity was confirmed by the refinement of the X-ray pattern (measured with a PANalytical Empyrean Xray platform with Cu radiation source) to the previously reported structure of CrSBr (ICSD 69659) using the X´Pert Highscore Plus program. The orthorhombic crystal system with a Pmmnz space group was obtained and the unit cell was determined to be α = β = γ = 90°, a = 3.512(2) Å, b = 4.762(1) Å and c = 7.962(1) Å.
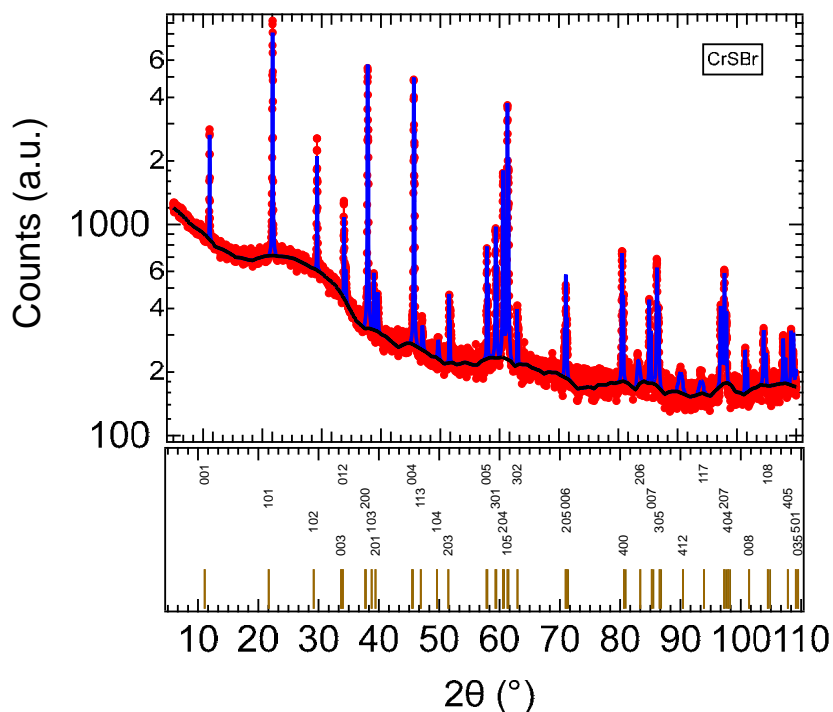

Figure S.1.- Experimental X-ray powder diffraction pattern (red) and corresponding fit (peaks in blue and background in black) for CrSBr.

1.2.   Single-crystal X-Ray diffraction and IR as a function of temperature.

Single crystal X-ray diffraction measurements were performed as a function of temperature in the 10-75K range using a Microfocus Supernova diffractometer (Mo Kα radiation, λ = 0.71073 Å) equipped with a two dimensional ATLAS detector, and a Helijet He open flow cryosystem. A needle shape single crystal sample was cut from a very large single crystal. Unit cell parameters were determined from 10 K to 75 K (5 K step), while complete data collection for structural determination and analysis was performed at 10K and 75K. Analytical absorption corrections were applied. Initial structural models were based on those proposed by Beck,[2] and refined using full matrix least squares on F^2 using OLEX.[3] The corresponding CIF files can be retrieved from Cambridge Structural Database (CSD) (deposition numbers: CCDC 2161029 & 2161030).

All IR measurements were performed using a Nicolet 5700 FT-IR spectrometer equipped with a He closed-cycle cryostat. The sample was grinded, mixed with polyethylene powder, pressed into pellets, and glued to the cold-finger of the cryostat using silver-paste thermal adhesive. Measurements were carried out as a function of temperature from 300K to 10K in the 50-1000 cm^{-1} wavenumber range.

CrSBr crystallizes in the structure type FeOCl,[2,4,5] which is adopted by the isostructural compounds MOX (M = Ti, V, Cr, Fe ; X = Cl, Br), in the orthorhombic space group Pmmn with two formula units per unit cell.[6–9] The whole family of MOX compounds exhibit magnetic transitions, which are accompanied by lattice and structural distortions owing to magnetoelastic coupling, evidenced by single crystal or powder X-ray diffraction. In TiOCl and TiOBr, a spin-Peierls transition inducing a lowering of symmetry from orthorhombic to monoclinic has been detected by the development of twofold superstructure reflections below T_c, indicating a dimerization of the Ti chain.[8] The lowering of the point symmetry was revealed by a splitting of reflections. A similar monoclinic distortion has also been characterized for CrOCl,[9] VOCl[7] and FeOCl.[6]

In order to correlate the electronic and magnetic behavior of CrSBr and its magneto-electric anisotropy to a possible underlying structural phase transition, the crystal structure and infrared spectra has been monitored as a function of temperature below 75 K using single crystal X-ray diffraction. Contrary to TiOCl, no superstructure reflections were detected in the reconstruction of the reciprocal lattice, ruling out any phase transition of the spin-Peierls type. Complete crystal structures have been determined and refined at T = 10 K and T = 75 K. No symmetry change, and especially no symmetry lowering to monoclinic is observed contrary to the monoclinic distortions characterized for the MOX compounds. The corresponding structures can be described both in the Pmmn space group. The distortion of the CrS_4Br_2 octahedra is preserved while lowering the temperature. This structural analysis is in agreement with the

3

structures reported at 15 K and 50 K by Telford *et al.*[4] and the powder X-ray crystallography results of Lopez-Paz *et al.*[10] The reciprocal space was reconstructed at all temperatures, in order to detect a subtle monoclinic distortion. Still, no splitting of the Bragg reflections was evidenced. The infrared spectrum of CrSBr was as well monitored as a function of temperature. The vibrational absorption bands at 265 cm^{-1} and 322 cm^{-1} do not experience any significant shift, intensity change or splitting upon temperature lowering from 90 K to 10 K. This result further strengthens the idea that no structural phase transition occurs in that temperature range.

Table S.1.- Selected X-ray data collection, processing and refinement parameters for all presented crystal structures.

Data set	10 K	75 K
Moiety formula	CrSBr	
Moiety formula mass	163.97	
Crystal system	Orthorhombic	
Space group	Pmmn (no. 59)	
Z	2	
F_{000}	150	
Crystal size / mm^3	0.17×0.28×0.72	0.17×0.28×0.72
a / Å	3.5035(6)	3.5116(7)
b / Å	4.7375(11)	4.7478(9)
c / Å	7.8968(16)	7.9134(13)
V / Å^3	131.07(5)	131.94(4)
d_{calc} / g·cm^{-3}	4.155	4.127
θ range	2.58° − 30.44 °	2.68° − 32.58°
Absorption coefficient, μ / mm^{-1}	20.006	19.875
No. of reflections collected / unique	1591 / 252	1509 / 253
R_{int}	0.1299	0.1417
No. of reflections with I > 2σ(I)	222	229
No. of parameters / restraints / constraints	13 / 0 / 0	13 / 0 / 0
R[F] (I > 2σ(I))	0.0476	0.0512
R[F] (all data)	0.0497	0.0531
WR[F] (I > 2σ(I))	0.1276	0.1272
WR[F] (all data)	0.1289	0.1257
$\varrho_{res}^{min/max}$ / e·Å^{-3}	−1.88 / +2.78	−2.25 / +2.92

Table S.2.- Selected bond distances (Å) and angles (°).

Data set	10 K	75 K
Distances		
Cr-S	2.383 (2)	2.389 (2)
Cr-S	2.4038 (7)	2.4084 (7)
Cr-Br	2.4863 (12)	2.4909 (12)
Intra-chain Cr…Cr	3.503	3.512
Inter-chain Cr…Cr	3.575	3.581
Angles		
S-Cr-S	160.40 (14)	160.57 (14)
Cr-S-Cr	160.40 (14)	160.57 (14)
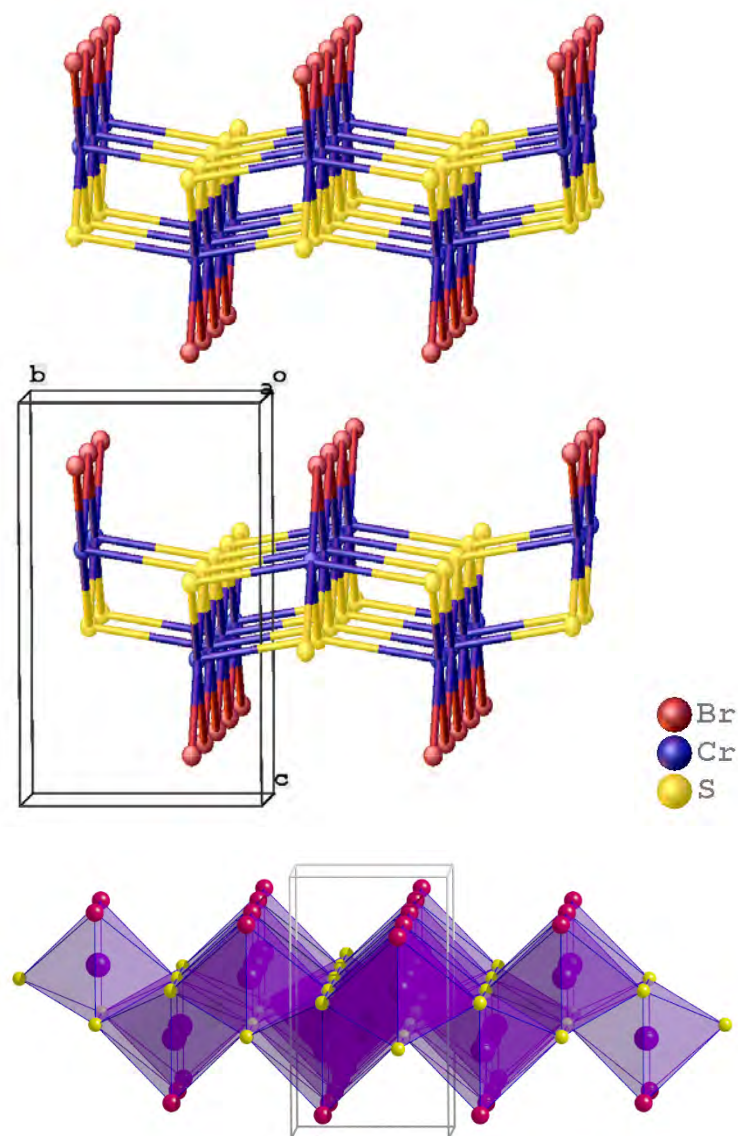
**Figure S.2.-** Projection of the crystal structure of CrSBr along the crystallographic a direction.
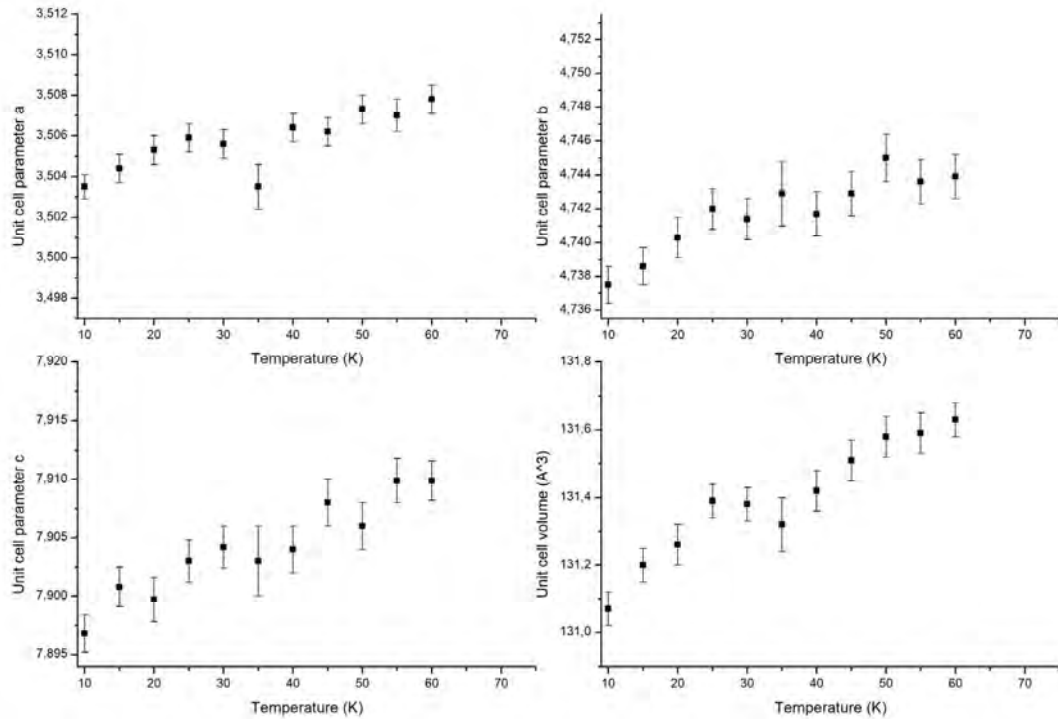
Figure S.3.- Evolution of the unit cell parameters as a function of temperature, determined from single crystal X-ray diffraction.
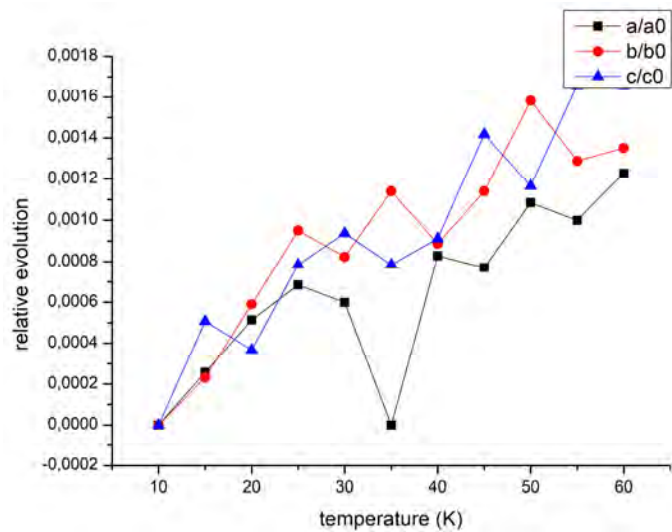
Figure S.4.- Relative evolution ($\Delta L/L$) of the unit cell parameters as a function of temperature.
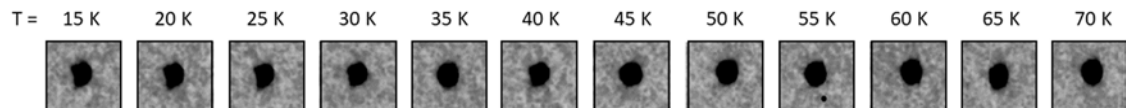
Figure S.5.- Reconstruction of the reciprocal space around the (130) reflection as a function of temperature.

6
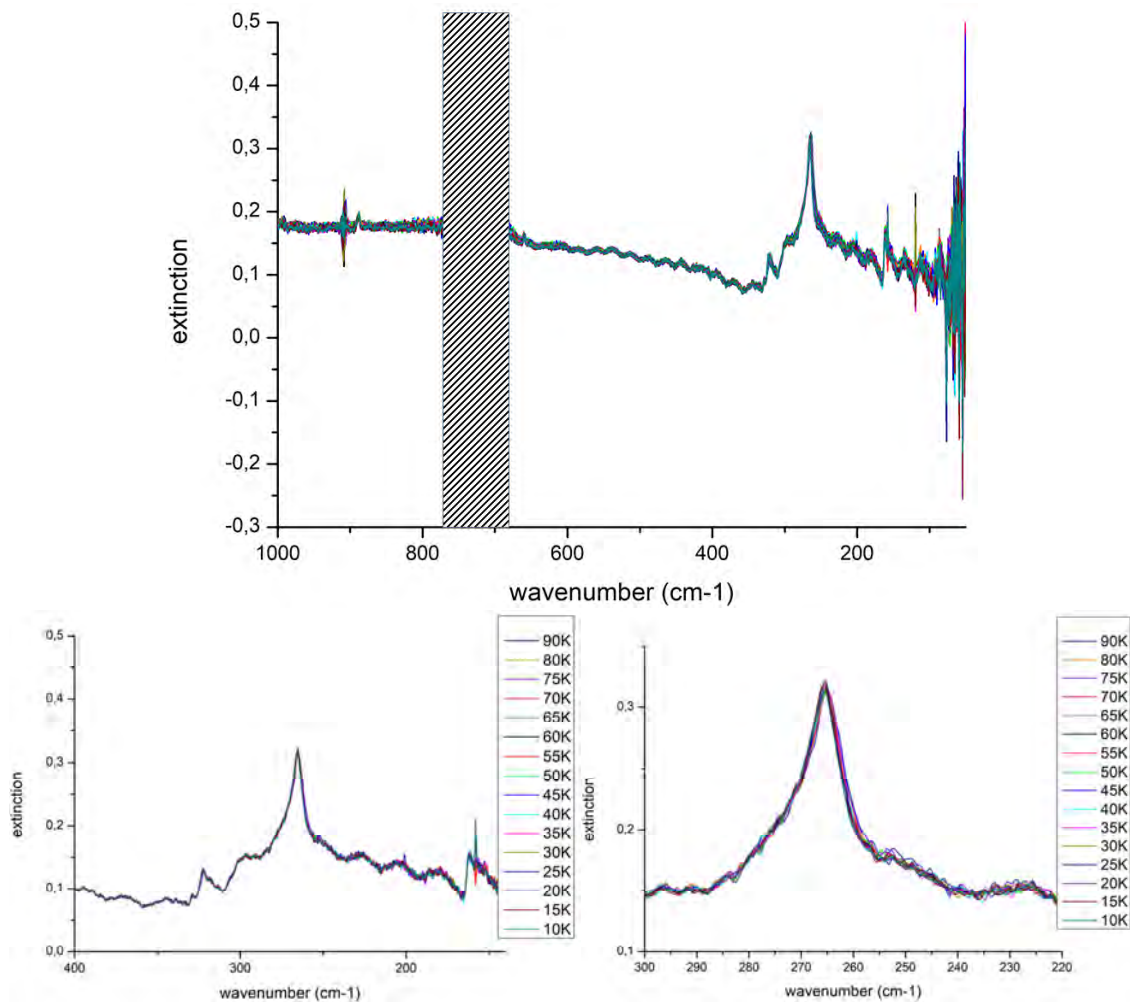
Figure S.6.- IR spectra in the 50-100 cm^{-1} wavenumber range as a function of temperature (from 150 K to 10 K). The excluded shaded area corresponds to strong IR absorption from polyethylene. The 50-100 cm^{-1} range is very noisy, at the detection limit of the spectrometer.

7

1.3.   Transmission electron microscopy.

Mechanically exfoliated flakes of CrSBr were transfered to silicon nitride grids and inspected by transmission electron microscopy, corroborating the structural and elemental composition of the material by atomic-resolution imaging, selected area electron diffraction patterns and energy-dispersive X-Ray spectroscopy. In this elongated cane-shaped flakes, the *a* (*b*) axis corresponds to the long (short) direction.

TEM images and diffraction patterns were acquired with a JEOL JEM-2100F with a field-emission gun operating at 200 kV. Simulated SAED patterns were generated with SingleCrystal software.
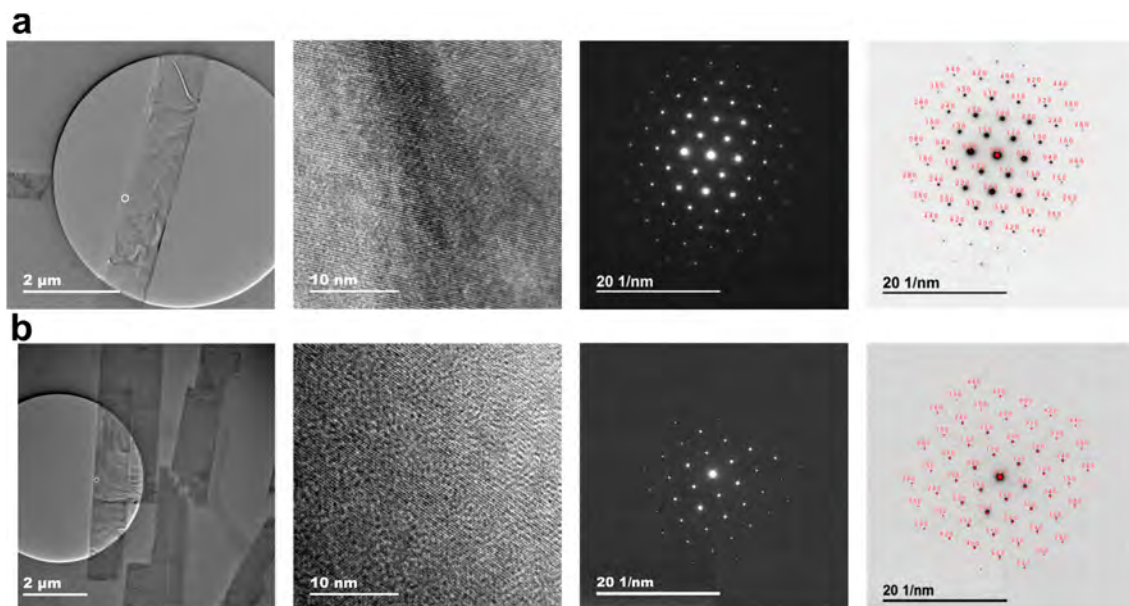
Figure S.7.- TEM characterization of CrSBr flakes: general view (the white circle enclosed the selected area), high-resolution view, selected area electron diffraction pattern and corresponding assignment of the reflections.

2. Optical characterization.

2.1. Experimental framework and discussion.

The optical contrast is a widely used technique in the field of two-dimensional (2D) materials that allows the fast identification of flakes with different thicknesses, being of great importance for air unstable materials, such as 1T-TaS$_2$ or CrI$_3$.[11,12] Taking into account the Fresnel framework,[11] the optical contrast depends on the incident wavelength, the refraction index and thickness of the layers.

As reported for other 2D materials, the optical contrast can be quantified in order to identify the thickness and crystallographic orientation of the exfoliated flake. Here, we consider thin-layers of CrSBr on top of 285 nm SiO$_2$/Si substrates. We define the optical contrast as:[11]

$$C\,(\lambda) = \frac{I_{flake} - I_{subtrate}}{I_{flake} + I_{subtrate}}$$

Thus, the optical contrast can be calculated from optical microscopy images: the I_{flake} value is obtained by selecting a region of interest in an RGB image and averaging its intensity. The same procedure follows for $I_{subtrate}$.

Once the contrast of a flake is determined, its thickness is measured by means of atomic force microscopy analysis (**Supplementary Section 2.2**) and corroborated by Raman spectroscopy (**Supplementary Section 2.3**). Hence, a calibration curve can be obtained relating the optical contrast and the thickness of CrSBr flakes (**Supplementary Section 2.4**).

We observe that atomically-thin layers of CrSBr on top of 285 nm SiO$_2$/Si substrates exhibit optimal contrast values under light illumination of 550 nm and 600 nm. For thickness below 10 nm, the number of CrSBr layers (N) can be determined by (**Supplementary Section 2.4**):

$$C(N)_{550\,nm} = -(0.048 \pm 0.002) \cdot N - (0.036 \pm 0.009)$$
$$C(N)_{600\,nm} = -(0.0480 \pm 0.0010) \cdot N + (0.007 \pm 0.006)$$

In addition, due to the highly anisotropic crystal structure of CrSBr, the crystallographic *a* and *b* axis can be determined by measuring the optical contrast (**Supplementary Section 2.6**) or the Raman spectrum (**Supplementary Section 2.5**) with linear polarized light, confirming the crystal orientation obtained by transmission electron microscopy (**Supplementary Section 1.3**).

2.2. Examples of experimental optical contrast of CrSBr thin-layers on 285 nm SiO₂/Si substrate.
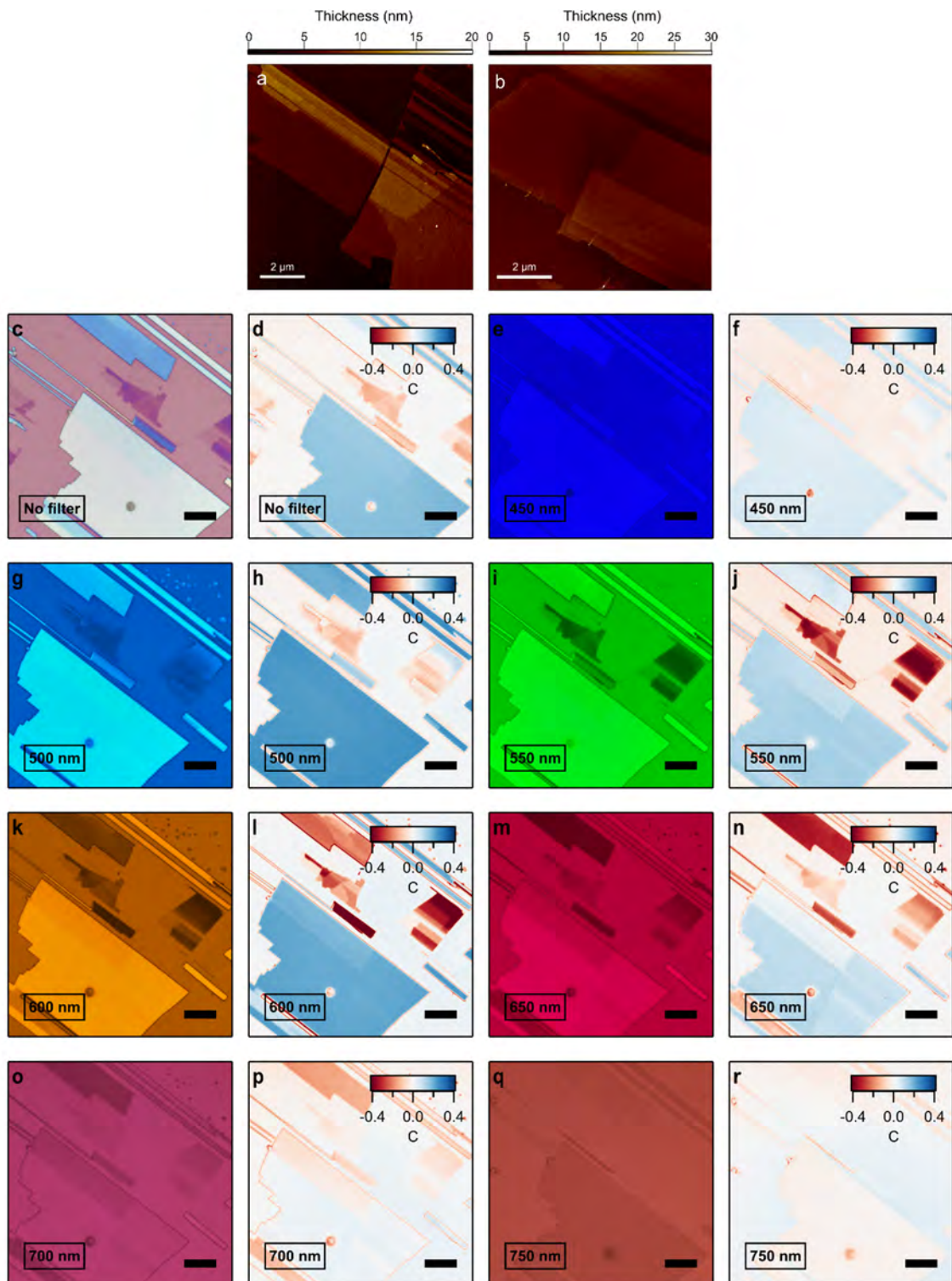

Figure S.8.- Experimental optical contrast of CrSBr thin-layers: atomic force microscopy image of the flakes (panels a and b), optical microscopy image without filter (panel c) and with filters (panels e, g, i, k, m, o and q) and the corresponding experimental optical contrast (panels d, f, h, j, l, n, p and r). Scale bar in contrast images: 10 μm.
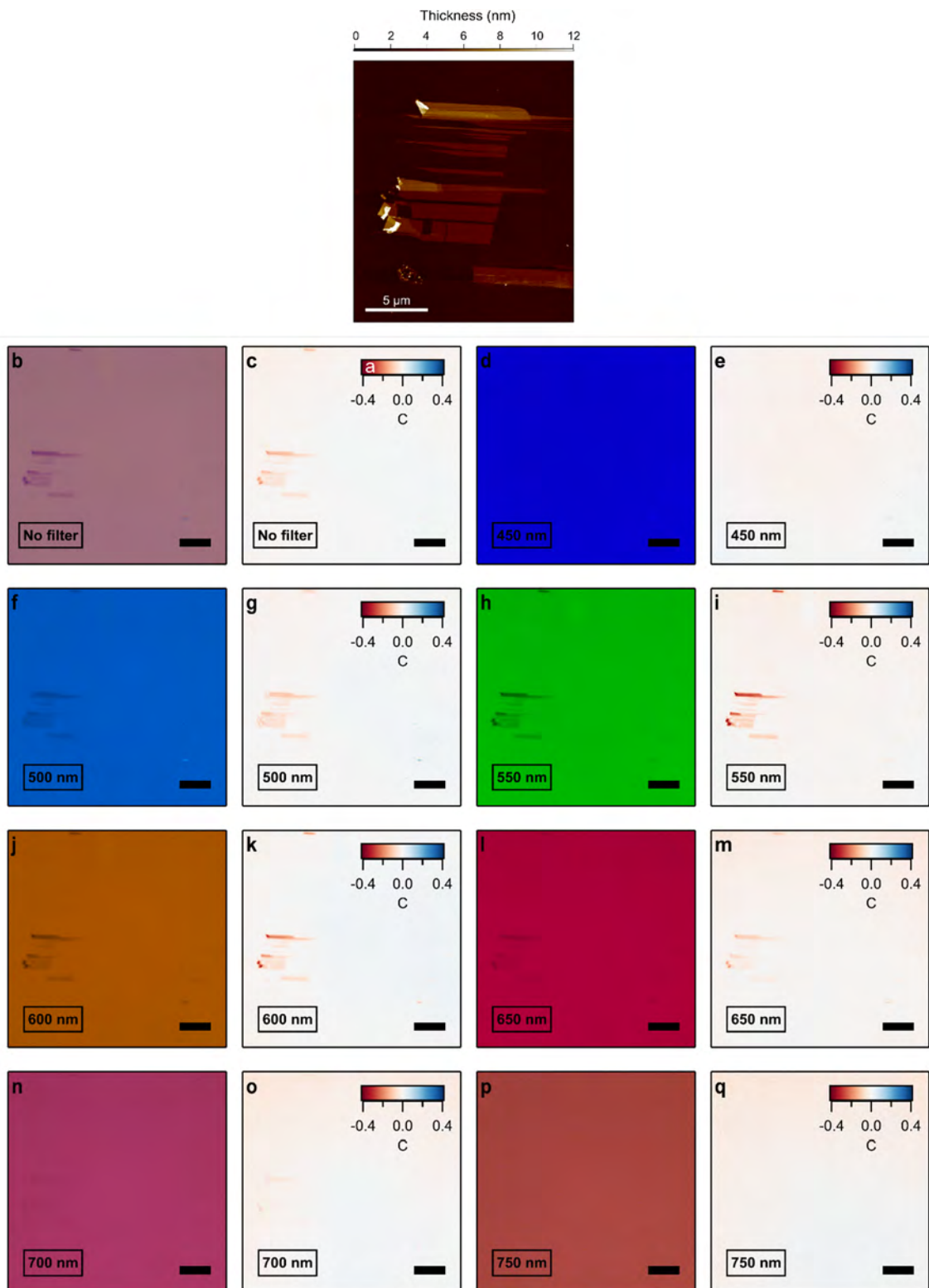
Figure S.9.- Experimental optical contrast of CrSBr thin-layers: atomic force microscopy image of the flakes (panel a), optical microscopy image without filter (panel b) and with filters (panels d, f, h, j, l, n and p). and the corresponding experimental optical contrast (panels c, e, g, i, k, m, o and q). Scale bar in contrast images: 10 μm.
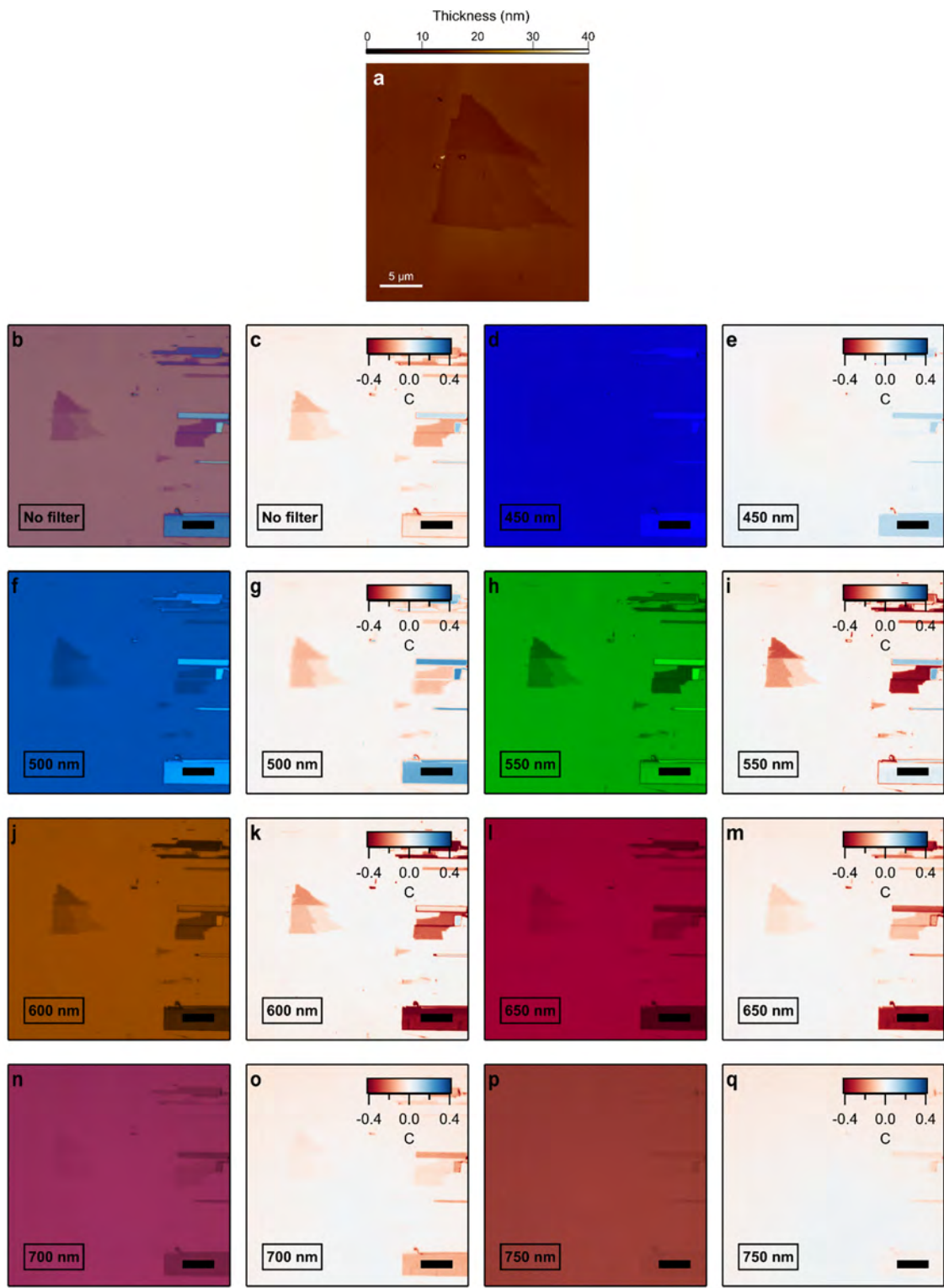
Figure S.10.- Experimental optical contrast of CrSBr thin-layers: atomic force microscopy image of the flakes (panel a), optical microscopy image without filter (panel b) and with filters (panels d, f, h, j, l, n and p). and the corresponding experimental optical contrast (panels c, e, g, i, k, m, o and q). Scale bar in contrast images: 10 μm.

2.3.   Layer dependence of the CrSBr Raman spectra.
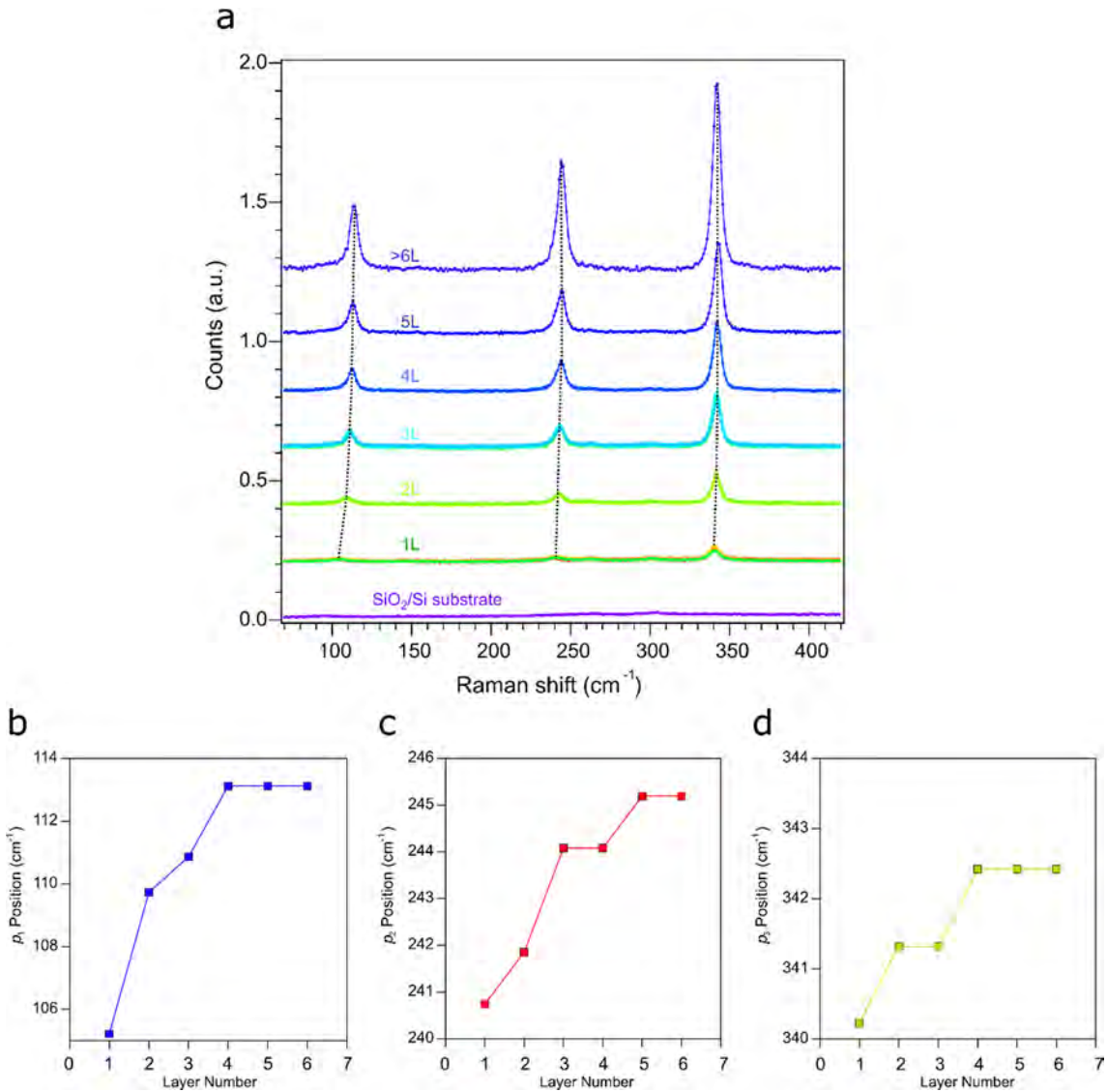
Figure S.11.- Identification of the Raman peaks corresponding to the CrSBr for flakes with different number of layers. Panel a shows the main peaks of intensity for the CrSBr and the SiO_2/Si substrate spectra. For clarity, and offset of 0.2 has been added. Panels b-d show the displacement of the peaks' position as the number of layers increases. Our results are in agreement with Telford *et al.*[13]

2.4. CrSBr optical contrast vs. number of layers for different incident wavelengths.
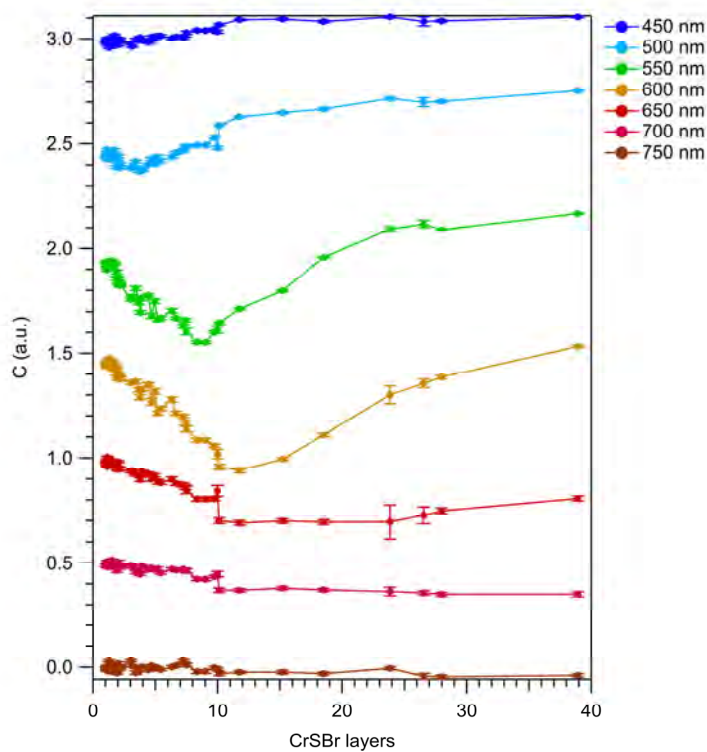
Figure S.12.- Experimental optical contrast points and the corresponding light filters. For clarity, it has been added a vertical offset of 0.5.
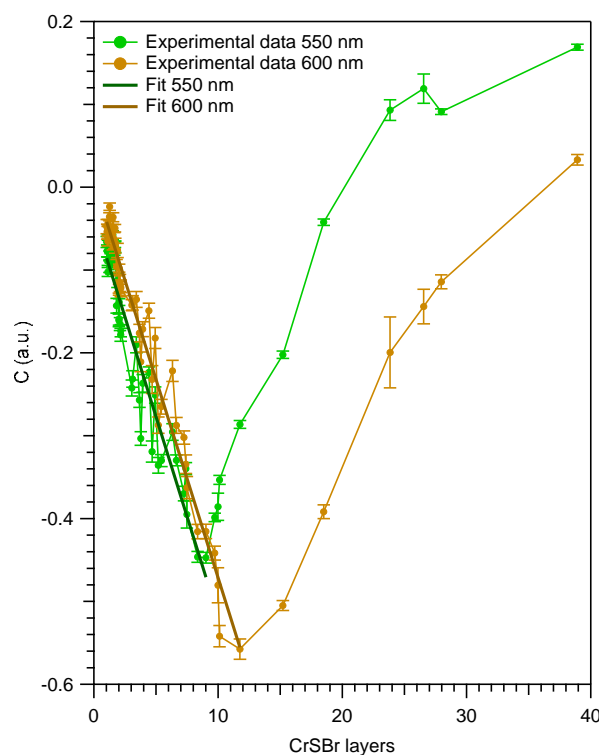
Figure S.13.- Linear fit of the experimental points obtained under = 550 nm and λ = 600 nm light filters.

2.5. CrSBr optical contrast dependence with incident polarized light.
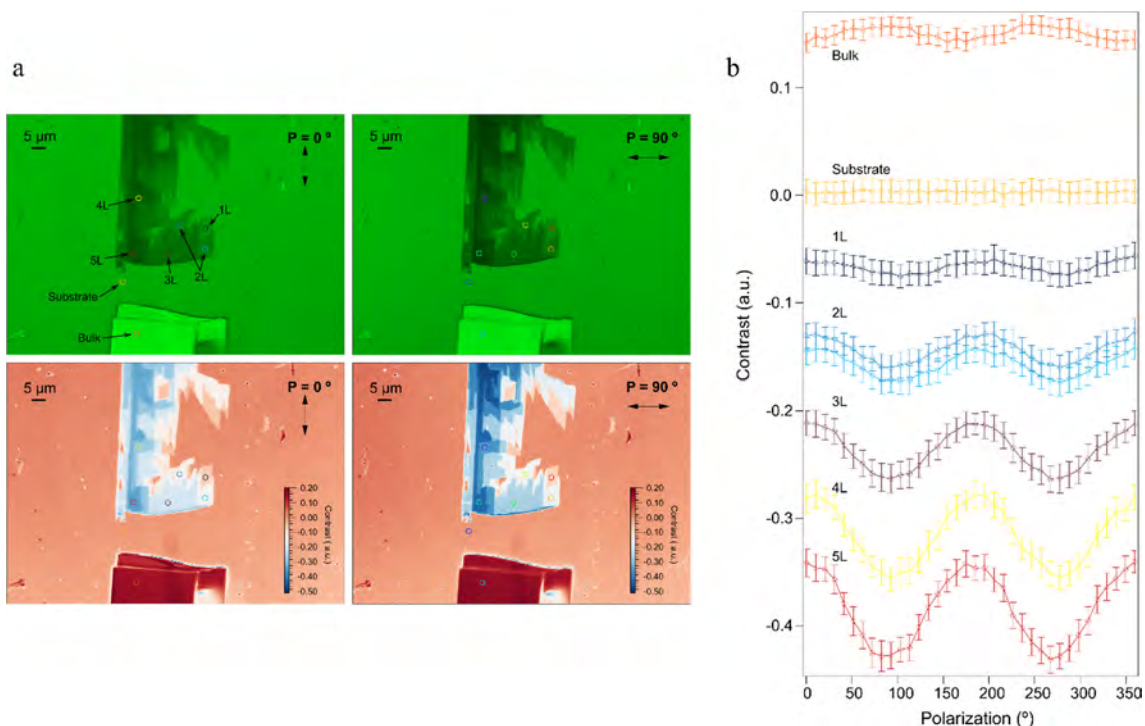
Figure S.14.- Contrast dependence of a CrSBr multilayer crystal using lineal polarized light under $\lambda = 550$ nm light filter. The anisotropy of the material leads to a maximum or a minimum in the contrast value when the polarized incident light is parallel to the *a* axis or the *b* axis, respectively.

2.6.   Light polarization dependence of the CrSBr Raman spectra.
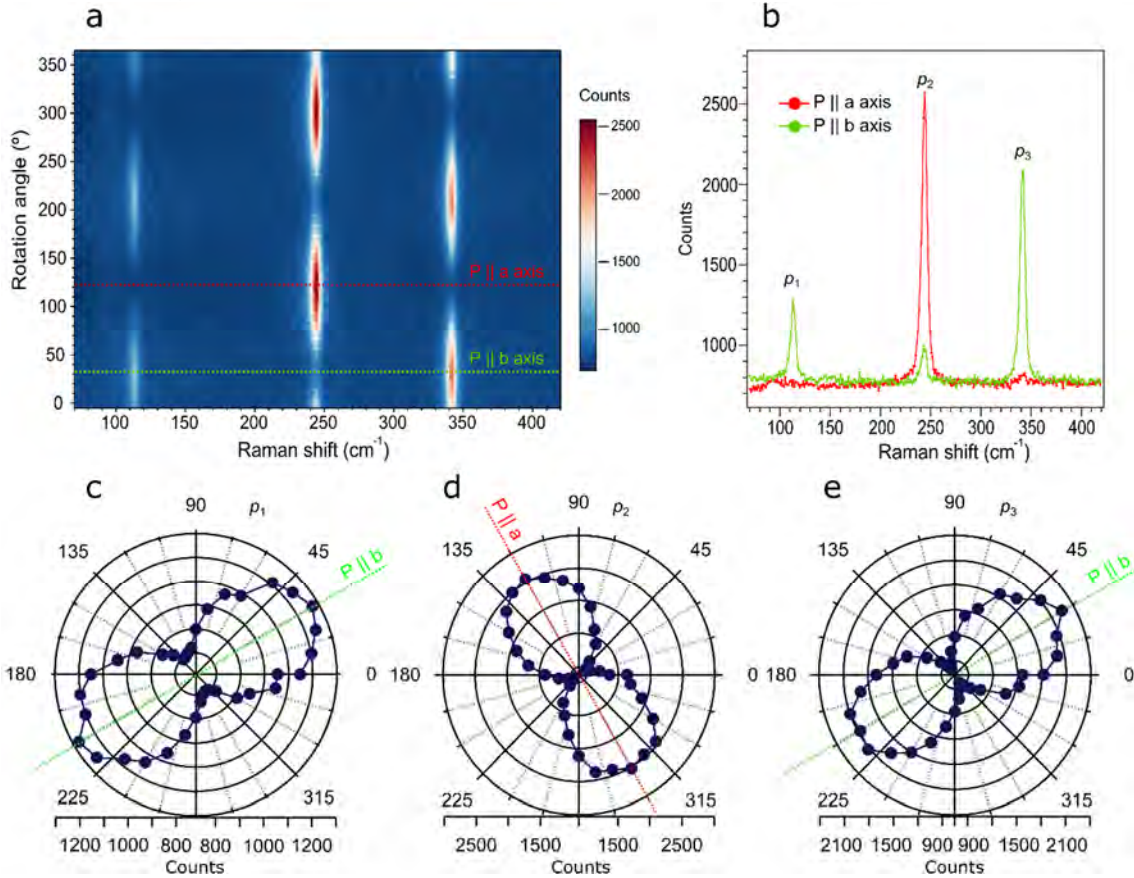
Figure S.15.- Raman spectra dependence on the polarization of the incident light. Panel a shows a 2D plot of the spectra as a function of the rotation angle. The red and the green-dashed lines represent the incident polarized light when it is parallel to the a axis and the b axis, respectively. Panels b-e show the evolution of the main peaks of the spectra as a function of the angle of polarization. The 90º difference between the maximum intensity of peaks P_1 and P_3, and P_2 is due to the high anisotropy of the material.

3. Magnetotransport measurements.

3.1. Summary table of the fabricated devices.

A total of 13 devices were fabricated following the same procedure as explained in the Methods section. In **Table S.3** we present a summary of the CrSBr-based devices, together with the experimental optical contrast calculated using a filter of 550 nm, the number of layers that are deduced from the calibration curve of the optical contrast for this material and the area of the junction for each device.

Table S.3.- Summary of the fabricated devices with the experimental contrast value, estimated number of layers and area of the junction barrier.

Device	CrSBr barrier		
	Optical contrast (a.u.)	Layers	Area (μm^2)
A.1. (FLG/CrSBr/FLG)	-0.075 ± 0.011	1	1.89
A.2. (FLG/CrSBr/FLG)	-0.077 ± 0.011	1	6.52
A.3. (FLG/CrSBr/FLG)	-0.077 ± 0.012	1	31.02
A.4. (FLG /CrSBr/ FLG)	-0.065 ± 0.011	1	4.10
A.5. (NbSe$_2$/CrSBr/ NbSe$_2$)	-0.076 ± 0.012	1	12.53
A.6. (TaS$_2$/CrSBr/TaS$_2$)	-0.087 ± 0.012	1	4.23
B.1. (FLG/CrSBr/FLG)	-0.152 ± 0.012	2	3.35
B.2. (FLG/CrSBr/FLG)	-0.159 ± 0.013	2	8.45
B.3. (FLG/CrSBr/FLG)	-0.157 ± 0.013	2	13.61
B.4. (FLG/CrSBr/FLG)	-0.157 ± 0.012	2	4.59
B.5. (FLG/CrSBr/FLG)	-0.152 ± 0.013	2	13.04
B.6. (NbSe$_2$/CrSBr/ NbSe$_2$)	-0.167 ± 0.013	2	17.10
B.7. (NbSe$_2$/CrSBr/ NbSe$_2$)	-0.151 ± 0.013	2	14.81
C.1. (FLG/CrSBr/FLG)	-0.180 ± 0.013	3	7.80

3.2. Comparison of the temperature dependence with reported horizontal devices.

In the horizontal devices previously reported by Telford *et al.*[13] and Wu *et al.*[14], there is a decrease in conductance in the 300 K - 200 K range followed by a metallic regime until ca. 130 K and a final crossover to a semiconducting/insulating phase. In addition, the MR exhibits opposite trends at low temperatures when the current is applied along the a or b crystallographic axis.[14] In contrast, in the present vertical geometry, both bilayer and monolayer exhibit similar behaviors characterized by a smooth increase in the resistance upon cooling down followed by a more pronounced enhancement at low temperatures (below T*), following the same trend when the current is applied along the a or b axis (see **Supplementary Section 3.3**). This supports sensing the out-of-plane component (c axis), as already reported for other vertical van der Waals heterostructures.[11,15,16]
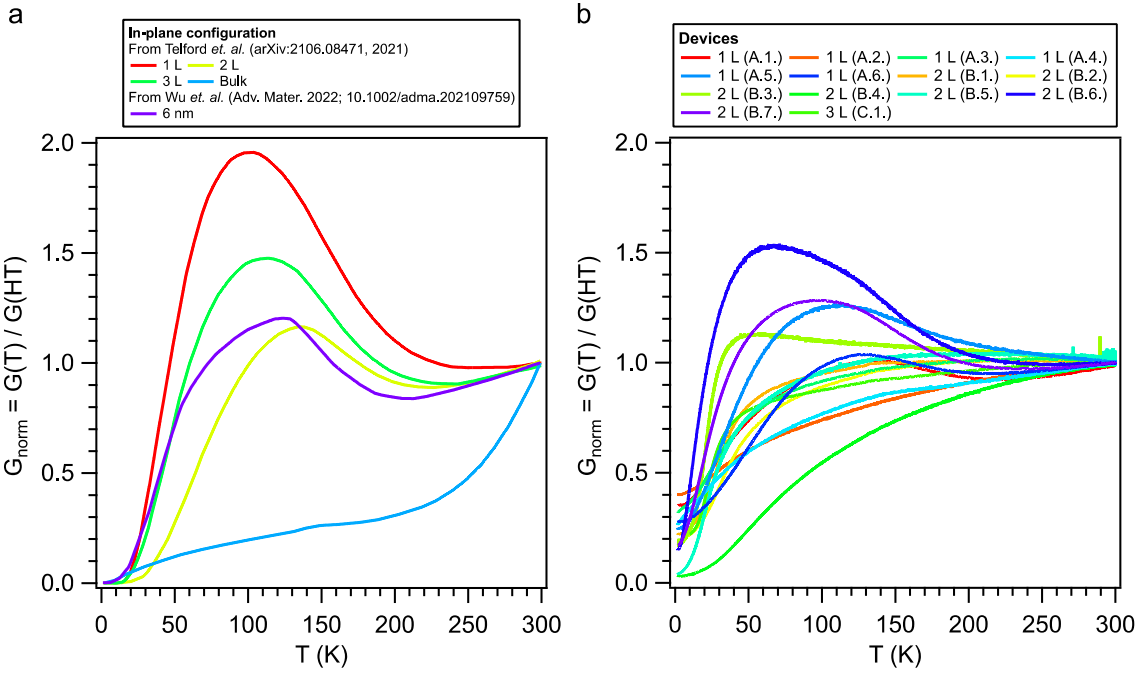
Figure S.16.- Comparative of in-plane (data from Telford *et. al.*[13] and Wu *et. al.*[14]) and out-of-plane (this work) transport measurements on CrSBr atomically thin layers.
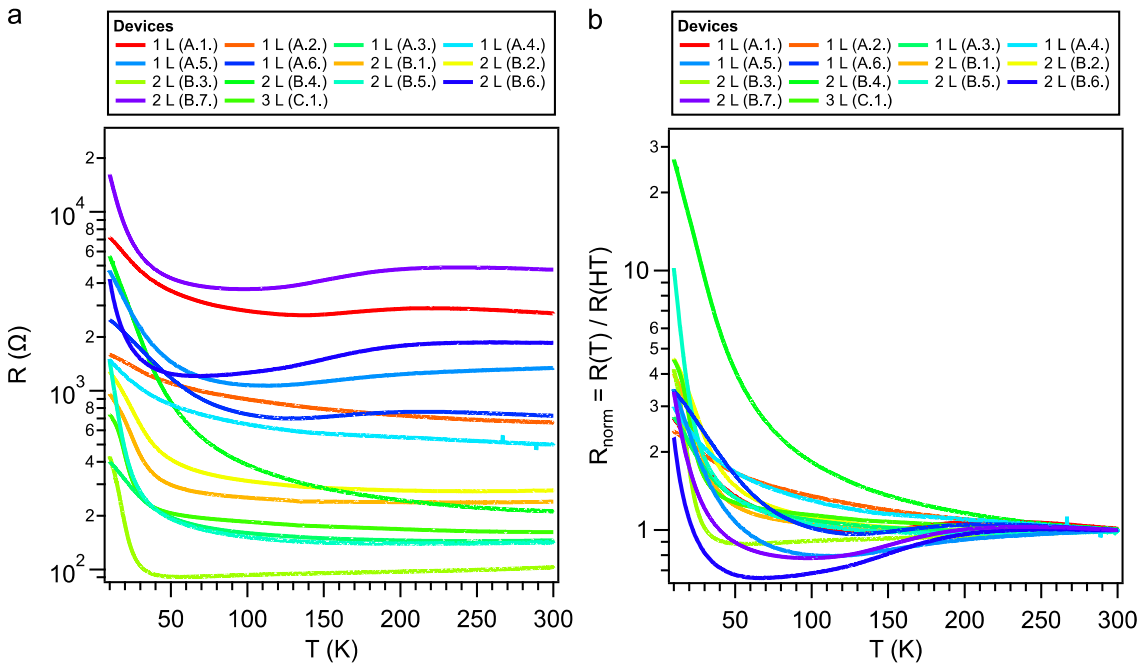
Figure S.17.- a) Resistance and b) normalized resistance for the vertical devices studied in this work.

3.3. Comparison of the magneto-resistance depending on the current direction with respect to the flake orientation.
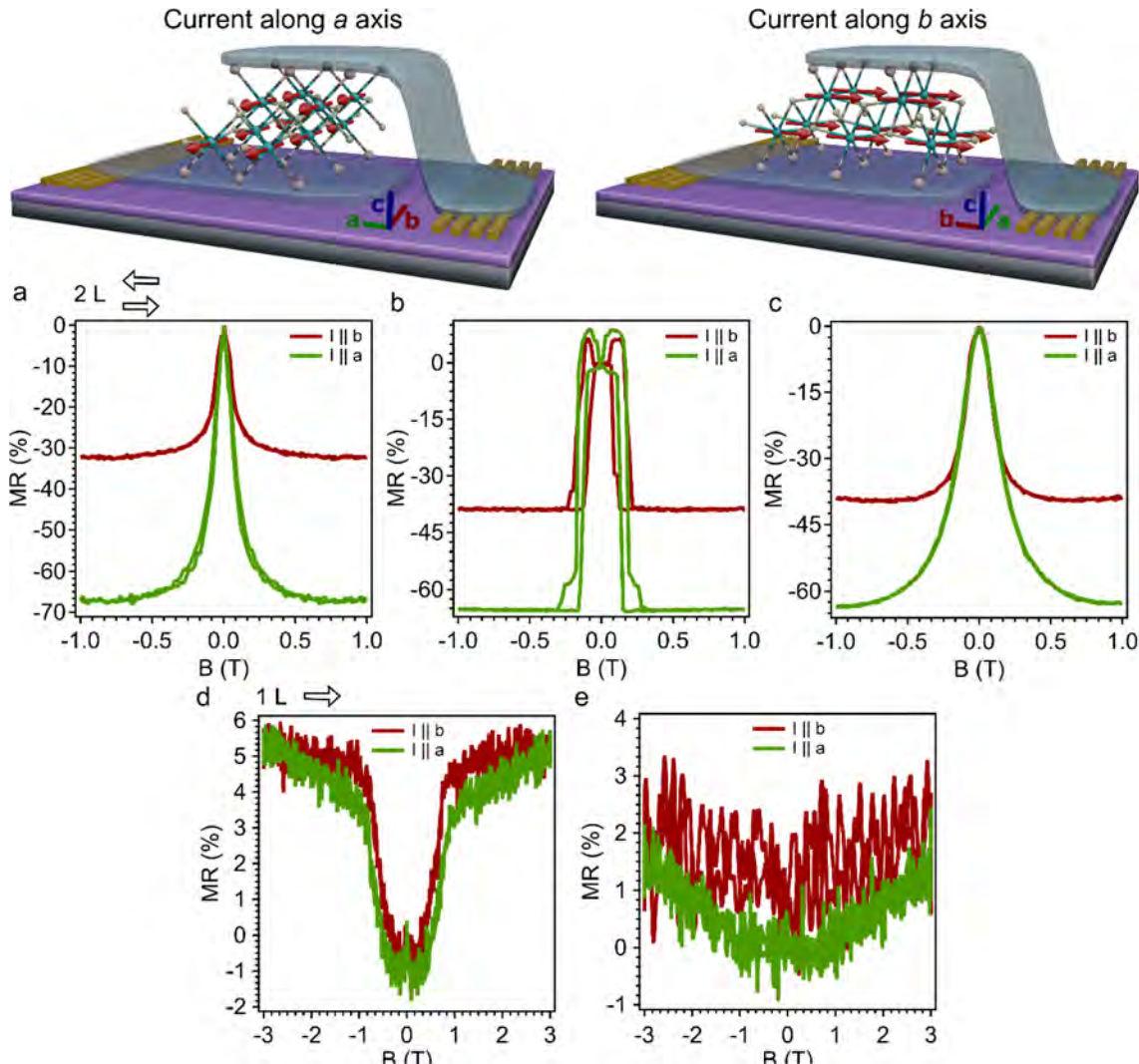

Figure S.18.- Sketch (not to scale) of devices where the CrSBr flakes are oriented in both directions. Magnetoresistance at 10 K for samples where the current is parallel to the main axis when the field is parallel to a) *a* axis, b) *b* axis and c) *c* axis for the bilayer case (device B.4 and device B.5 for the current parallel to *b* and *a*, respectively) and when the field is parallel to d) *a* axis, e) *b* axis for the monolayer case (device A.1 and device A.4 for the current parallel to *b* and *a*, respectively).

3.4. Measured devices.

3.4.1. Device A.1. (CrSBr monolayer).
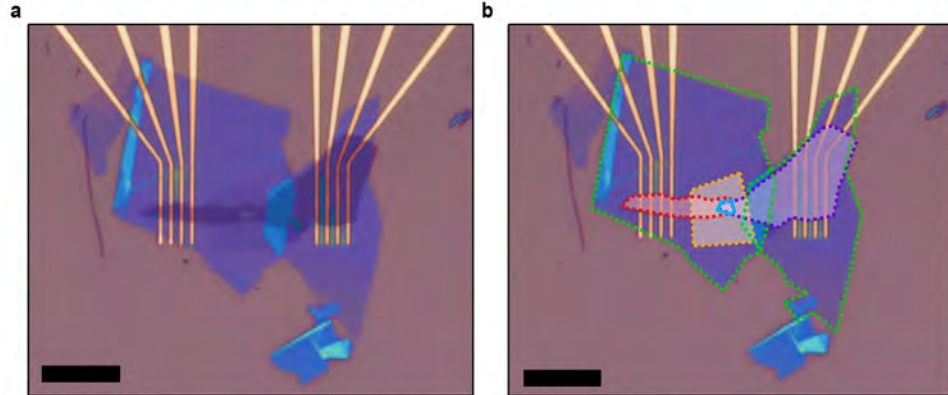
Figure S.19.- Optical picture of the device. For simplicity, the top graphite contact has been highlighted in red, the bottom graphite contact in purple and the CrSBr barrier in orange. h-BN is marked in green. The junction (blue area) is the overlapped area formed by the three different materials. Scale bar: 10 μm.
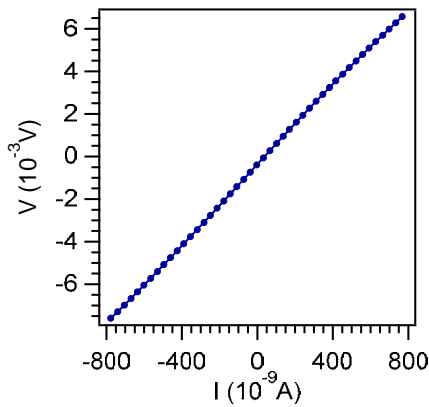
Figure S.20.- DC IV curve for the junction area at 10 K.
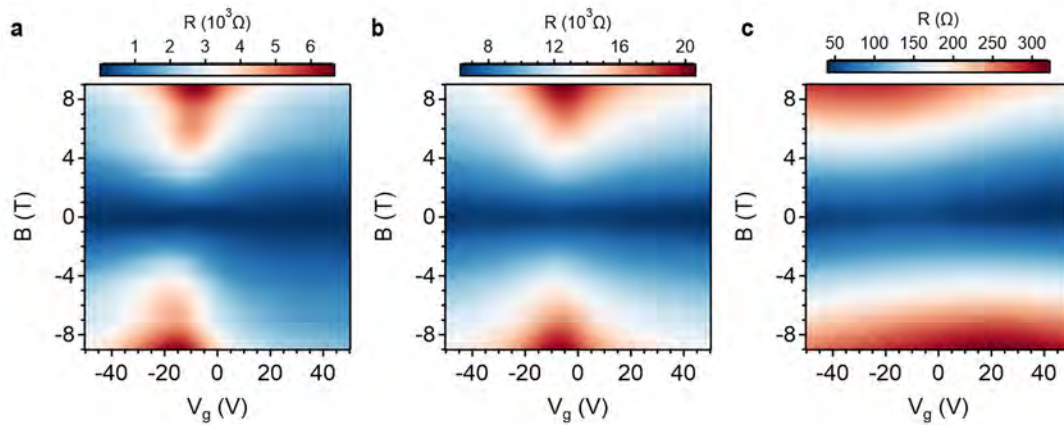
Figure S.21.- Field dependence of the resistance as a function of the gate voltage at 10 K for the top contact (a), the junction (b) and the bottom contact (c). Field parallel to the c axis.
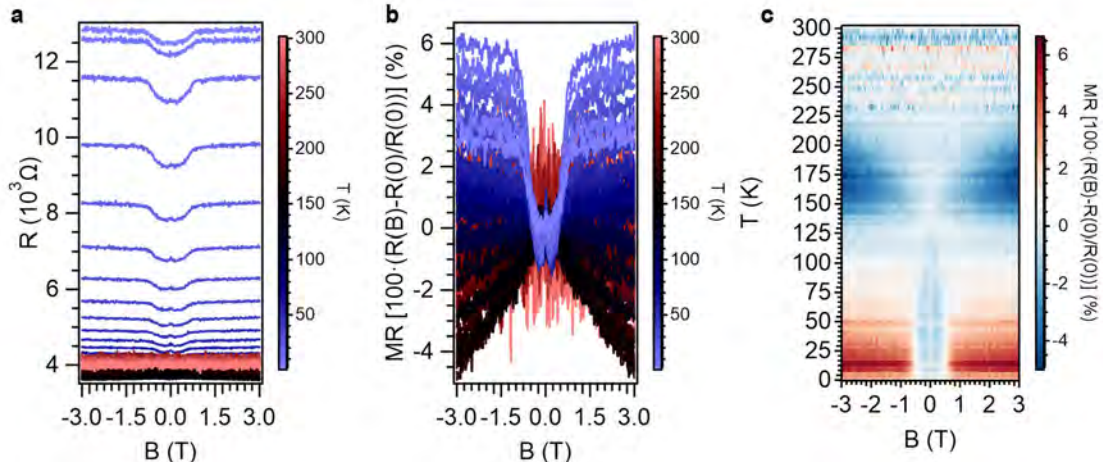
Figure S.22.- a) Resistance as a function of the magnetic field for different temperatures. b) Calculated magnetoresistance as a function of the magnetic field for different temperatures. c) Resistance plot as a function of temperature and magnetic field. M Field parallel to the a axis.
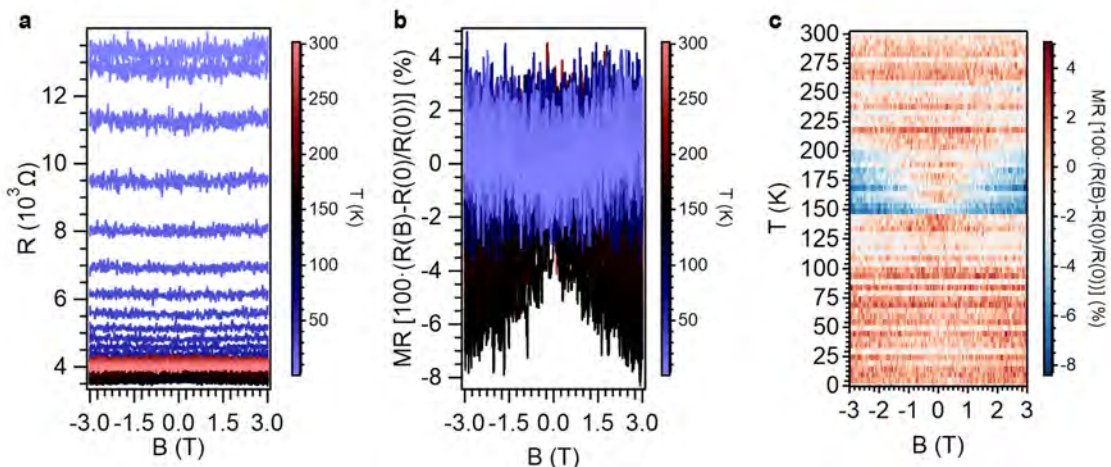
Figure S.23.- a) Resistance as a function of the magnetic field for different temperatures. b) Calculated magnetoresistance as a function of the magnetic field for different temperatures. c) Resistance plot as a function of temperature and magnetic field. Field parallel to the b axis.
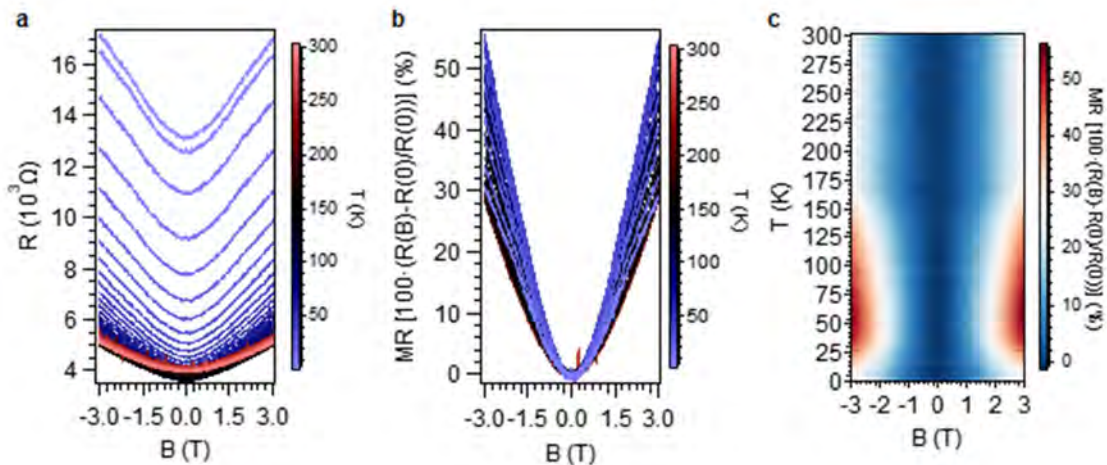
Figure S.24.- a) Resistance as a function of the magnetic field for different temperatures. b) Calculated magnetoresistance as a function of the magnetic field for different temperatures. c) Resistance plot as a function of temperature and magnetic field. Field parallel to the c axis.

21
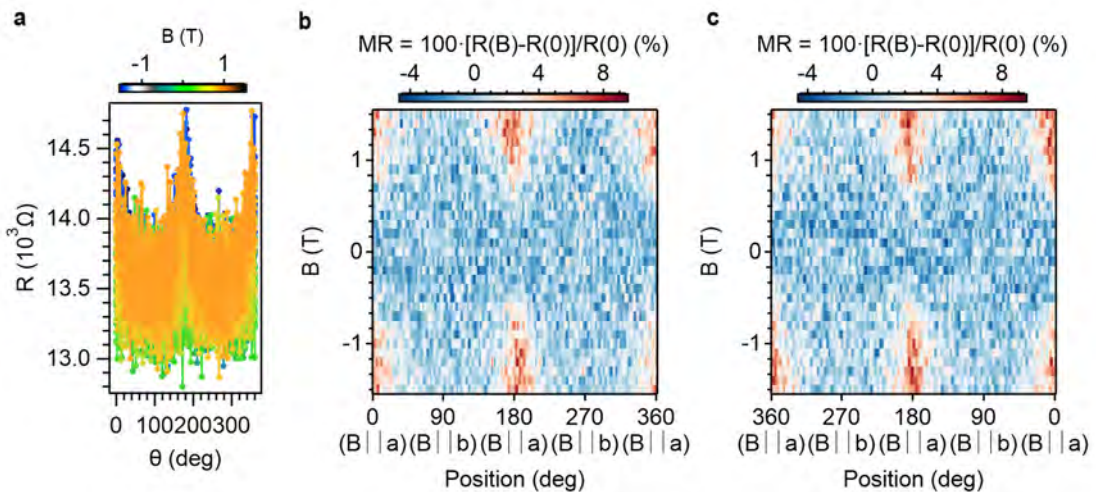
Figure S.25.- Resistance dependence as a function of the angle for different magnetic fields (a) and 2D plots of the magnetoresistance as a function of the angle between the magnetic field and the direction of the current in the vdWH from 0º to 360º (b) and viceversa (c) at 2 K. Rotation in the *a-b* plane.
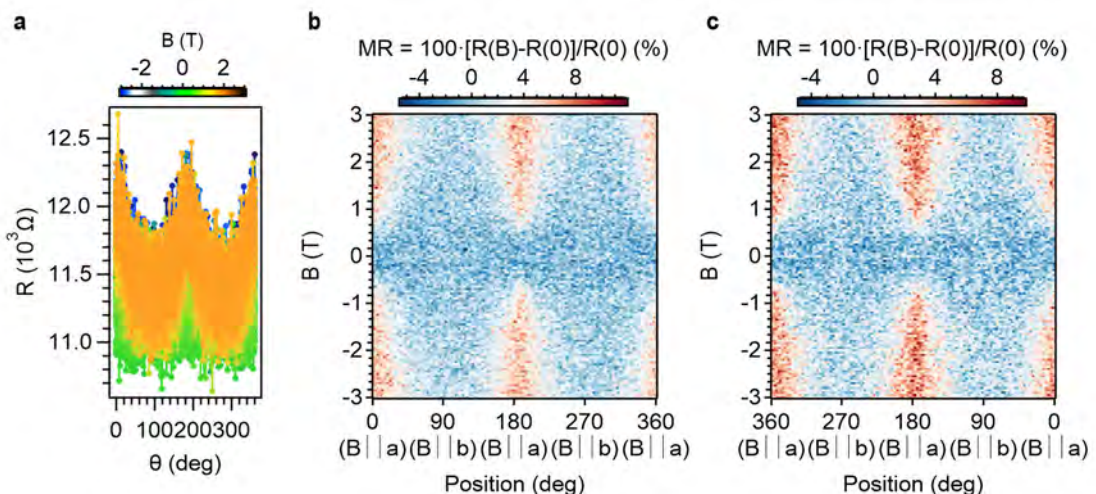

Figure S.26.- Resistance dependence as a function of the angle for different magnetic fields (a) and 2D plots of the magnetoresistance as a function of the angle between the magnetic field and the direction of the current in the vdWH from 0º to 360º (b) and viceversa (c) at 10 K. Rotation in the *a-b* plane.
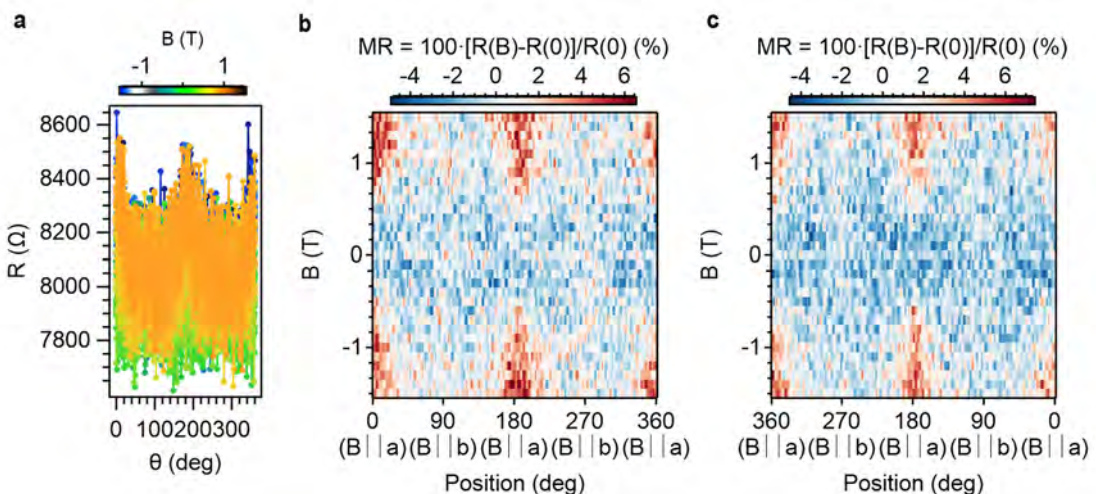

Figure S.27.- Resistance dependence as a function of the angle for different magnetic fields (a) and 2D plots of the magnetoresistance as a function of the angle between the magnetic field and the direction of the current in the vdWH from 0º to 360º (b) and viceversa (c) at 20 K. Rotation in the *a-b* plane.
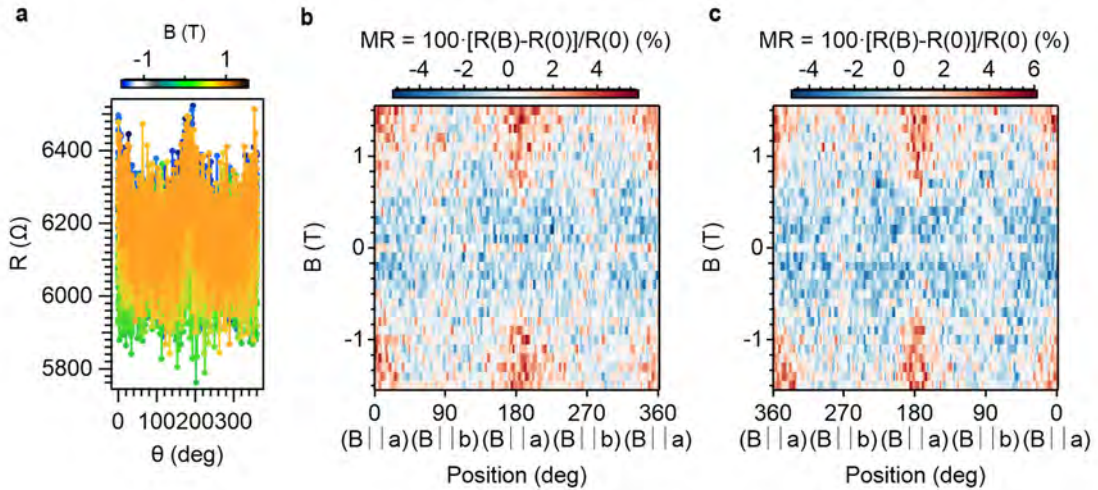
Figure S.28.- Resistance dependence as a function of the angle for different magnetic fields (a) and 2D plots of the magnetoresistance as a function of the angle between the magnetic field and the direction of the current in the vdWH from 0º to 360º (b) and viceversa (c) at 30 K. Rotation in the *a-b* plane.
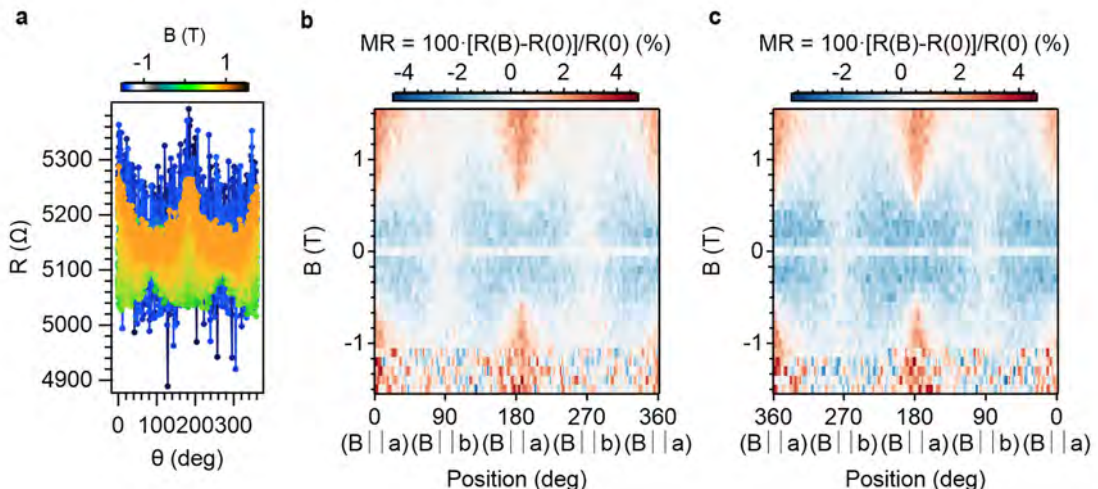
Figure S.29.- Resistance dependence as a function of the angle for different magnetic fields (a) and 2D plots of the magnetoresistance as a function of the angle between the magnetic field and the direction of the current in the vdWH from 0º to 360º (b) and viceversa (c) at 40 K. Rotation in the *a-b* plane.
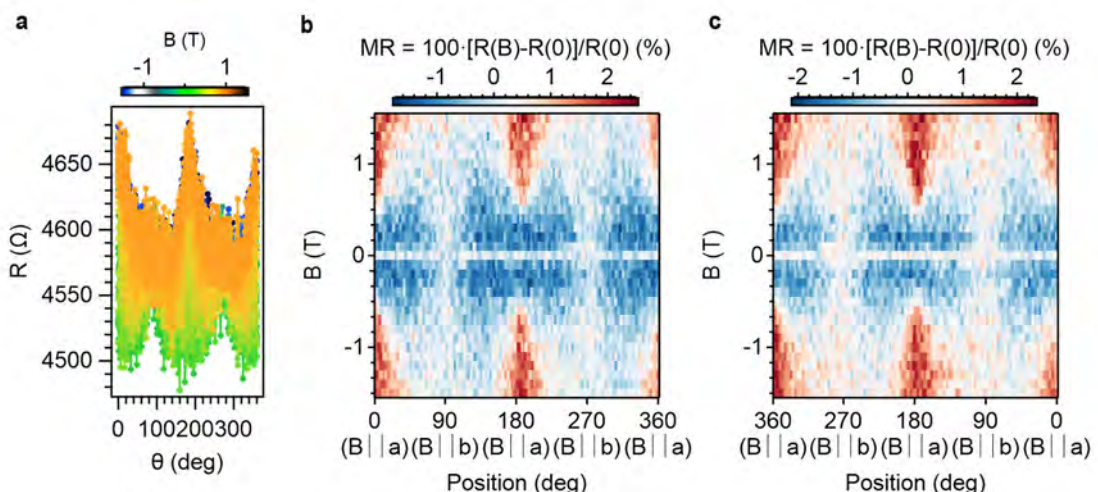
Figure S.30.- Resistance dependence as a function of the angle for different magnetic fields (a) and 2D plots of the magnetoresistance as a function of the angle between the magnetic field and the direction of the current in the vdWH from 0º to 360º (b) and viceversa (c) at 50 K. Rotation in the *a-b* plane.

23
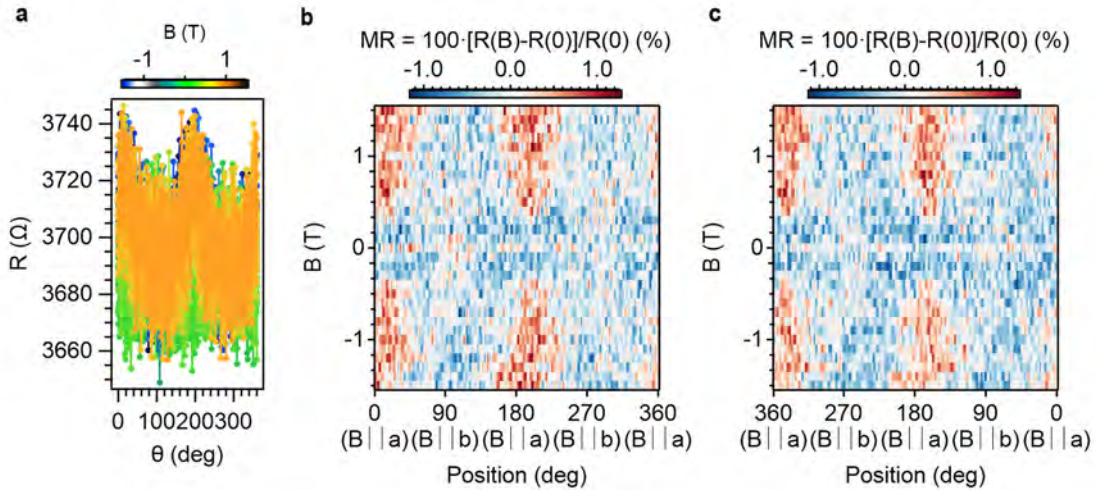
Figure S.31.- Resistance dependence as a function of the angle for different magnetic fields (a) and 2D plots of the magnetoresistance as a function of the angle between the magnetic field and the direction of the current in the vdWH from 0º to 360º (b) and viceversa (c) at 100 K. Rotation in the *a-b* plane.
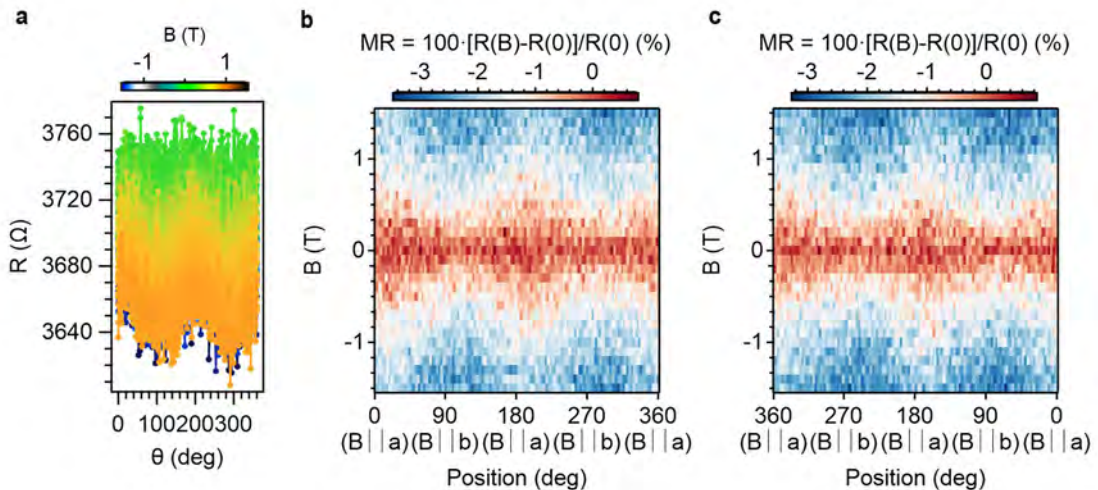
Figure S.32.- Resistance dependence as a function of the angle for different magnetic fields (a) and 2D plots of the magnetoresistance as a function of the angle between the magnetic field and the direction of the current in the vdWH from 0º to 360º (b) and viceversa (c) at 150 K. Rotation in the *a-b* plane.
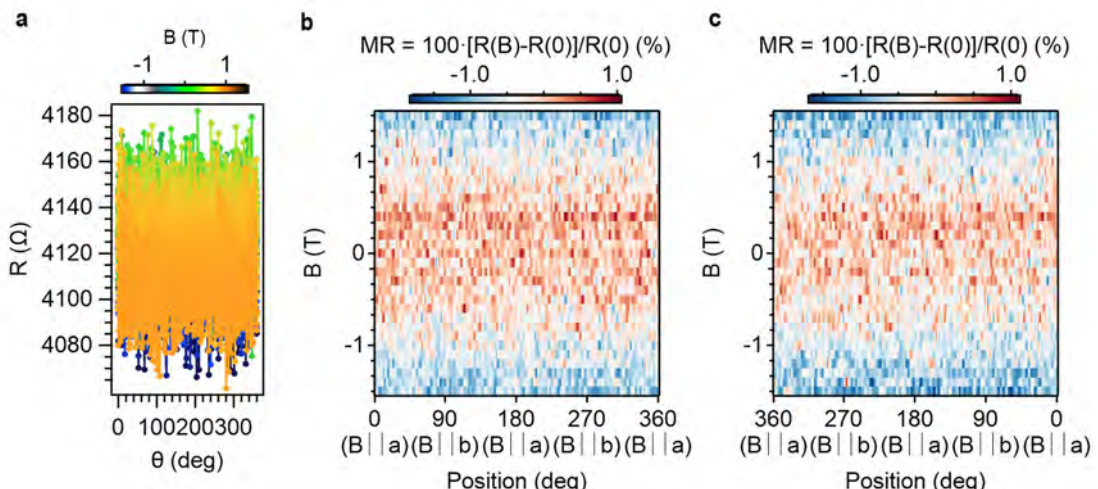

Figure S.33.- Resistance dependence as a function of the angle for different magnetic fields (a) and 2D plots of the magnetoresistance as a function of the angle between the magnetic field and the direction of the current in the vdWH from 0º to 360º (b) and viceversa (c) at 200 K. Rotation in the *a-b* plane.

24

3.4.2. Device A.2. (CrSBr monolayer).
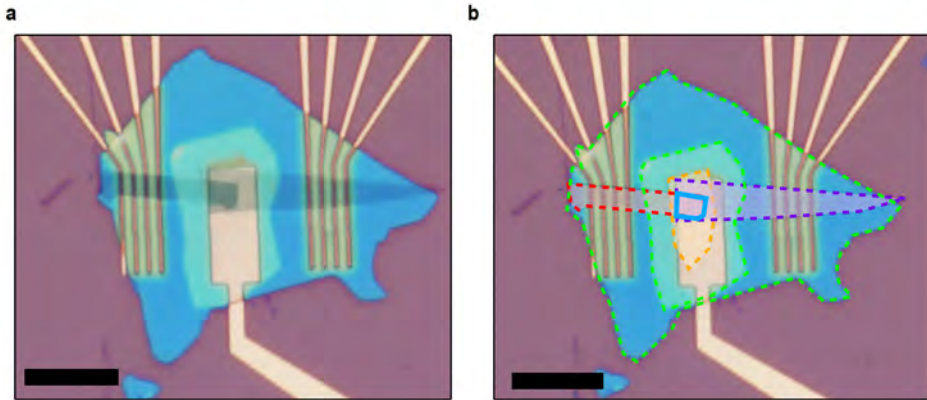
Figure S.34.- Optical picture of the device. For simplicity, the top graphite contact has been highlighted in red, the bottom graphite contact in purple and the CrSBr barrier in orange. h-BN is marked in green. The junction (blue area) is the overlapped area formed by the three different materials. Scale bar: 10 μm.
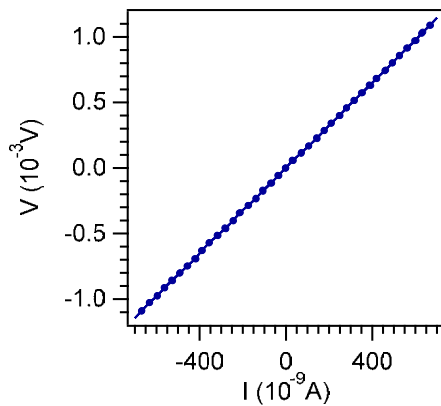
Figure S.35.- DC IV curve for the junction area at 2 K.
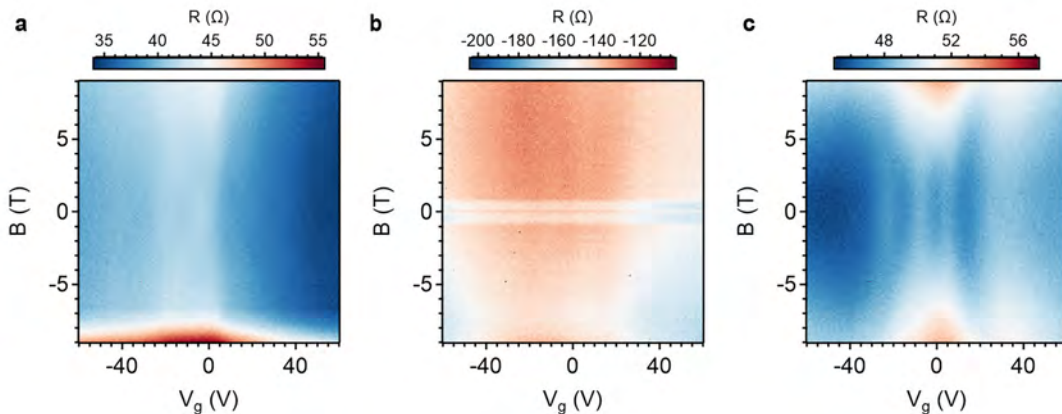
Figure S.36.- Field dependence of the resistance as a function of the gate voltage at 2 K for the top contact (a), the junction (b) and the bottom contact (c). Field parallel to the *a* axis.
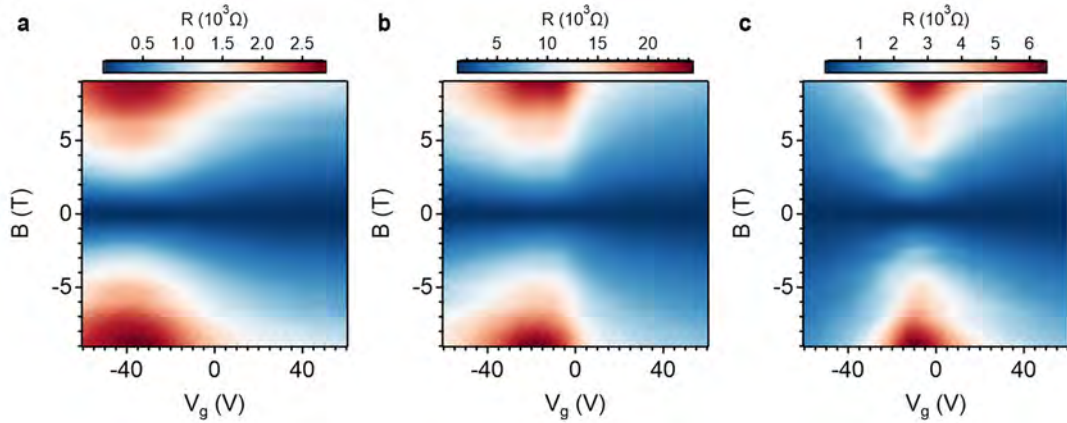
Figure S.37.- Field dependence of the resistance as a function of the gate voltage at 2 K for the top contact (a), the junction (b) and the bottom contact (c). Field parallel to the *c* axis.
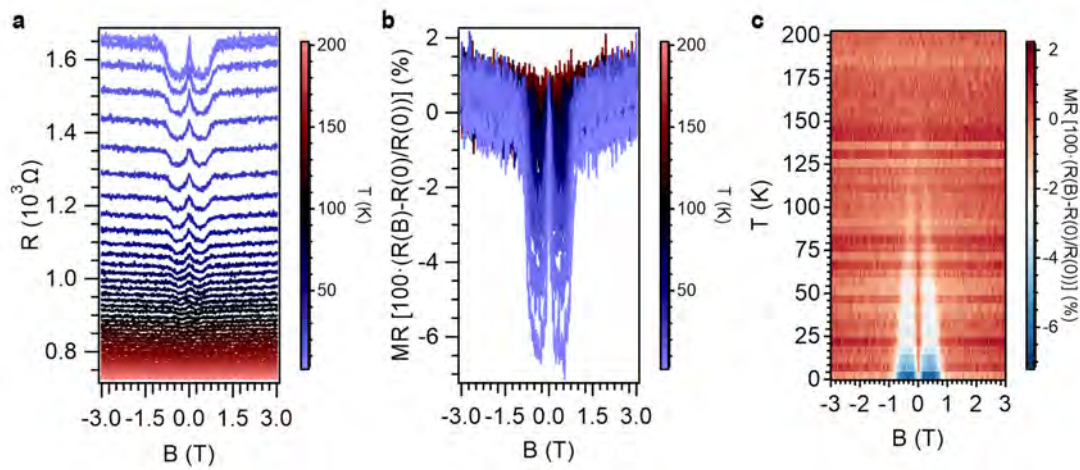
Figure S.38.- a) Resistance as a function of the magnetic field for different temperatures. b) Calculated magnetoresistance as a function of the magnetic field for different temperatures. c) Resistance plot as a function of temperature and magnetic field. Field parallel to the *a* axis.
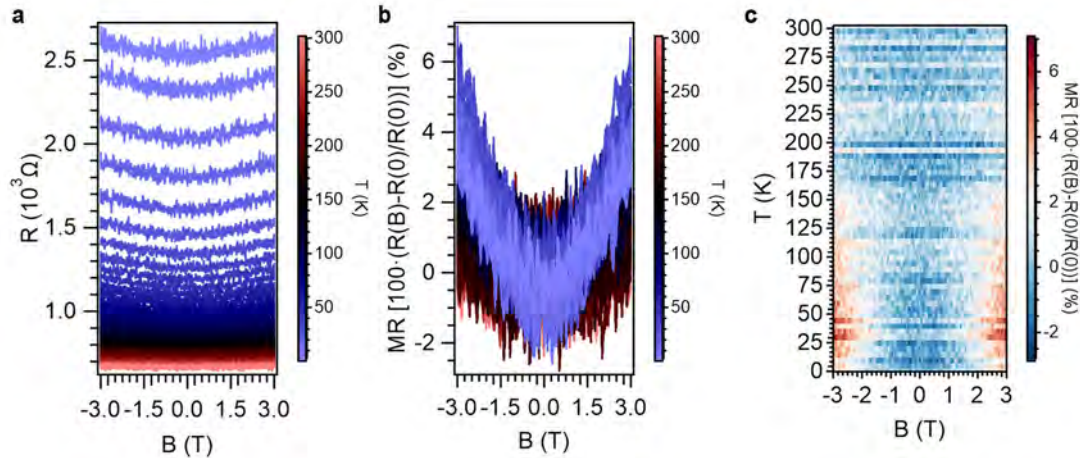
Figure S.39.- a) Resistance as a function of the magnetic field for different temperatures. b) Calculated magnetoresistance as a function of the magnetic field for different temperatures. c) Resistance plot as a function of temperature and magnetic field. Field parallel to the *b* axis.
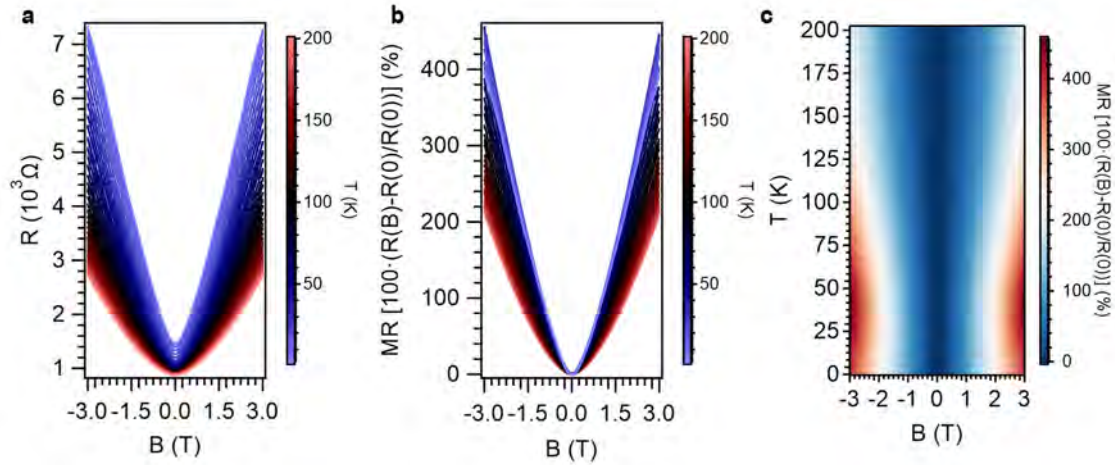
Figure S.40.- a) Resistance as a function of the magnetic field for different temperatures. b) Calculated magnetoresistance as a function of the magnetic field for different temperatures. c) Resistance plot as a function of temperature and magnetic field. Field parallel to the *c* axis.
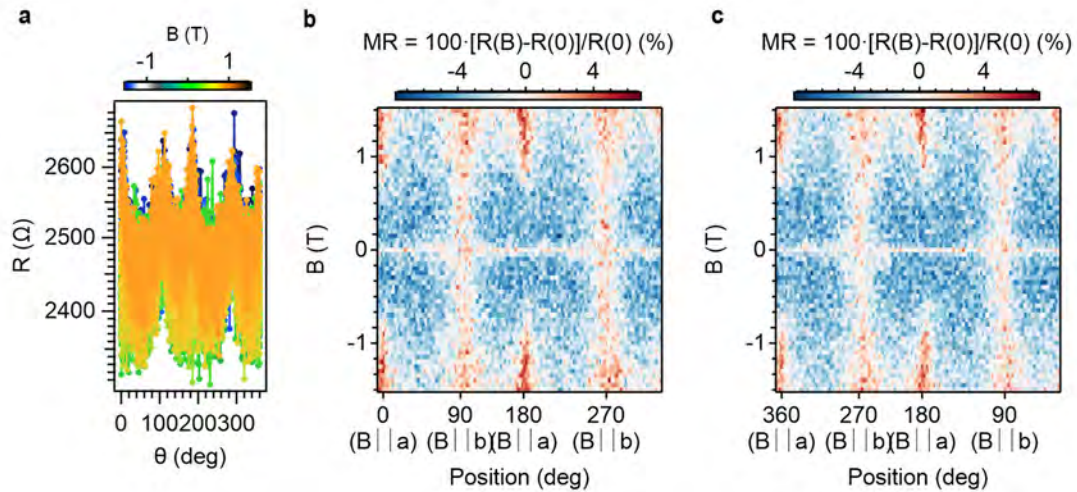

Figure S.41.- a) Resistance dependence as a function of the angle for different magnetic fields (a) and 2D plots of the magnetoresistance as a function of the angle between the magnetic field and the direction of the current in the vdWH from 0º to 360º (b) and viceversa (c) at 2 K. Rotation in the *a-b* plane.


Figure S.42.- a) Resistance dependence as a function of the angle for different magnetic fields (a) and 2D plots of the magnetoresistance as a function of the angle between the magnetic field and the direction of the current in the vdWH from 0º to 360º (b) and viceversa (c) at 10 K. Rotation in the *a-b* plane.

Figure S.43.- a) Resistance dependence as a function of the angle for different magnetic fields (a) and 2D plots of the magnetoresistance as a function of the angle between the magnetic field and the direction of the current in the vdWH from 0º to 360º (b) and viceversa (c) at 20 K. Rotation in the *a-b* plane.

Figure S.44.- a) Resistance dependence as a function of the angle for different magnetic fields (a) and 2D plots of the magnetoresistance as a function of the angle between the magnetic field and the direction of the current in the vdWH from 0º to 360º (b) and viceversa (c) at 30 K. Rotation in the *a-b* plane.

Figure S.45.- a) Resistance dependence as a function of the angle for different magnetic fields (a) and 2D plots of the magnetoresistance as a function of the angle between the magnetic field and the direction of the current in the vdWH from 0º to 360º (b) and viceversa (c) at 40 K. Rotation in the *a-b* plane.

Figure S.46.- a) Resistance dependence as a function of the angle for different magnetic fields (a) and 2D plots of the magnetoresistance as a function of the angle between the magnetic field and the direction of the current in the vdWH from 0° to 360° (b) and viceversa (c) at 50 K. Rotation in the *a-b* plane.

### 3.4.3. Device A.3. (CrSBr monolayer).
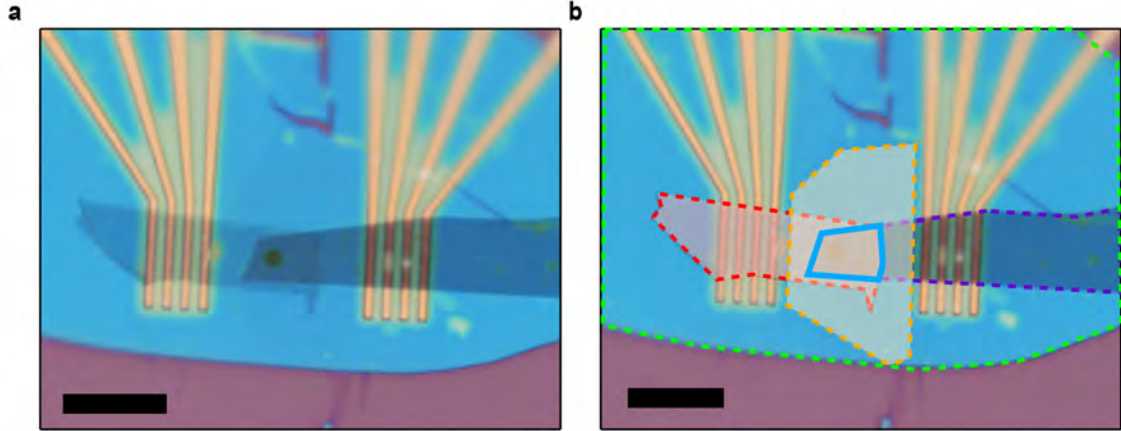
Figure S.47.- Optical picture of the device. For simplicity, the top graphite contact has been highlighted in red, the bottom graphite contact in purple and the CrSBr barrier in orange. h-BN is marked in green. The junction (blue area) is the overlapped area formed by the three different materials. Scale bar: 10 μm.
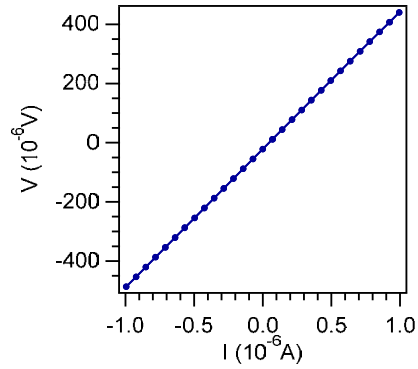
Figure S.48.- DC IV curve for the junction area at 2 K.
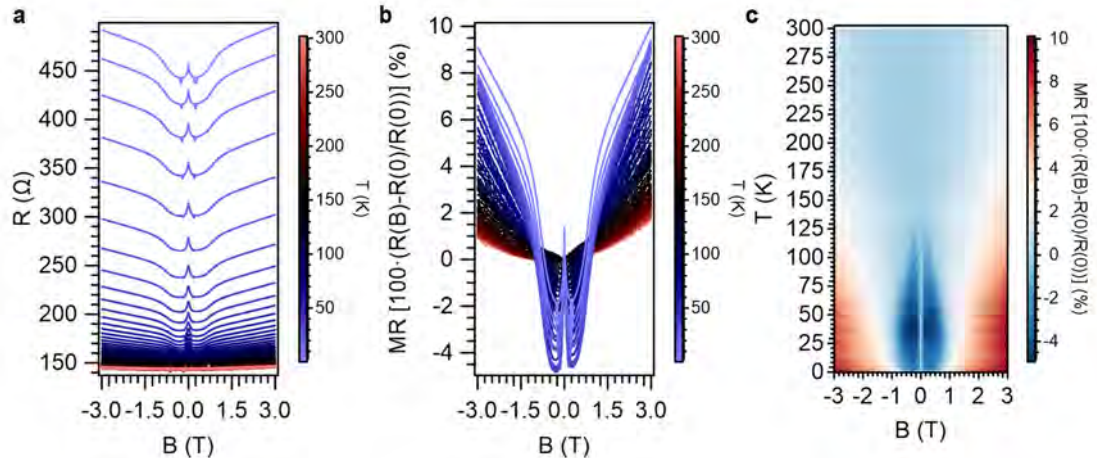
Figure S.49.- a) Resistance as a function of the magnetic field for different temperatures. b) Calculated magnetoresistance as a function of the magnetic field for different temperatures. c) Resistance plot as a function of temperature and magnetic field. Field parallel to the *a* axis.
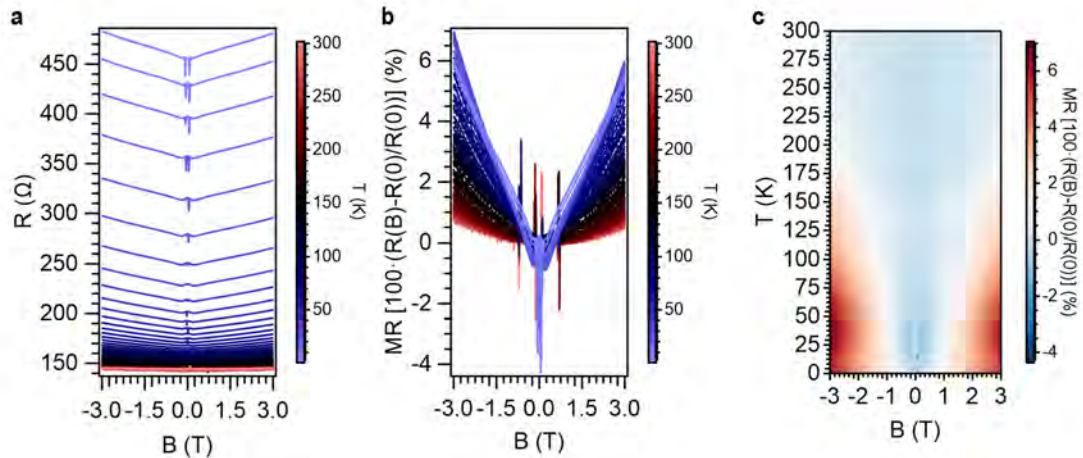
Figure S.50.- a) Resistance as a function of the magnetic field for different temperatures. b) Calculated magnetoresistance as a function of the magnetic field for different temperatures. c) Resistance plot as a function of temperature and magnetic field. Field parallel to the *b* axis.
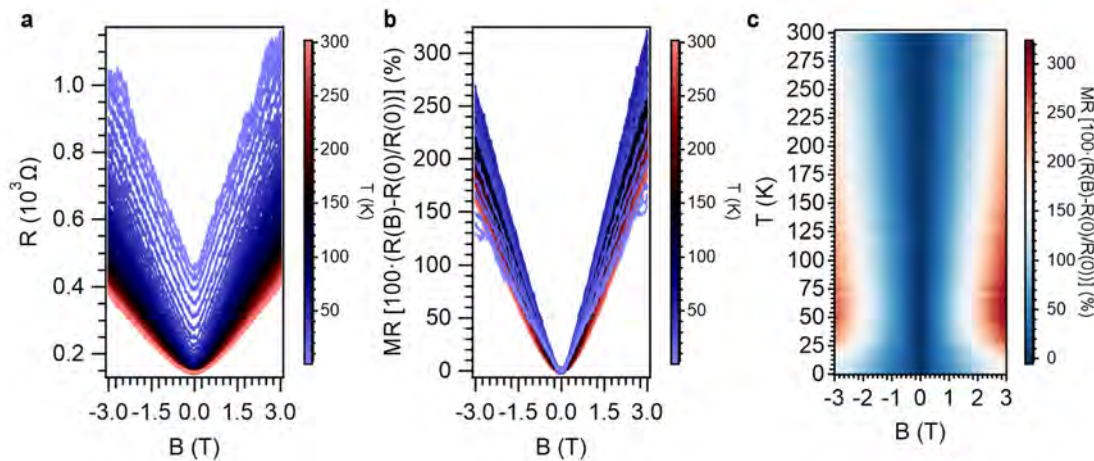
Figure S.51.- a) Resistance as a function of the magnetic field for different temperatures. b) Calculated magnetoresistance as a function of the magnetic field for different temperatures. c) Resistance plot as a function of temperature and magnetic field. Field parallel to the *c* axis.
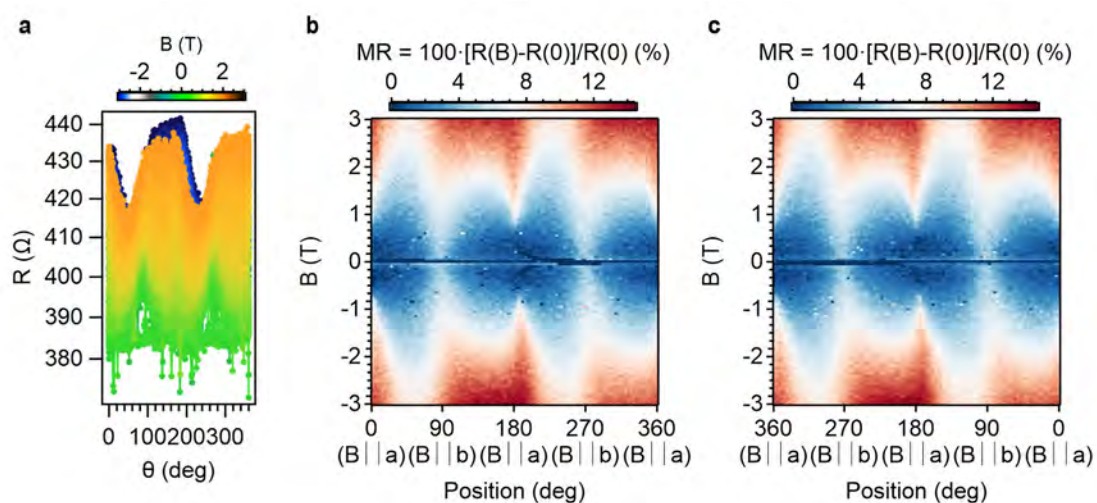

Figure S.52.- Resistance dependence as a function of the angle for different magnetic fields (a) and 2D plots of the magnetoresistance as a function of the angle between the magnetic field and the direction of the current in the vdWH from 0º to 360º (b) and viceversa (c) at 2 K. Rotation in the *a-b* plane.

Figure S.53.- Resistance dependence as a function of the angle for different magnetic fields (a) and 2D plots of the magnetoresistance as a function of the angle between the magnetic field and the direction of the current in the vdWH from 0º to 360º (b) and viceversa (c) at 10 K. Rotation in the *a-b* plane.
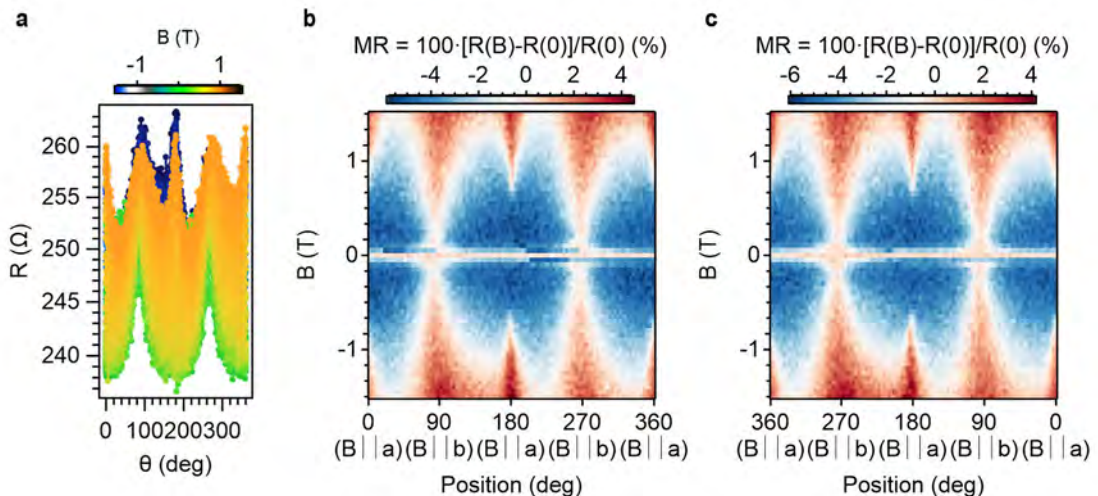

Figure S.54.- Resistance dependence as a function of the angle for different magnetic fields (a) and 2D plots of the magnetoresistance as a function of the angle between the magnetic field and the direction of the current in the vdWH from 0º to 360º (b) and viceversa (c) at 30 K. Rotation in the *a-b* plane.
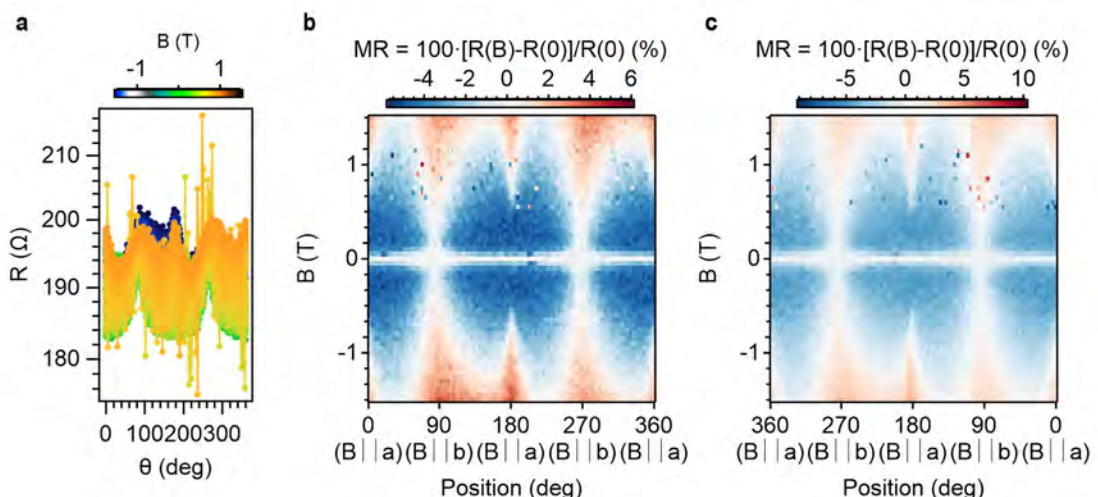

Figure S.55.- Resistance dependence as a function of the angle for different magnetic fields (a) and 2D plots of the magnetoresistance as a function of the angle between the magnetic field and the direction of the current in the vdWH from 0º to 360º (b) and viceversa (c) at 50 K. Rotation in the *a-b* plane.

32
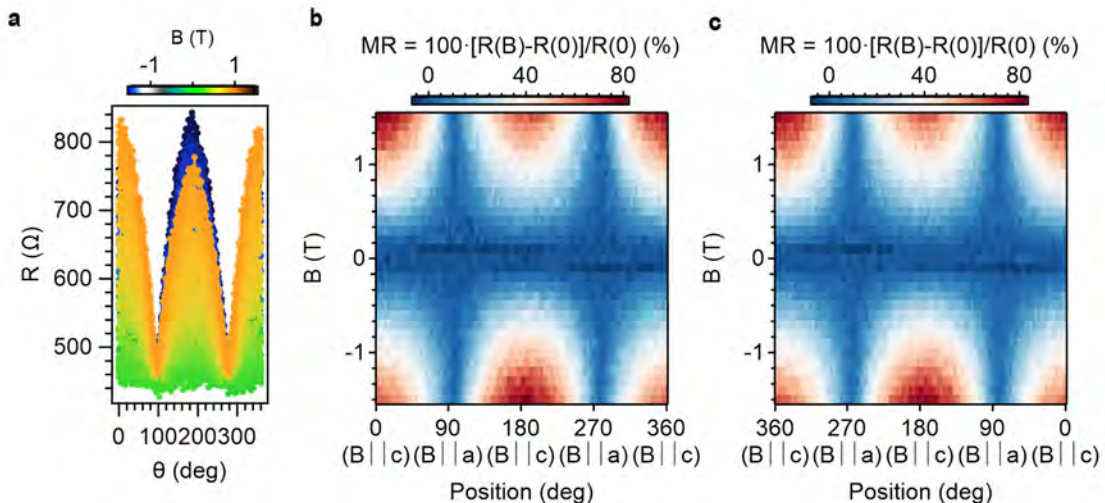
Figure S.56.- Resistance dependence as a function of the angle for different magnetic fields (a) and 2D plots of the magnetoresistance as a function of the angle between the magnetic field and the direction of the current in the vdWH from 0º to 360º (b) and viceversa (c) at 2 K. Rotation in the *a-c* plane.
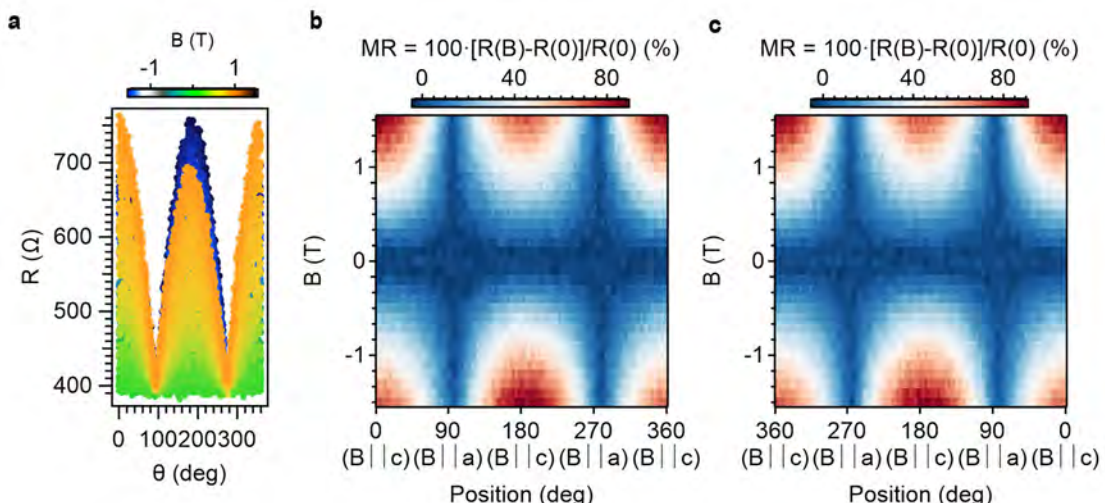
Figure S.57.- Resistance dependence as a function of the angle for different magnetic fields (a) and 2D plots of the magnetoresistance as a function of the angle between the magnetic field and the direction of the current in the vdWH from 0º to 360º (b) and viceversa (c) at 10 K. Rotation in the *a-c* plane.
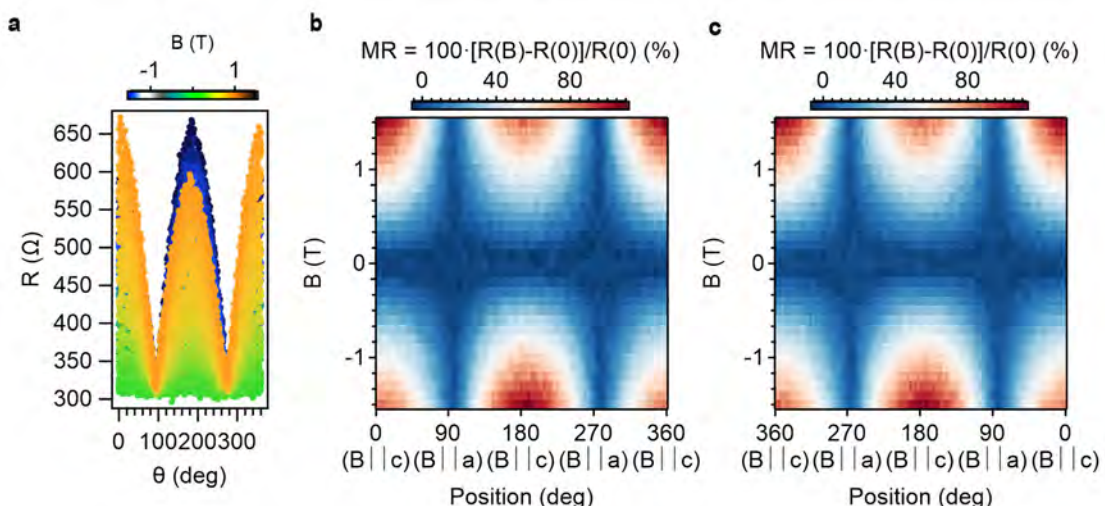

Figure S.58.- Resistance dependence as a function of the angle for different magnetic fields (a) and 2D plots of the magnetoresistance as a function of the angle between the magnetic field and the direction of the current in the vdWH from 0º to 360º (b) and viceversa (c) at 20 K. Rotation in the *a-c* plane.

33
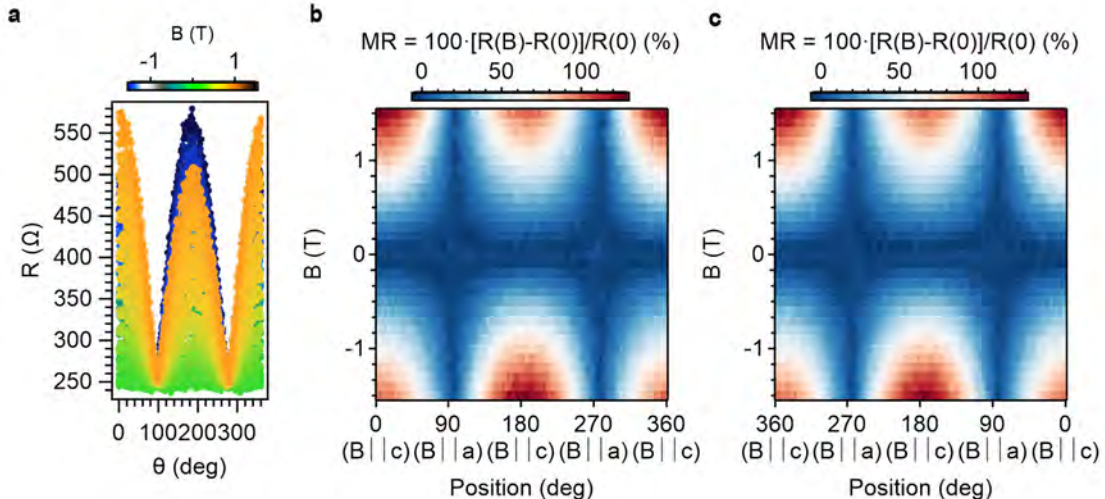
Figure S.59.- Resistance dependence as a function of the angle for different magnetic fields (a) and 2D plots of the magnetoresistance as a function of the angle between the magnetic field and the direction of the current in the vdWH from 0º to 360º (b) and viceversa (c) at 30 K. Rotation in the *a-c* plane.
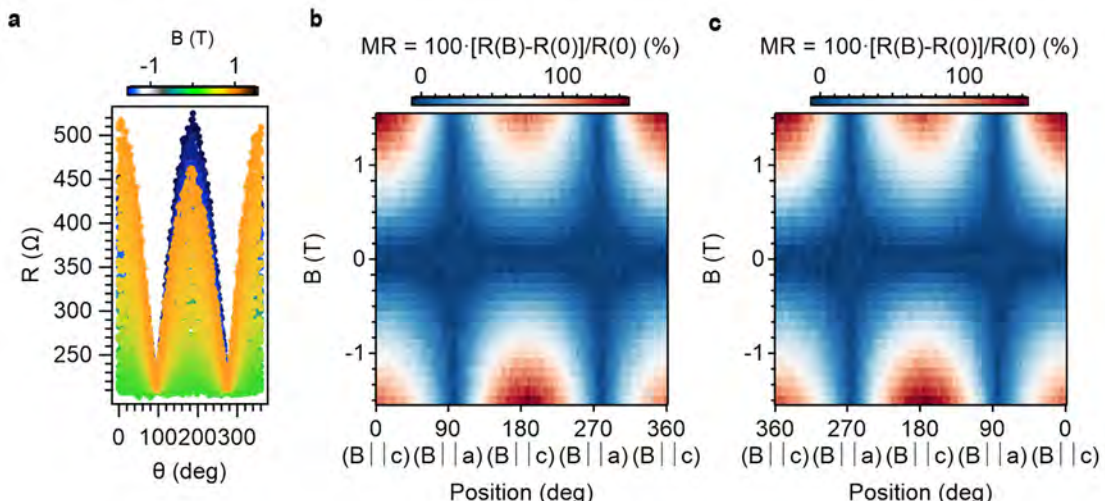

Figure S.60.- Resistance dependence as a function of the angle for different magnetic fields (a) and 2D plots of the magnetoresistance as a function of the angle between the magnetic field and the direction of the current in the vdWH from 0º to 360º (b) and viceversa (c) at 40 K. Rotation in the *a-c* plane.
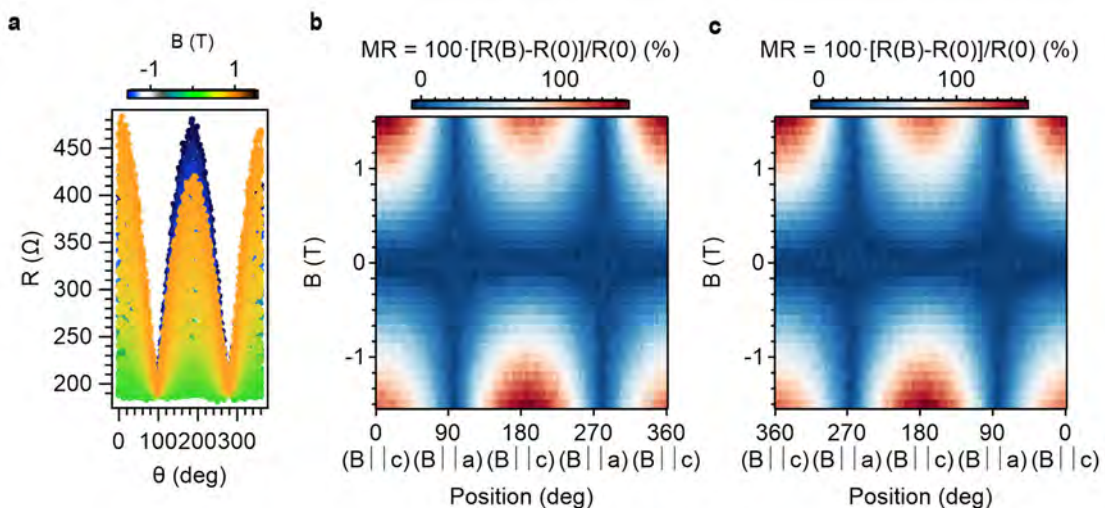

Figure S.61.- Resistance dependence as a function of the angle for different magnetic fields (a) and 2D plots of the magnetoresistance as a function of the angle between the magnetic field and the direction of the current in the vdWH from 0º to 360º (b) and viceversa (c) at 50 K. Rotation in the *a-c* plane.
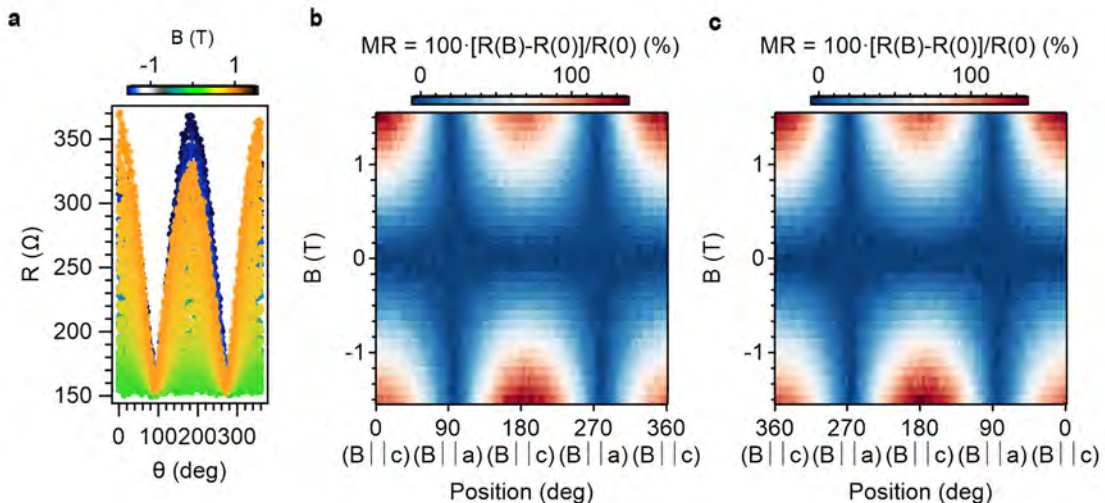
Figure S.62.- Resistance dependence as a function of the angle for different magnetic fields (a) and 2D plots of the magnetoresistance as a function of the angle between the magnetic field and the direction of the current in the vdWH from 0º to 360º (b) and viceversa (c) at 100 K. Rotation in the *a-c* plane.
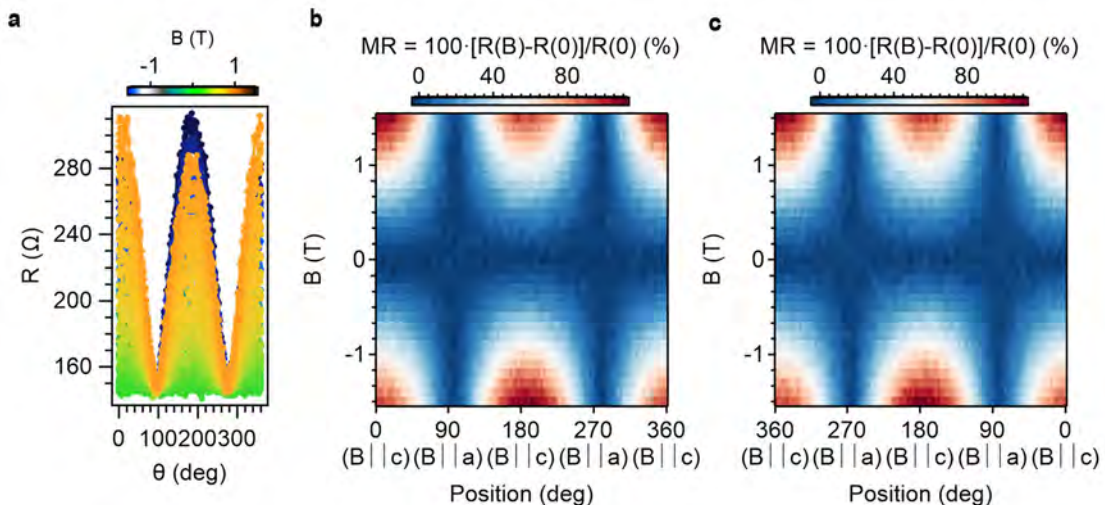
Figure S.63.- Resistance dependence as a function of the angle for different magnetic fields (a) and 2D plots of the magnetoresistance as a function of the angle between the magnetic field and the direction of the current in the vdWH from 0º to 360º (b) and viceversa (c) at 150 K. Rotation in the *a-c* plane.
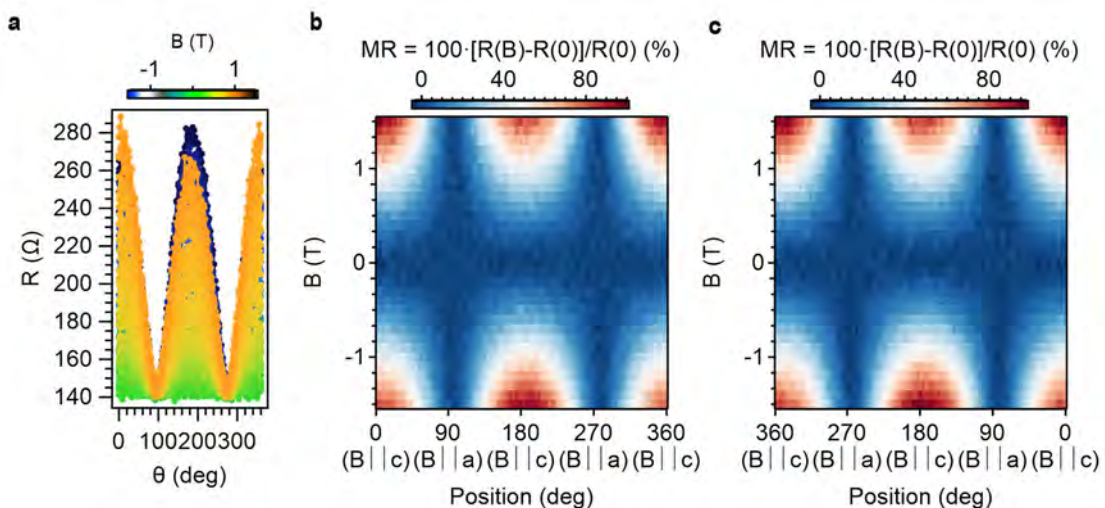
Figure S.64.- Resistance dependence as a function of the angle for different magnetic fields (a) and 2D plots of the magnetoresistance as a function of the angle between the magnetic field and the direction of the current in the vdWH from 0º to 360º (b) and viceversa (c) at 200 K. Rotation in the *a-c* plane.

3.4.4. Device A.4. (CrSBr monolayer).
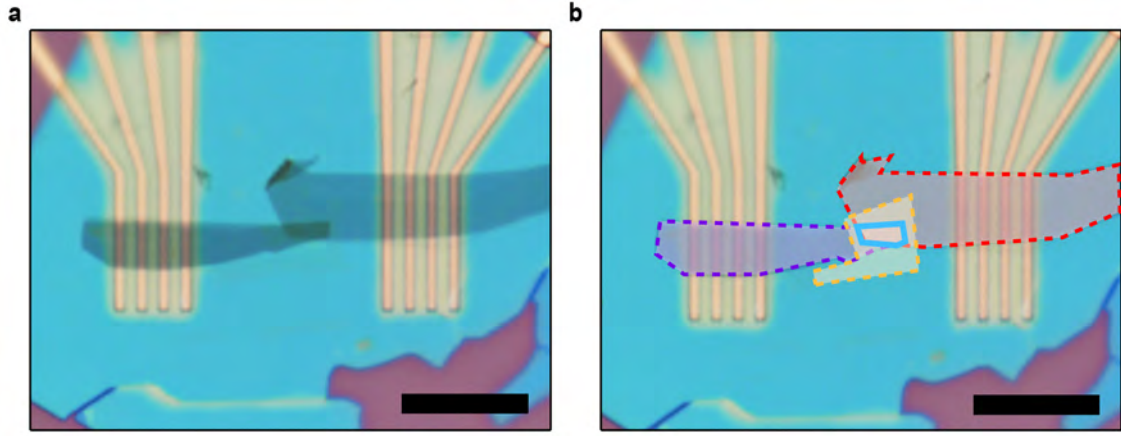
Figure S.65.- Optical picture of the device. For simplicity, the top graphite contact has been highlighted in red, the bottom graphite contact in purple and the CrSBr barrier in orange. h-BN is marked in green. The junction (blue area) is the overlapped area formed by the three different materials. Scale bar: 10 μm.
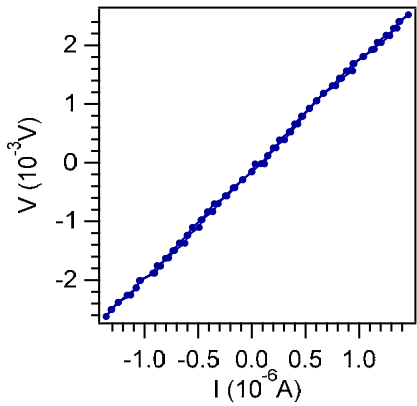

**Figure S.66.-** DC IV curve for the junction area at 2 K.
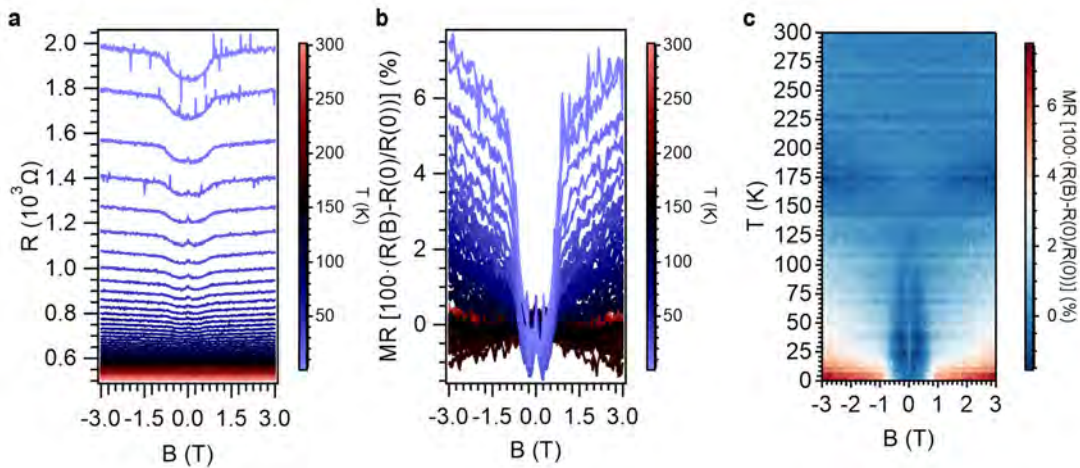
Figure S.67.- Resistance as a function of the magnetic field for different temperatures. b) Calculated magnetoresistance as a function of the magnetic field for different temperatures. c) Resistance plot as a function of temperature and magnetic field. Field parallel to the *a* axis.
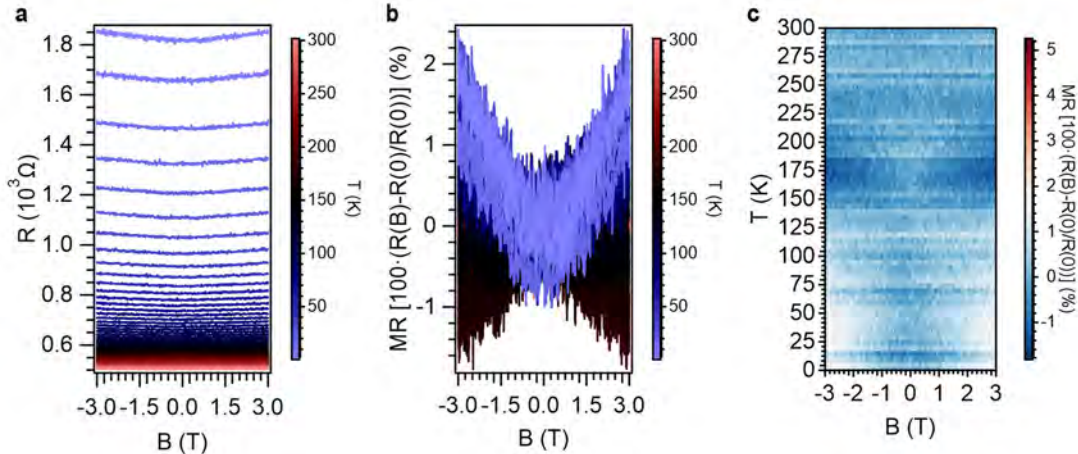
Figure S.68.- Resistance as a function of the magnetic field for different temperatures. b) Calculated magnetoresistance as a function of the magnetic field for different temperatures. c) Resistance plot as a function of temperature and magnetic field. Field parallel to the *b* axis.
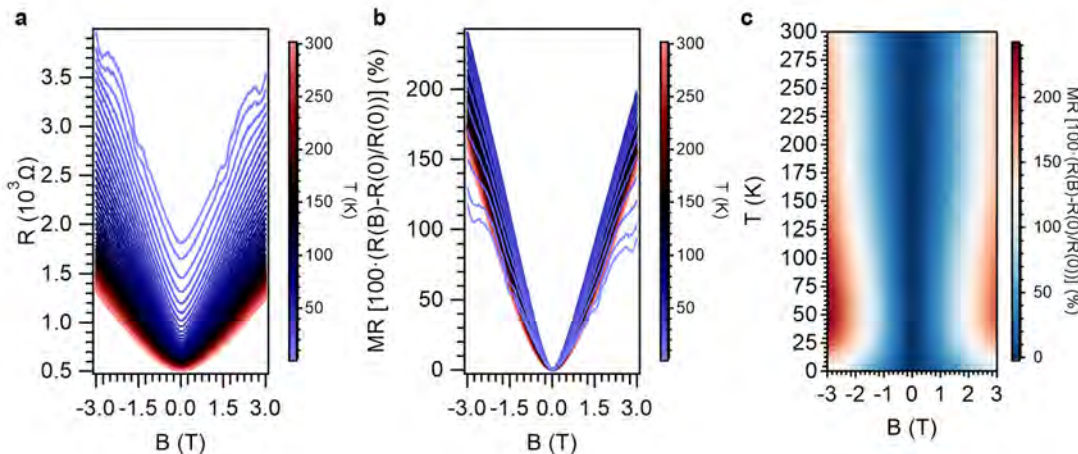
Figure S.69.- Resistance as a function of the magnetic field for different temperatures. b) Calculated magnetoresistance as a function of the magnetic field for different temperatures. c) Resistance plot as a function of temperature and magnetic field. Field parallel to the *c* axis.
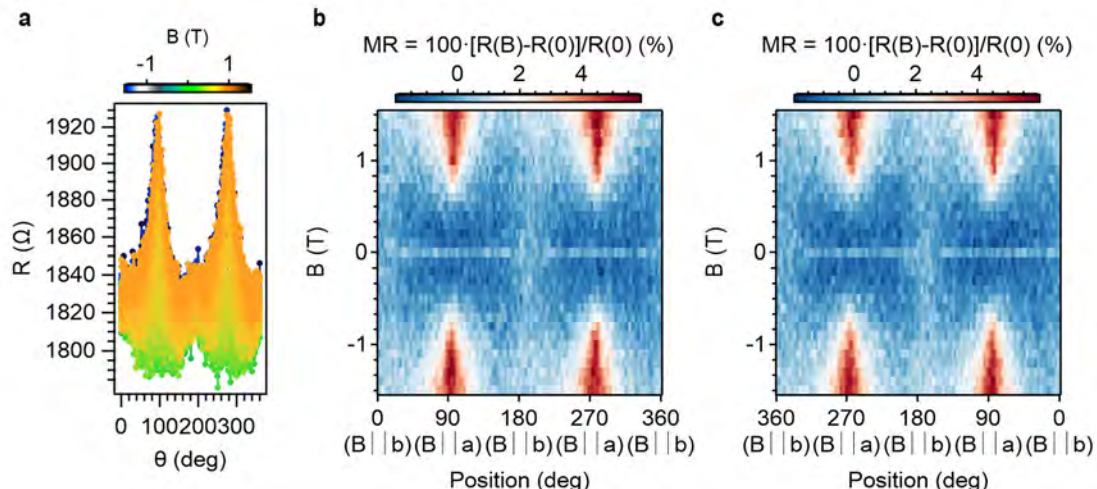

Figure S.70.- Resistance dependence as a function of the angle for different magnetic fields (a) and 2D plots of the magnetoresistance as a function of the angle between the magnetic field and the direction of the current in the vdWH from 0º to 360º (b) and viceversa (c) at 2 K. Rotation in the *a-b* plane.

37
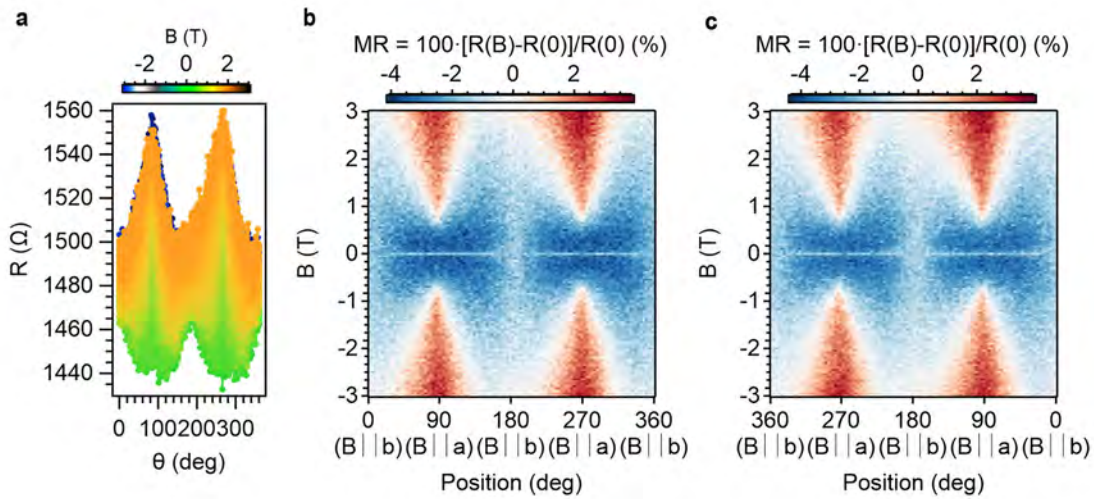
Figure S.71.- Resistance dependence as a function of the angle for different magnetic fields (a) and 2D plots of the magnetoresistance as a function of the angle between the magnetic field and the direction of the current in the vdWH from 0º to 360º (b) and viceversa (c) at 10 K. Rotation in the *a-b* plane.
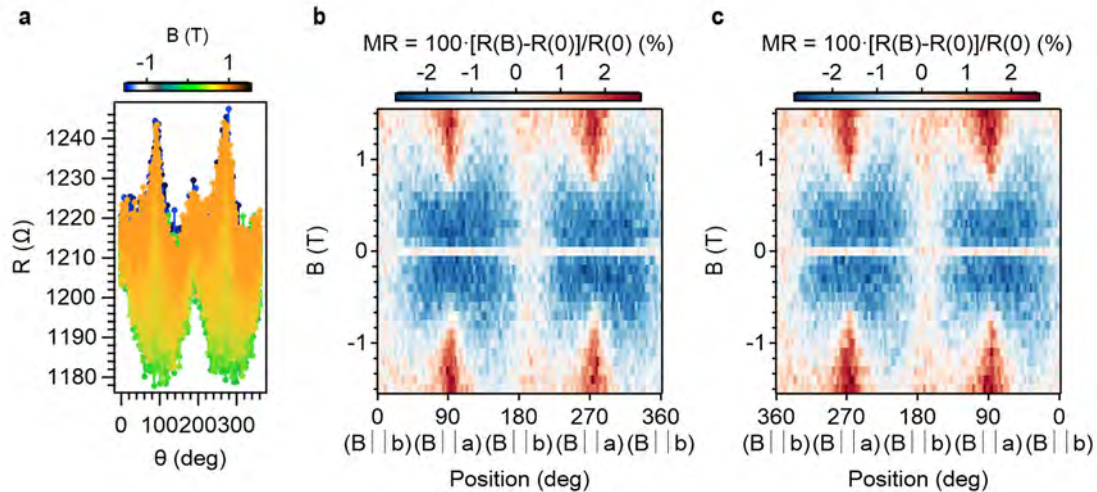

Figure S.72.- Resistance dependence as a function of the angle for different magnetic fields (a) and 2D plots of the magnetoresistance as a function of the angle between the magnetic field and the direction of the current in the vdWH from 0º to 360º (b) and viceversa (c) at 20 K. Rotation in the *a-b* plane.
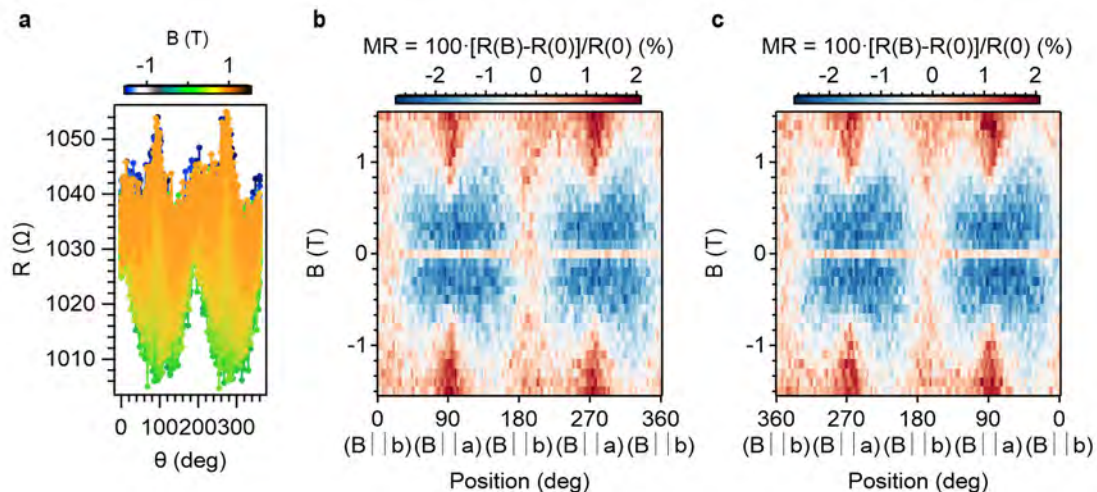

Figure S.73.- Resistance dependence as a function of the angle for different magnetic fields (a) and 2D plots of the magnetoresistance as a function of the angle between the magnetic field and the direction of the current in the vdWH from 0º to 360º (b) and viceversa (c) at 30 K. Rotation in the *a-b* plane.
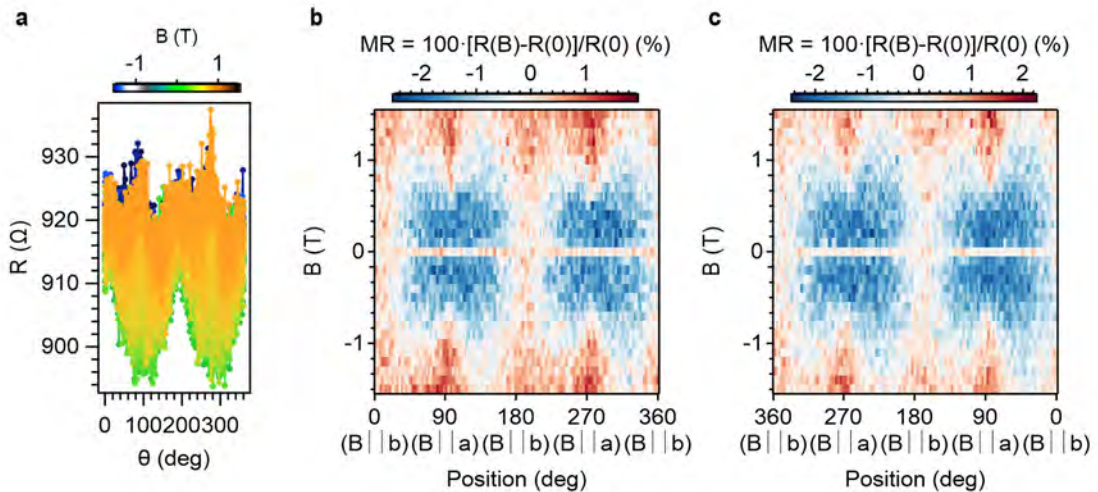
Figure S.74.- Resistance dependence as a function of the angle for different magnetic fields (a) and 2D plots of the magnetoresistance as a function of the angle between the magnetic field and the direction of the current in the vdWH from 0º to 360º (b) and viceversa (c) at 40 K. Rotation in the *a-b* plane.
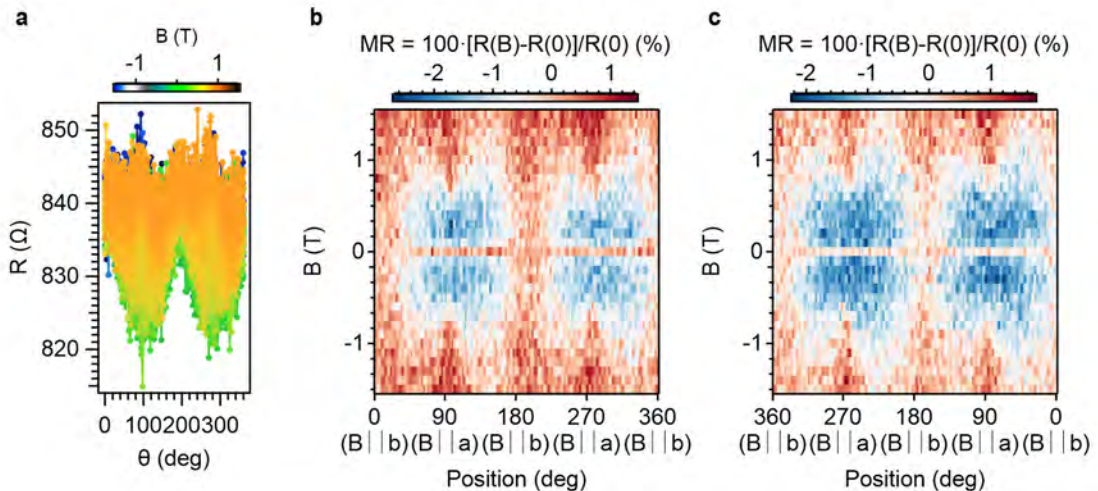

Figure S.75.- Resistance dependence as a function of the angle for different magnetic fields (a) and 2D plots of the magnetoresistance as a function of the angle between the magnetic field and the direction of the current in the vdWH from 0º to 360º (b) and viceversa (c) at 50 K. Rotation in the *a-b* plane.
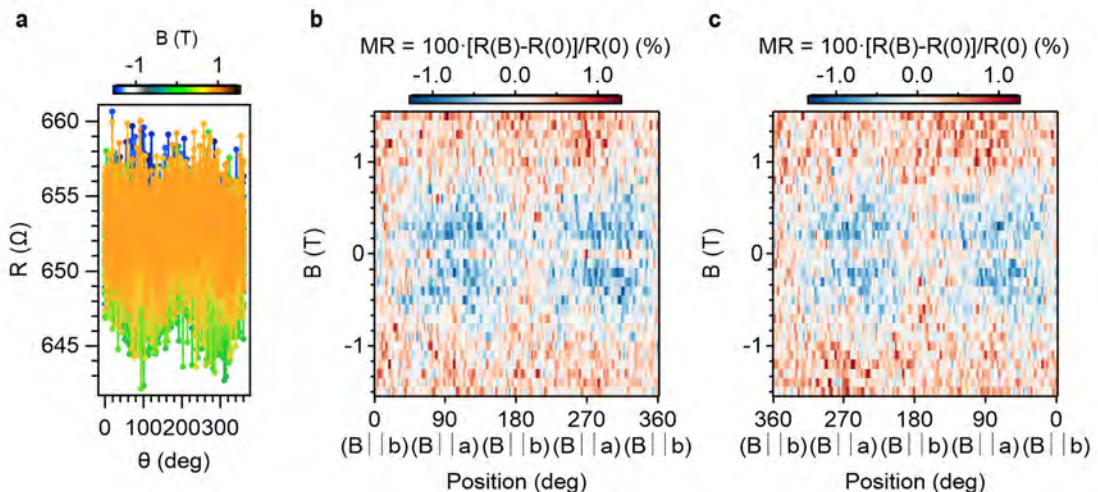
Figure S.76.- Resistance dependence as a function of the angle for different magnetic fields (a) and 2D plots of the magnetoresistance as a function of the angle between the magnetic field and the direction of the current in the vdWH from 0º to 360º (b) and viceversa (c) at 100 K. Rotation in the *a-b* plane.

### 3.4.5. Device A.5. (CrSBr monolayer).
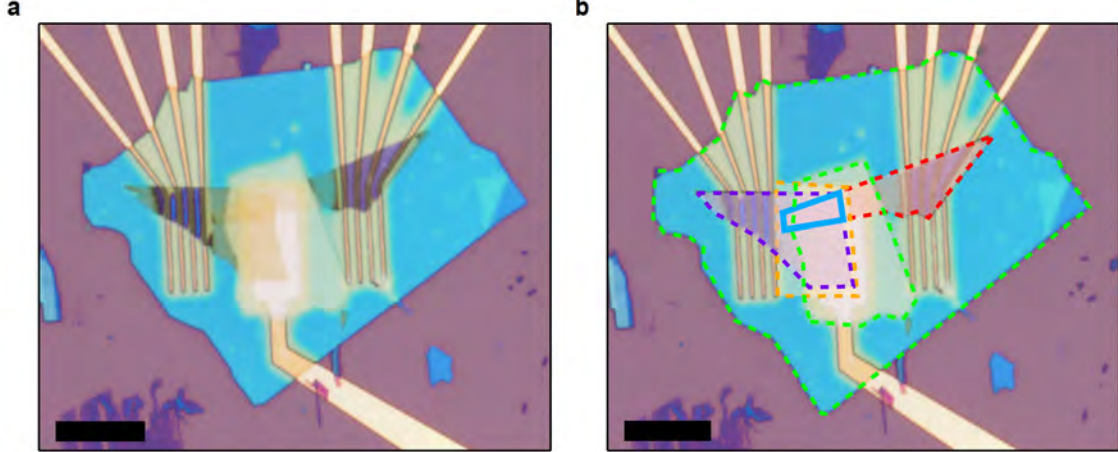
Figure S.77.- Optical picture of the device. For simplicity, the top NbSe$_2$ contact has been highlighted in red, the bottom NbSe$_2$ contact in purple and the CrSBr barrier in orange. h-BN is marked in green. The junction (blue area) is the overlapped area formed by the three different materials. Scale bar: 10 μm.
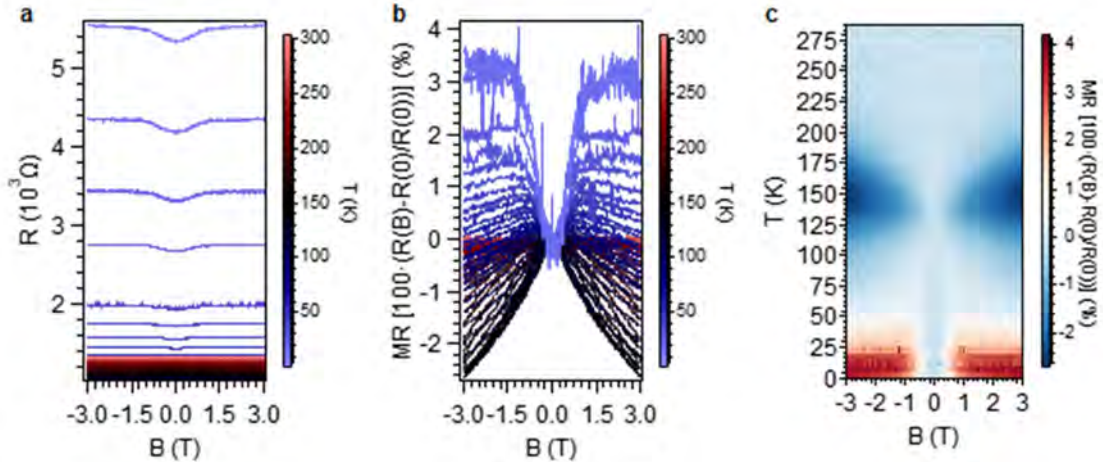

Figure S.78.- a) Resistance as a function of the magnetic field for different temperatures. b) Calculated magnetoresistance as a function of the magnetic field for different temperatures. c) Resistance plot as a function of temperature and magnetic field. Field parallel to the *a* axis.
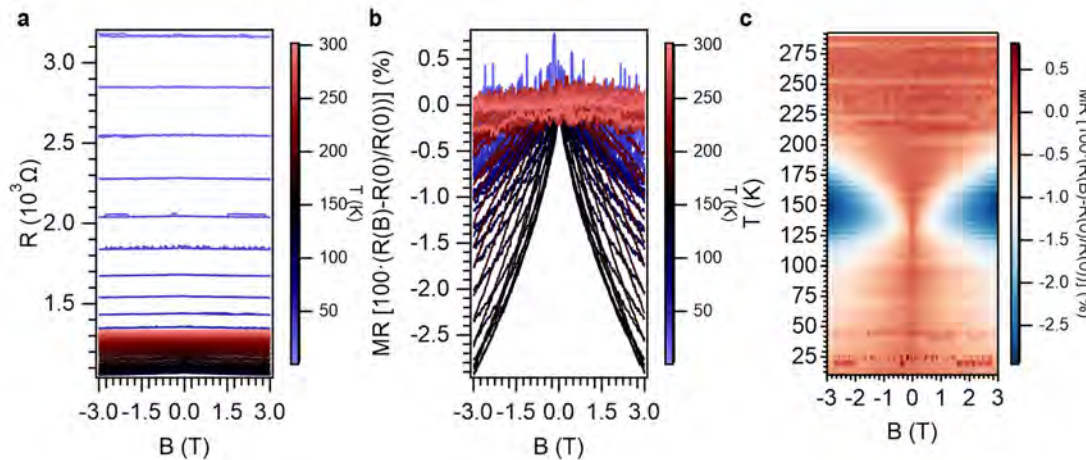

Figure S.79.- a) Resistance as a function of the magnetic field for different temperatures. b) Calculated magnetoresistance as a function of the magnetic field for different temperatures. c) Resistance plot as a function of temperature and magnetic field. Field parallel to the *b* axis.
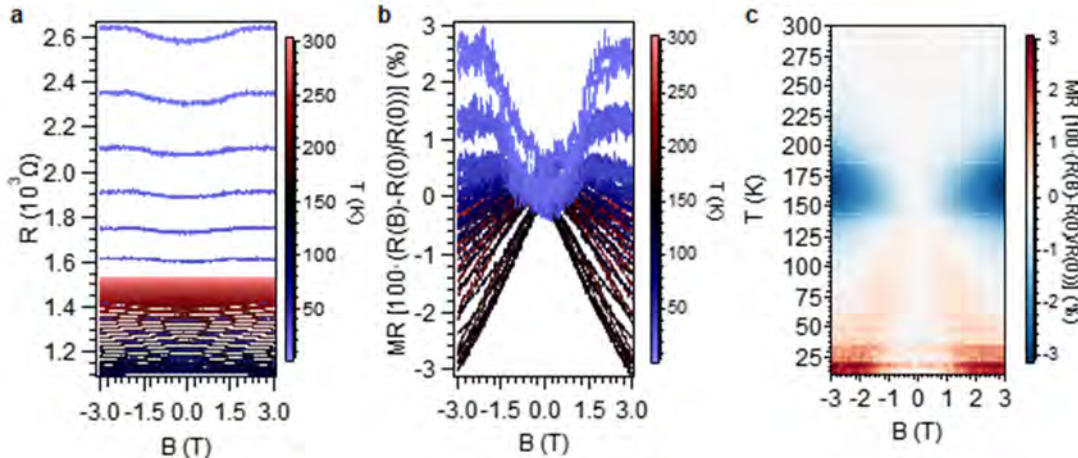
Figure S.80.- a) Resistance as a function of the magnetic field for different temperatures. b) Calculated magnetoresistance as a function of the magnetic field for different temperatures. c) Resistance plot as a function of temperature and magnetic field. Field parallel to the *c* axis.
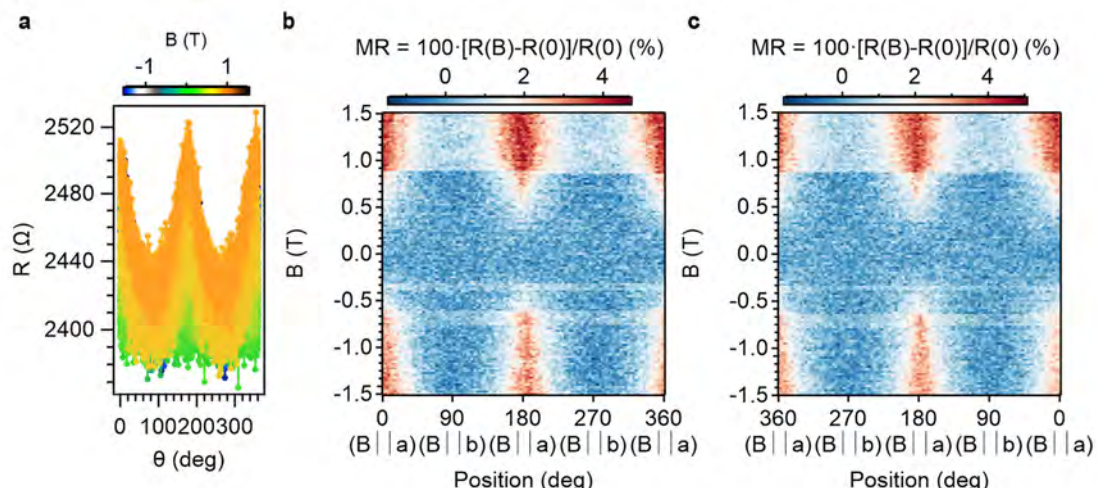

Figure S.81.- Resistance dependence as a function of the angle for different magnetic fields (a) and 2D plots of the magnetoresistance as a function of the angle between the magnetic field and the direction of the current in the vdWH from 0º to 360º (b) and viceversa (c) at 10 K. Rotation in the *a-b* plane.
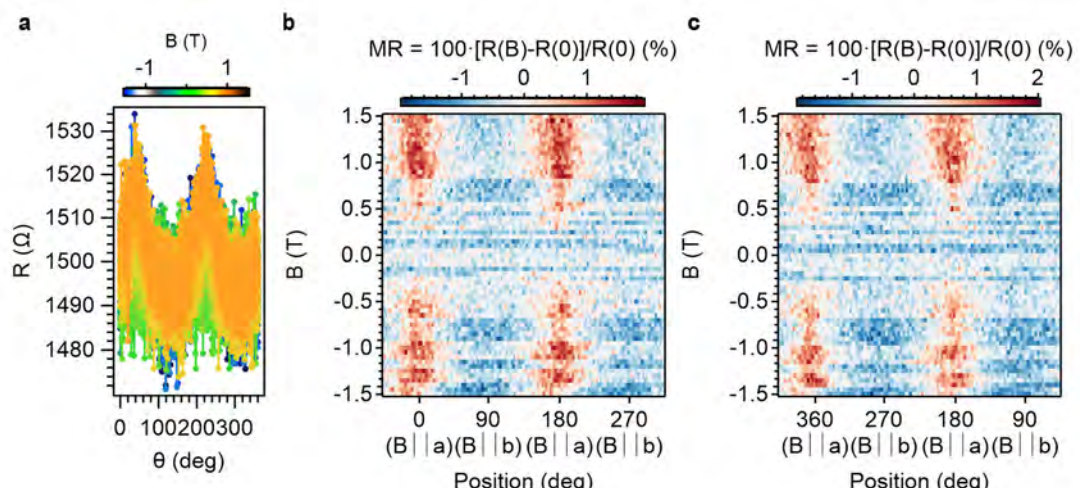

Figure S.82.- Resistance dependence as a function of the angle for different magnetic fields (a) and 2D plots of the magnetoresistance as a function of the angle between the magnetic field and the direction of the current in the vdWH from 0º to 360º (b) and viceversa (c) at 50 K. Rotation in the *a-b* plane.

41
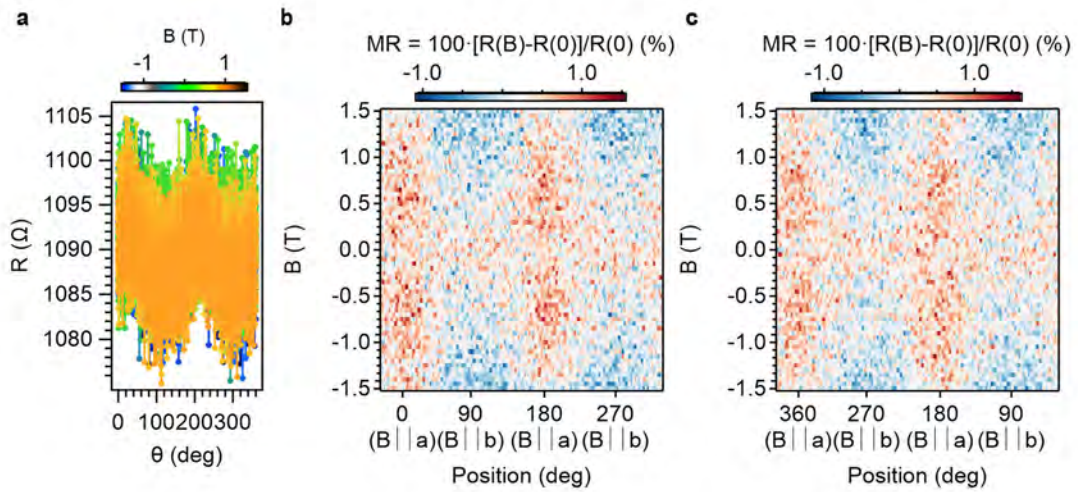
Figure S.83.- Resistance dependence as a function of the angle for different magnetic fields (a) and 2D plots of the magnetoresistance as a function of the angle between the magnetic field and the direction of the current in the vdWH from 0º to 360º (b) and viceversa (c) at 100 K. Rotation in the *a-b* plane.
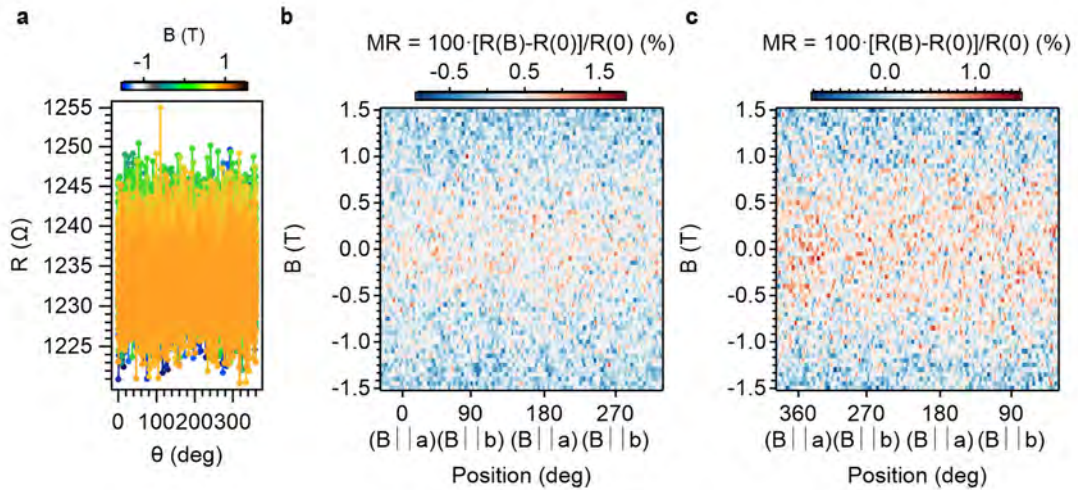

Figure S.84.- Resistance dependence as a function of the angle for different magnetic fields (a) and 2D plots of the magnetoresistance as a function of the angle between the magnetic field and the direction of the current in the vdWH from 0º to 360º (b) and viceversa (c) at 200 K. Rotation in the *a-b* plane.

3.4.6. Device A.6. (CrSBr monolayer).
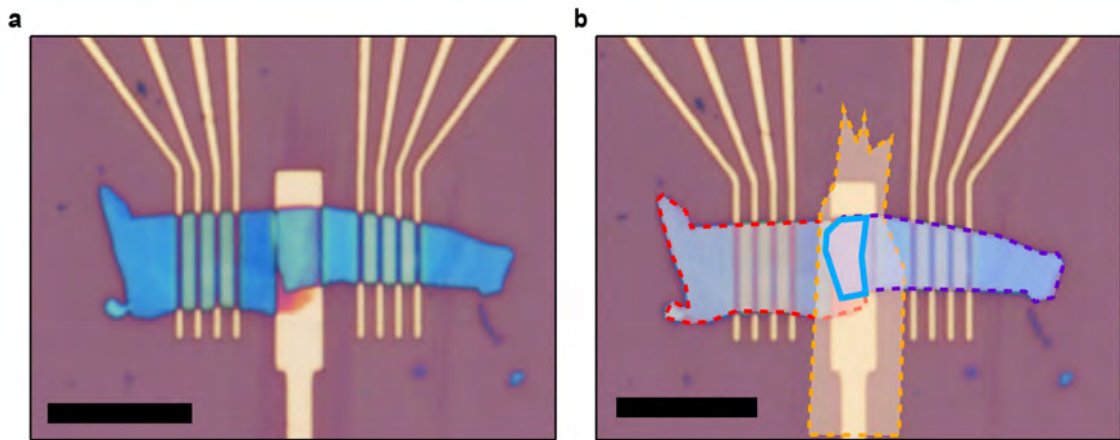
Figure S.85.- Optical picture of the device. For simplicity, the top TaS$_2$ contact has been highlighted in red, the bottom TaS$_2$ contact in purple and the CrSBr barrier in orange. The junction (blue area) is the overlapped area formed by the three different materials. Scale bar: 10 μm.
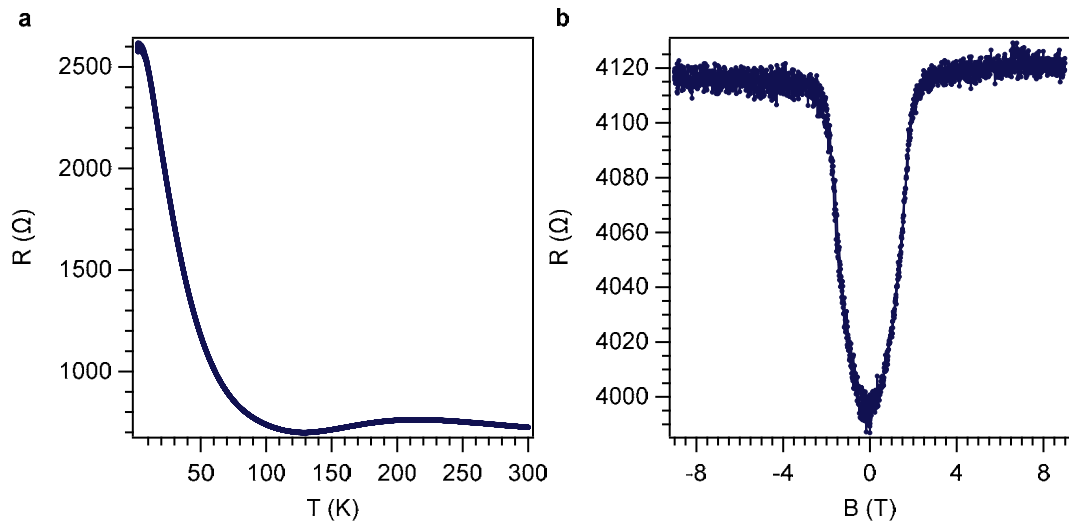

Figure S.86.- Resistance dependence as a function of the (a) temperature and resistance with the magnetic field parallel to the *a* axis (b).

3.4.7. Device B.1. (CrSBr bilayer).
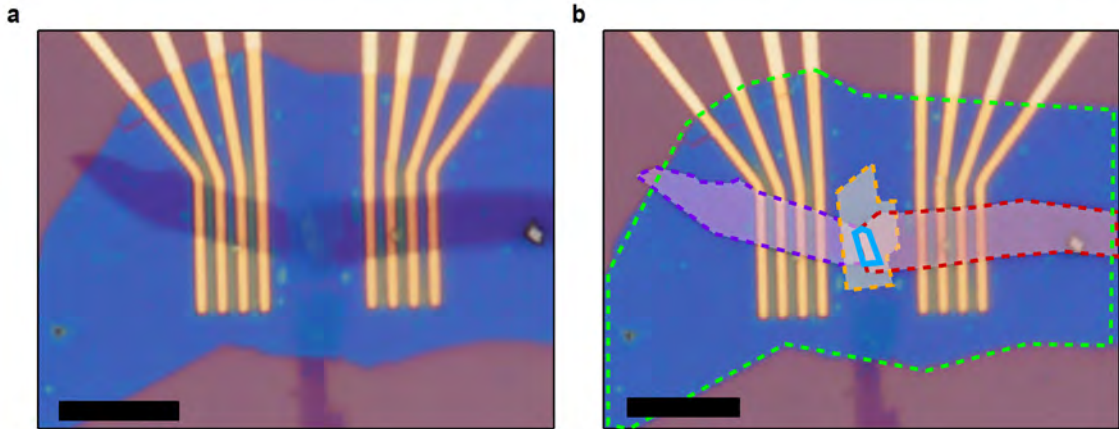
Figure S.87.- Optical picture of the device. For simplicity, the top graphite contact has been highlighted in red, the bottom graphite contact in purple and the CrSBr barrier in orange. h-BN is marked in green. The junction (blue area) is the overlapped area formed by the three different materials. Scale bar: 10 μm.
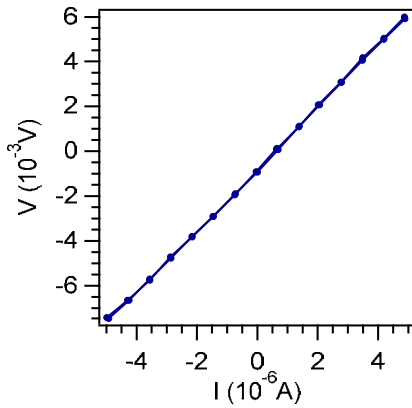

Figure S.88.- DC IV curve for the junction area at 2 K.
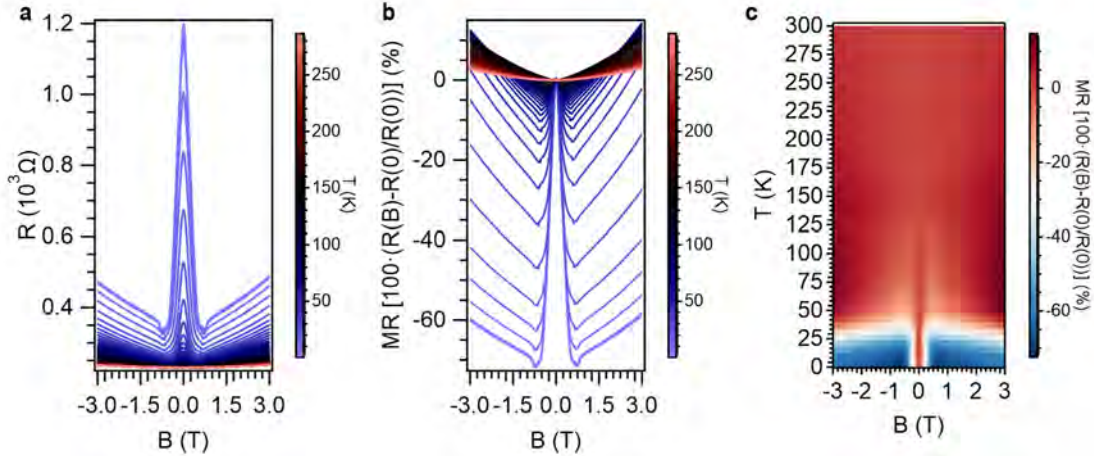
Figure S.89.- a) Resistance as a function of the magnetic field for different temperatures. b) Calculated magnetoresistance as a function of the magnetic field for different temperatures. c) Resistance plot as a function of temperature and magnetic field. Field parallel to the *a* axis.
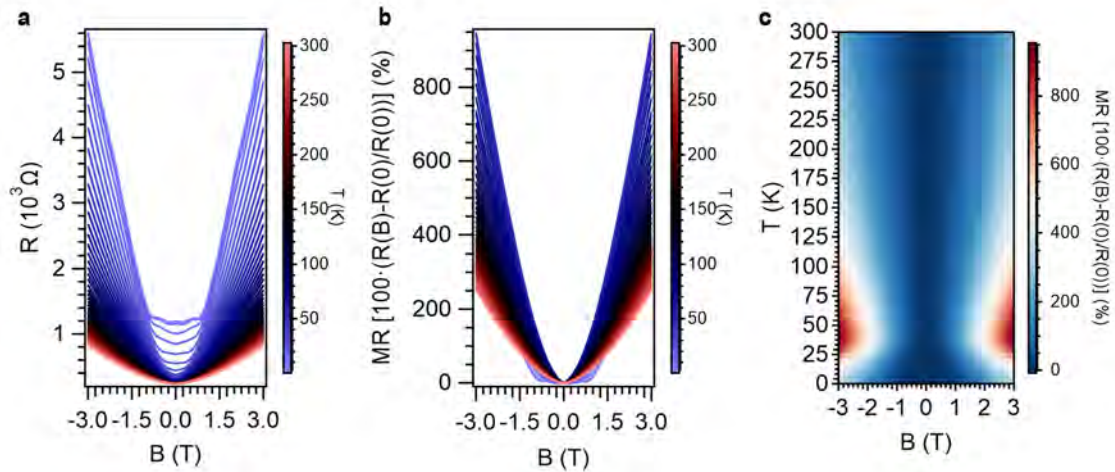
Figure S.90.- a) Resistance as a function of the magnetic field for different temperatures. b) Calculated magnetoresistance as a function of the magnetic field for different temperatures. c) Resistance plot as a function of temperature and magnetic field. Field parallel to the *c* axis.

3.4.8. Device B.2. (CrSBr bilayer).
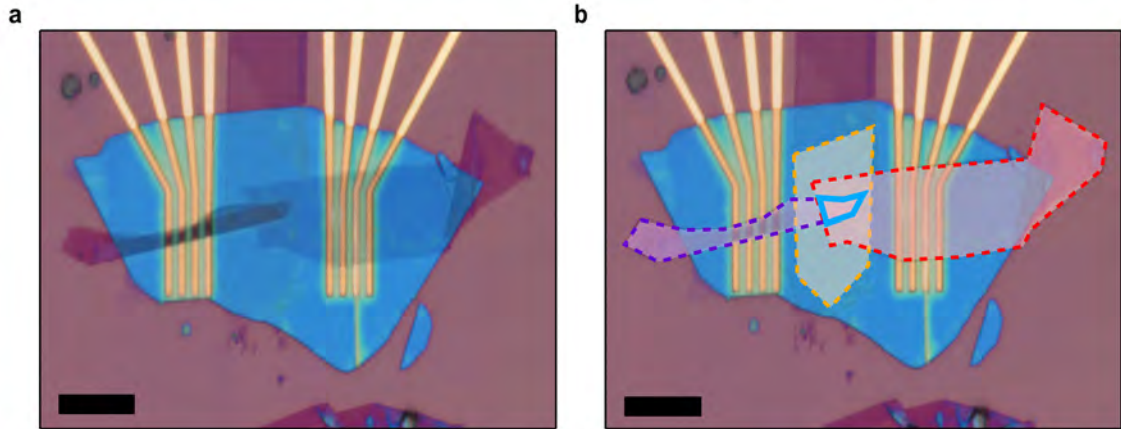
Figure S.91.- Optical picture of the device. For simplicity, the top graphite contact has been highlighted in red, the bottom graphite contact in purple and the CrSBr barrier in orange. h-BN is marked in green. The junction (blue area) is the overlapped area formed by the three different materials. Scale bar: 10 μm.
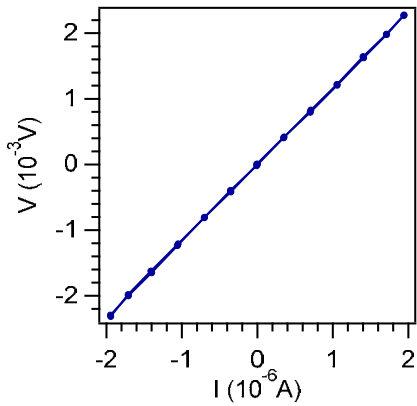

Figure S.92.- DC IV curve for the junction area at 2 K.
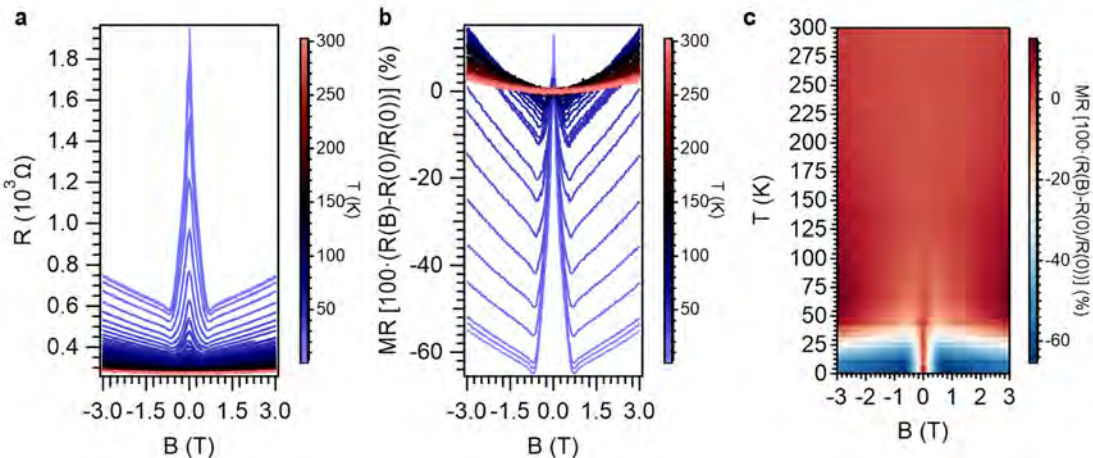
Figure S.93.- a) Resistance as a function of the magnetic field for different temperatures. b) Calculated magnetoresistance as a function of the magnetic field for different temperatures. c) Resistance plot as a function of temperature and magnetic field. Field parallel to the *a* axis.
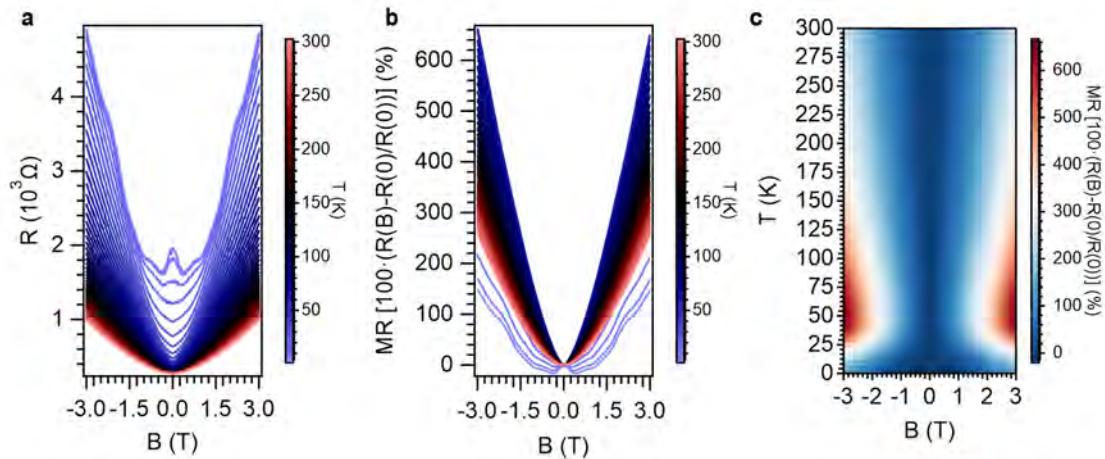
Figure S.94.- a) Resistance as a function of the magnetic field for different temperatures. b) Calculated magnetoresistance as a function of the magnetic field for different temperatures. c) Resistance plot as a function of temperature and magnetic field. Field parallel to the *c* axis.

3.4.9. Device B.3. (CrSBr bilayer).
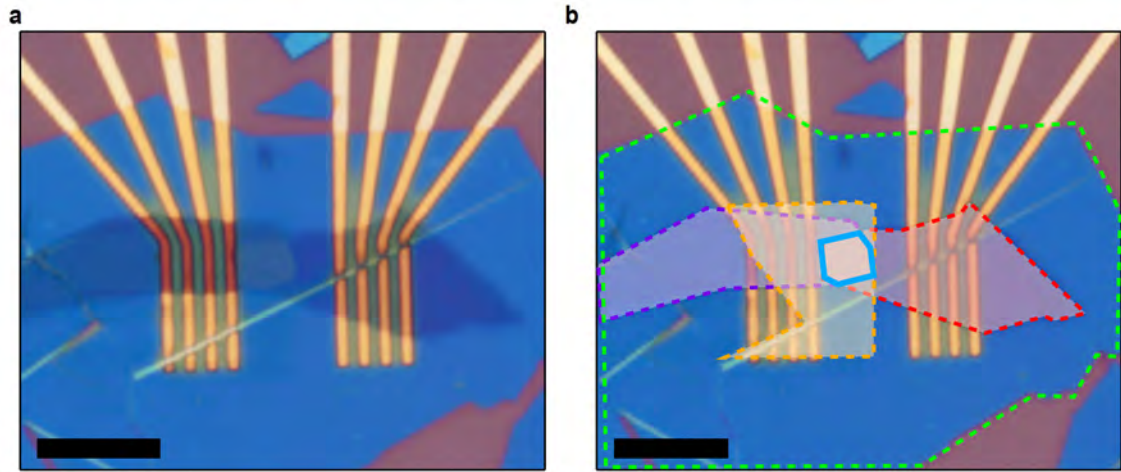
Figure S.95.- Optical picture of the device. For simplicity, the top graphite contact has been highlighted in red, the bottom graphite contact in purple and the CrSBr barrier in orange. h-BN is marked in green. The junction (blue area) is the overlapped area formed by the three different materials. Scale bar: 10 μm.
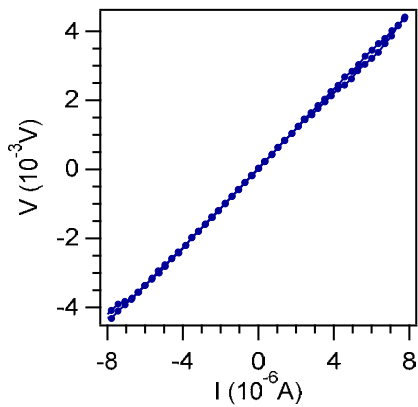
**Figure S.96.-** DC IV curve for the junction area at 2 K.
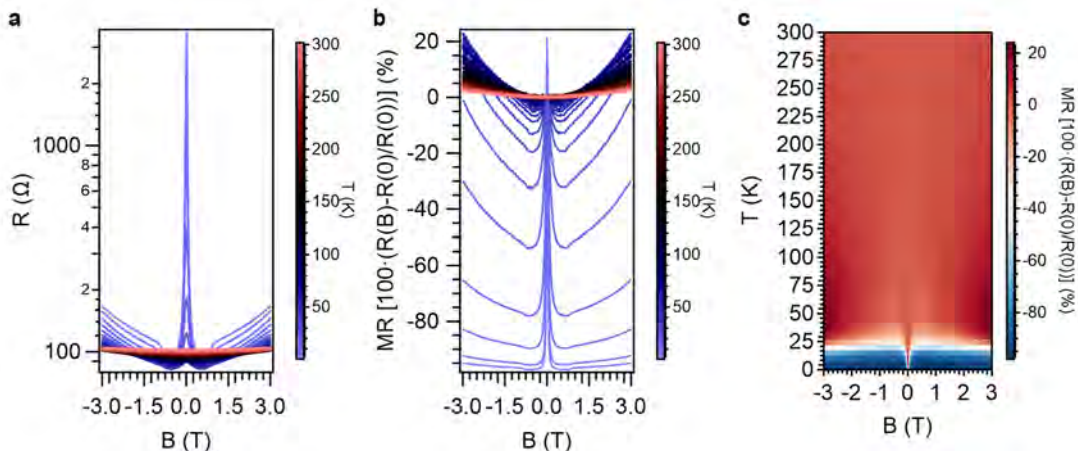
Figure S.97.- a) Resistance as a function of the magnetic field for different temperatures. b) Calculated magnetoresistance as a function of the magnetic field for different temperatures. c) Resistance plot as a function of temperature and magnetic field. Field parallel to the *a* axis.

48
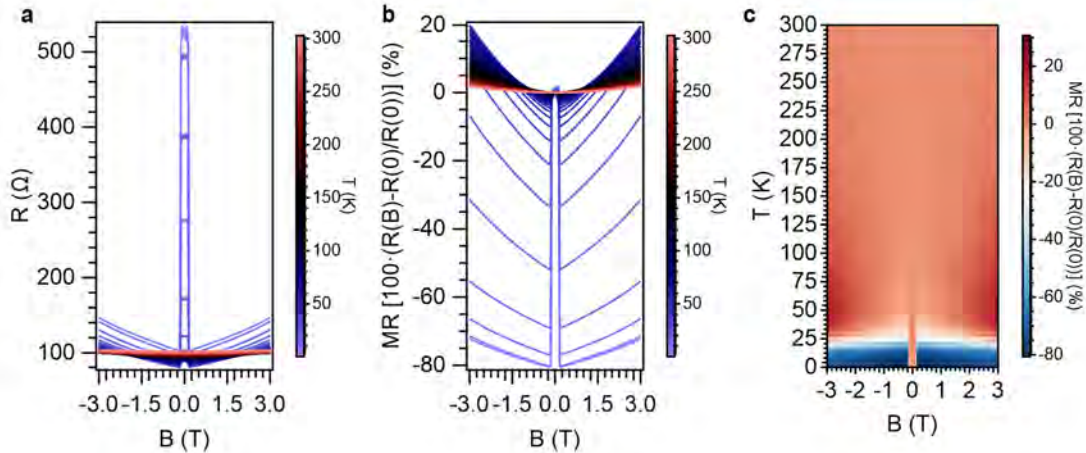
Figure S.98.- a) Resistance as a function of the magnetic field for different temperatures. b) Calculated magnetoresistance as a function of the magnetic field for different temperatures. c) Resistance plot as a function of temperature and magnetic field. Field parallel to the *b* axis.
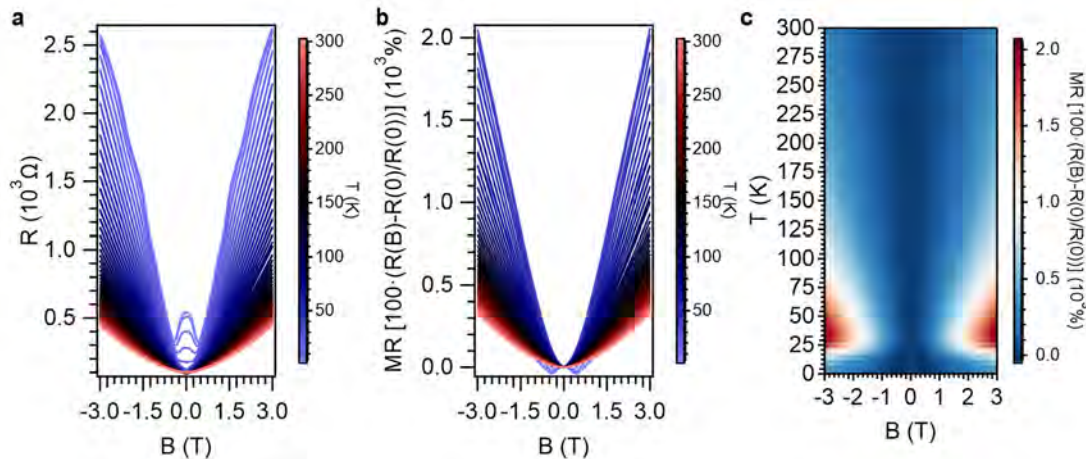

Figure S.99.- a) Resistance as a function of the magnetic field for different temperatures. b) Calculated magnetoresistance as a function of the magnetic field for different temperatures. c) Resistance plot as a function of temperature and magnetic field. Field parallel to the *c* axis.
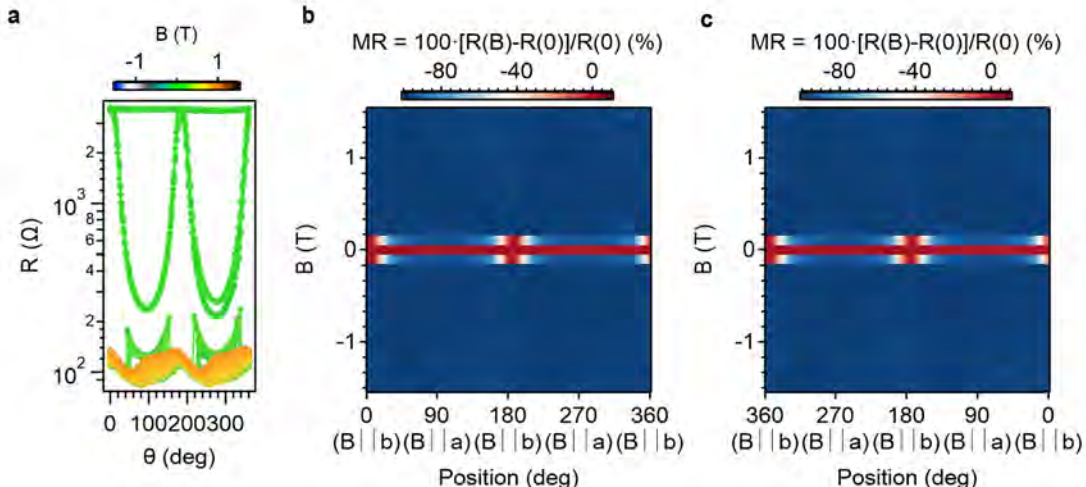
Figure S.100.- Resistance dependence (log) as a function of the angle for different magnetic fields (a) and 2D plots of the magnetoresistance as a function of the angle between the magnetic field and the direction of the current in the vdWH from 0º to 360º (b) and viceversa (c) at 2 K. Rotation in the *a-b* plane.

49
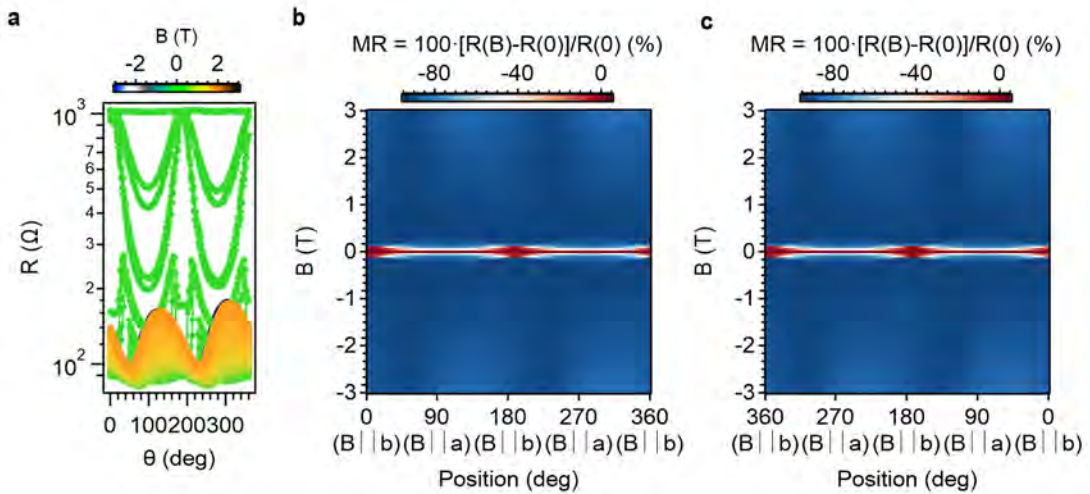
Figure S.101.- Resistance dependence (log) as a function of the angle for different magnetic fields (a) and 2D plots of the magnetoresistance as a function of the angle between the magnetic field and the direction of the current in the vdWH from 0º to 360º (b) and viceversa (c) at 10 K. Rotation in the *a-b* plane.
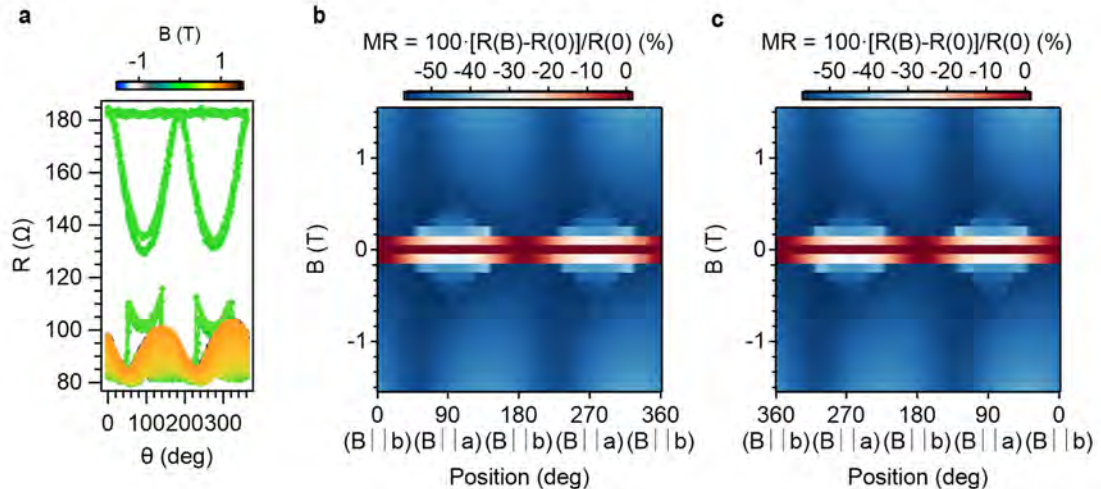
**Figure S.102.-** Resistance dependence as a function of the angle for different magnetic fields (a) and 2D plots of the magnetoresistance as a function of the angle between the magnetic field and the direction of the current in the vdWH from 0º to 360º (b) and viceversa (c) at 20 K. Rotation in the *a-b* plane.
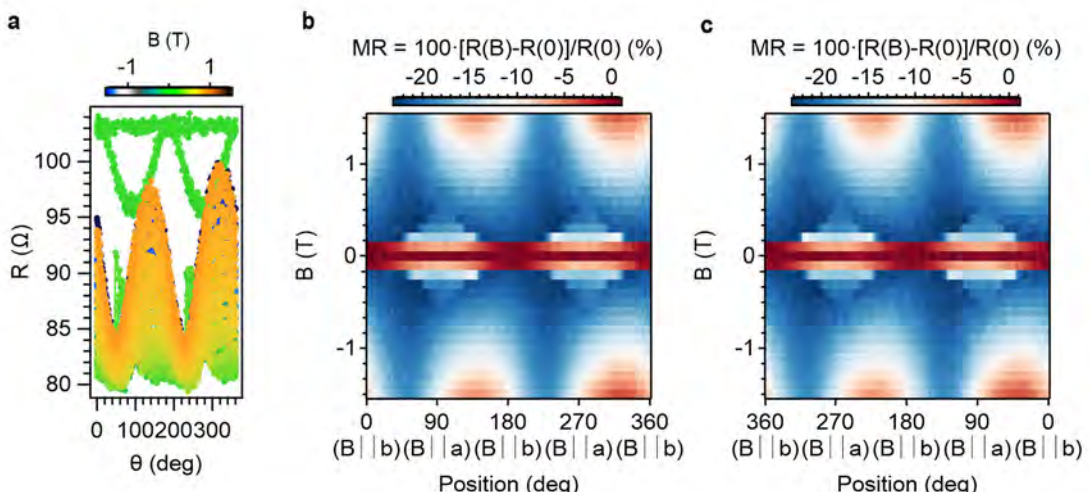
Figure S.103.- Resistance dependence as a function of the angle for different magnetic fields (a) and 2D plots of the magnetoresistance as a function of the angle between the magnetic field and the direction of the current in the vdWH from 0º to 360º (b) and viceversa (c) at 30 K. Rotation in the *a-b* plane.

3.4.10. Device B.4. (CrSBr bilayer).
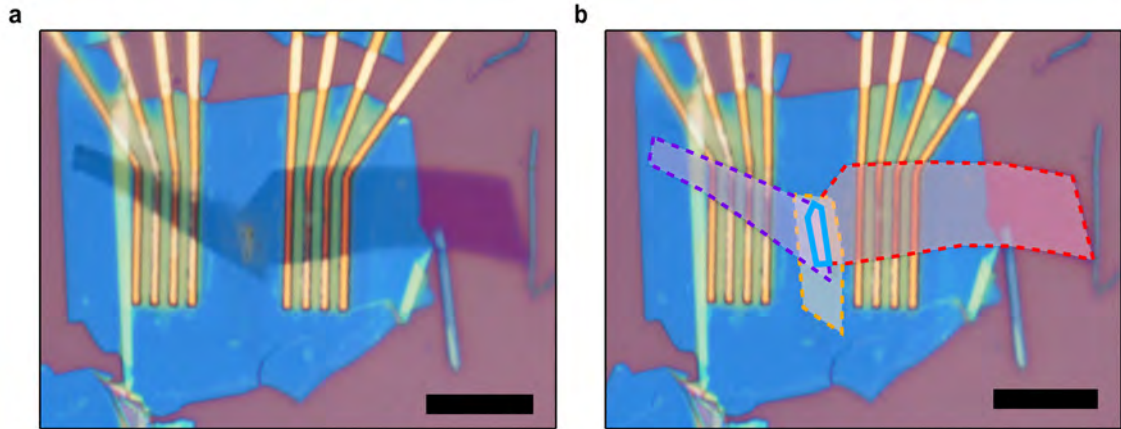
Figure S.104.- Optical picture of the device. For simplicity, the top graphite contact has been highlighted in red, the bottom graphite contact in purple and the CrSBr barrier in orange. h-BN is marked in green. The junction (blue area) is the overlapped area formed by the three different materials. Scale bar: 10 μm.
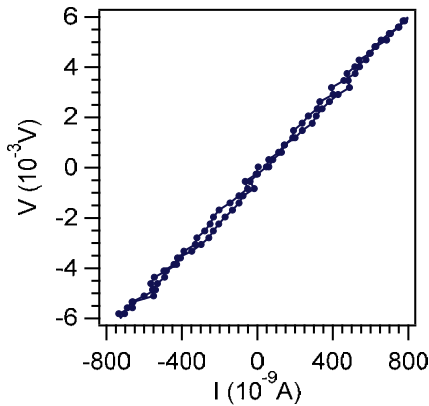
Figure S.105.- DC IV curve for the junction area at 10 K.
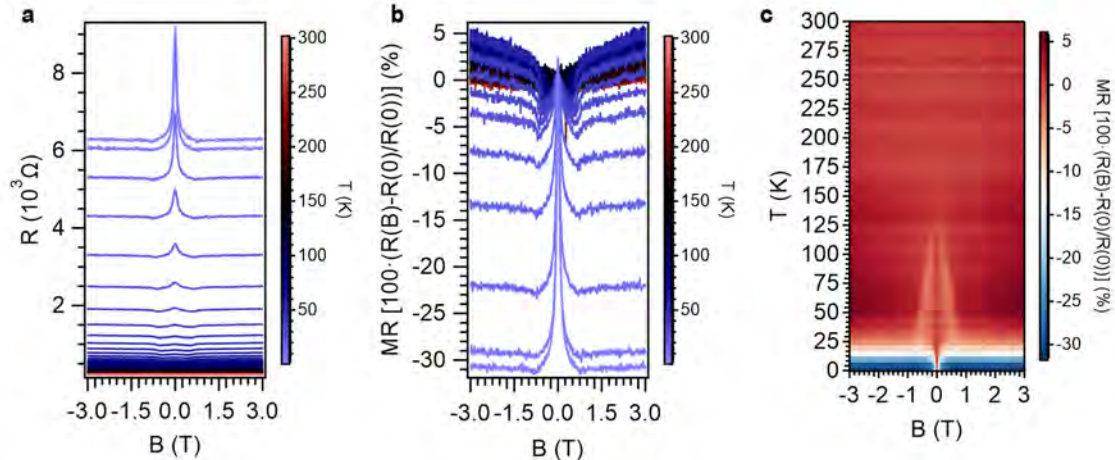
Figure S.106.- a) Resistance as a function of the magnetic field for different temperatures. b) Calculated magnetoresistance as a function of the magnetic field for different temperatures. c) Resistance plot as a function of temperature and magnetic field. Field parallel to the *a* axis.
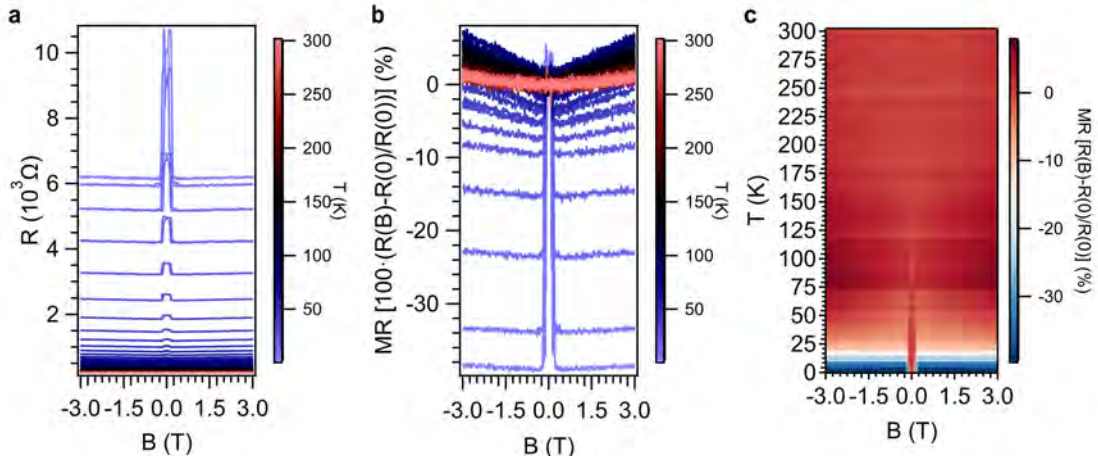
Figure S.107.- a) Resistance as a function of the magnetic field for different temperatures. b) Calculated magnetoresistance as a function of the magnetic field for different temperatures. c) Resistance plot as a function of temperature and magnetic field. Field parallel to the *b* axis.
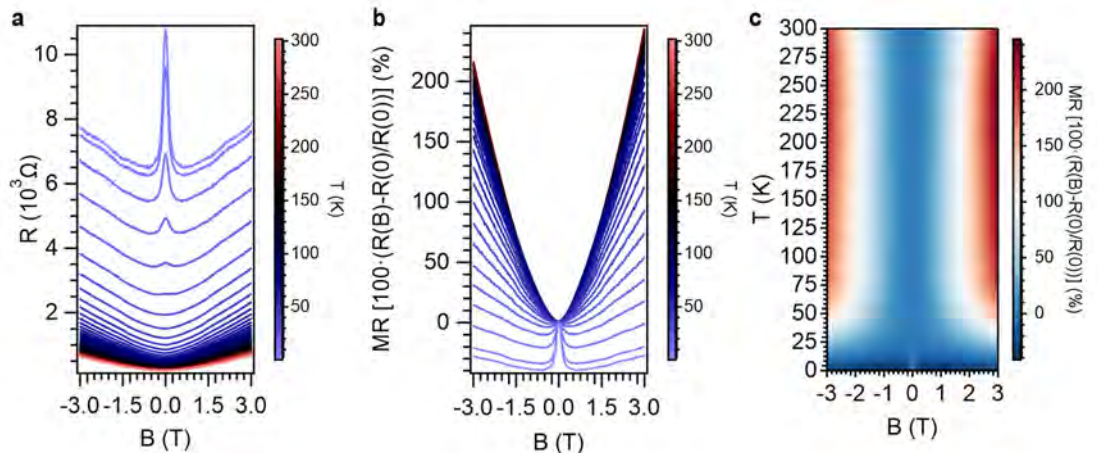
Figure S.108.- a) Resistance as a function of the magnetic field for different temperatures. b) Calculated magnetoresistance as a function of the magnetic field for different temperatures. c) Resistance plot as a function of temperature and magnetic field. Field parallel to the *c* axis.
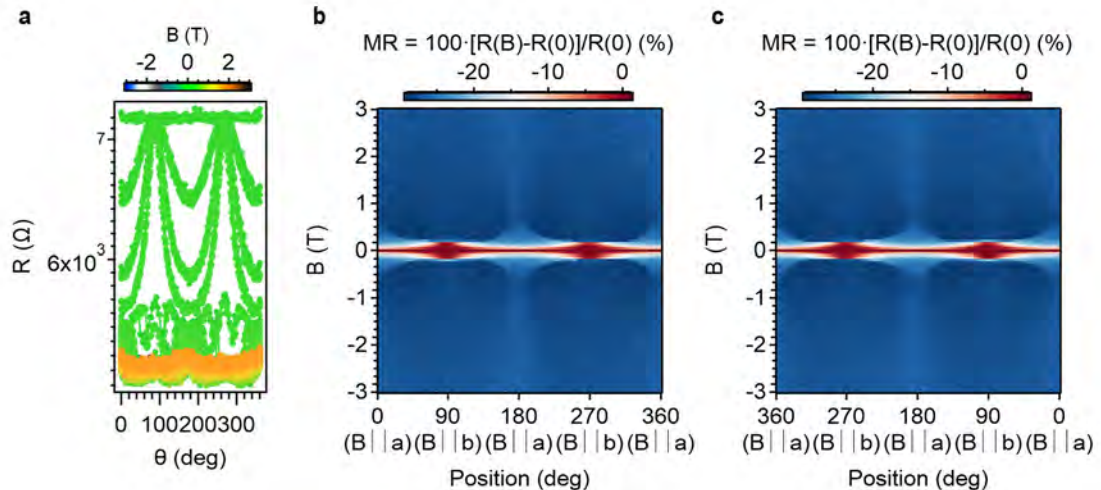
Figure S.109.- Resistance dependence as a function of the angle for different magnetic fields (a) and 2D plots of the magnetoresistance as a function of the angle between the magnetic field and the direction of the current in the vdWH from 0º to 360º (b) and viceversa (c) at 10 K. Rotation in the *a-b* plane.
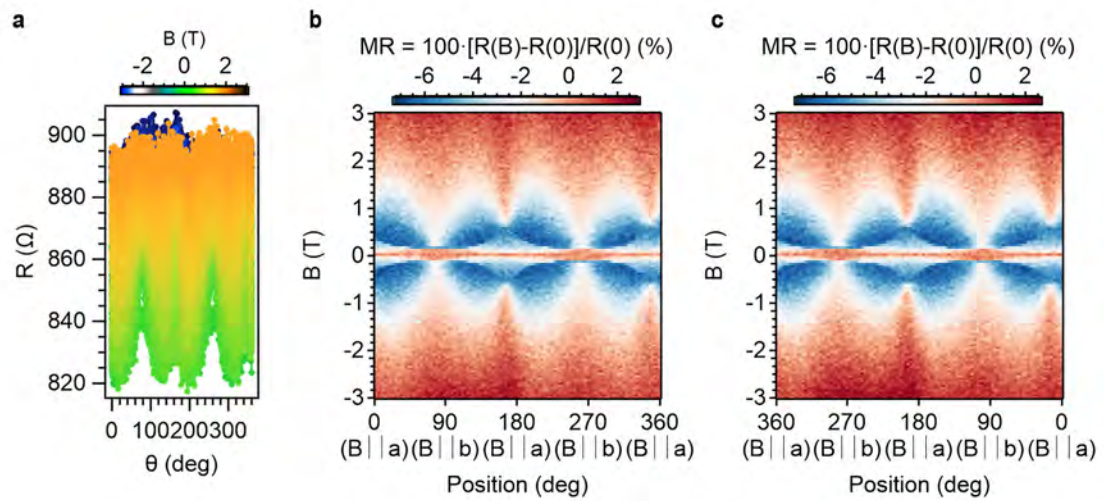
Figure S.110.- Resistance dependence (log) as a function of the angle for different magnetic fields (a) and 2D plots of the magnetoresistance as a function of the angle between the magnetic field and the direction of the current in the vdWH from 0º to 360º (b) and viceversa (c) at 50 K. Rotation in the *a-b* plane.

3.4.11. Device B.5. (CrSBr bilayer).
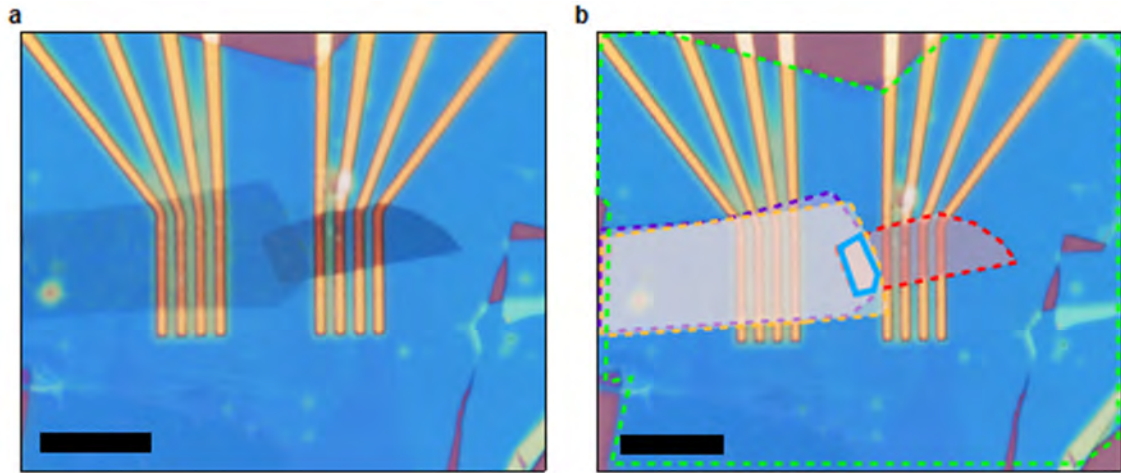
Figure S.111.- Optical picture of the device. For simplicity, the top graphite contact has been highlighted in red, the bottom graphite contact in purple and the CrSBr barrier in orange. h-BN is marked in green. The junction (blue area) is the overlapped area formed by the three different materials. Scale bar: 10 μm.
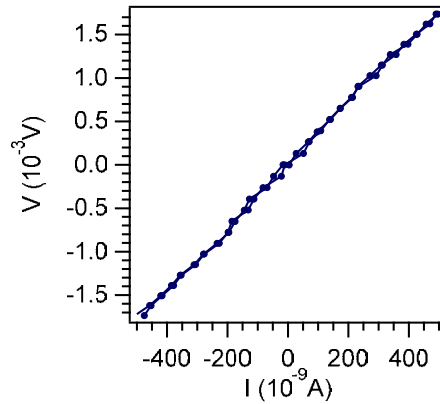
Figure S.112.- DC IV curve for the junction area at 2 K.
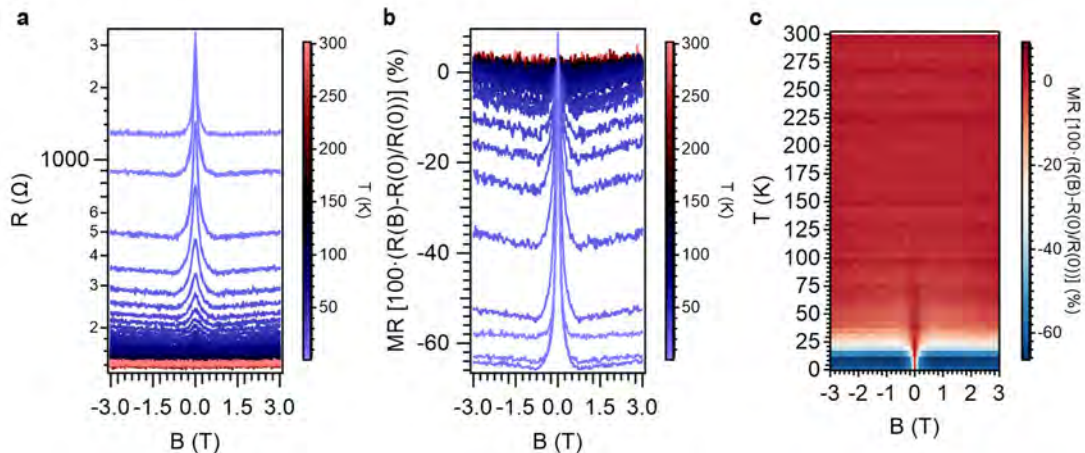
Figure S.113.- a) Resistance (log) as a function of the magnetic field for different temperatures. b) Calculated magnetoresistance as a function of the magnetic field for different temperatures. c) Resistance plot as a function of temperature and magnetic field. Field parallel to the *a* axis.
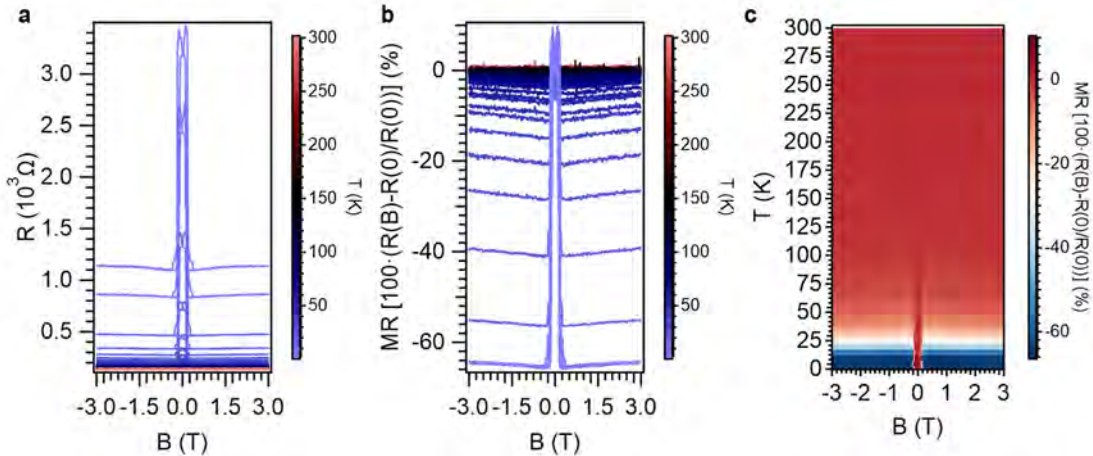
Figure S.114.- a) Resistance as a function of the magnetic field for different temperatures. b) Calculated magnetoresistance as a function of the magnetic field for different temperatures. c) Resistance plot as a function of temperature and magnetic field. Field parallel to the *b* axis.
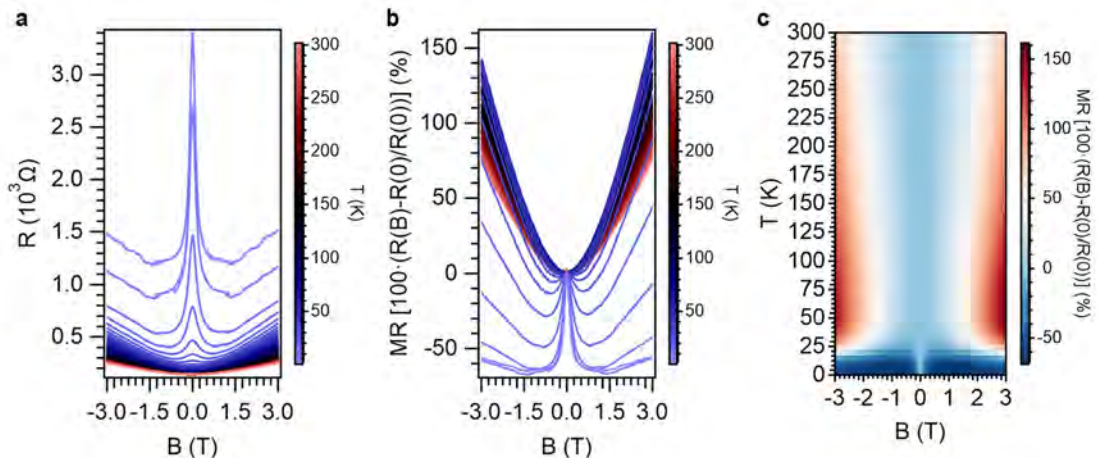
Figure S.115.- a) Resistance as a function of the magnetic field for different temperatures. b) Calculated magnetoresistance as a function of the magnetic field for different temperatures. c) Resistance plot as a function of temperature and magnetic field. Field parallel to the *c* axis.
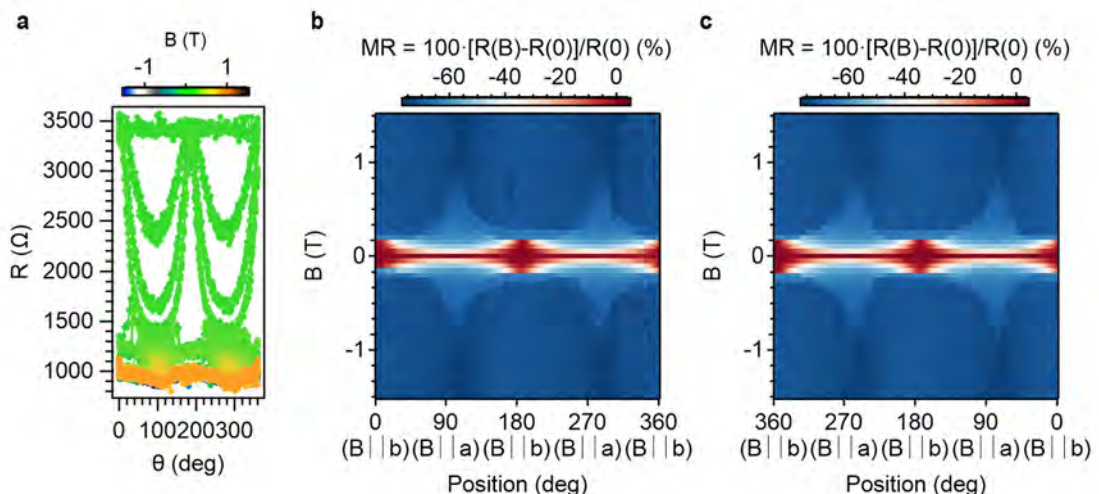

Figure S.116.- Resistance dependence as a function of the angle for different magnetic fields (a) and 2D plots of the magnetoresistance as a function of the angle between the magnetic field and the direction of the current in the vdWH from 0º to 360º (b) and viceversa (c) at 2 K. Rotation in the *a-b* plane.
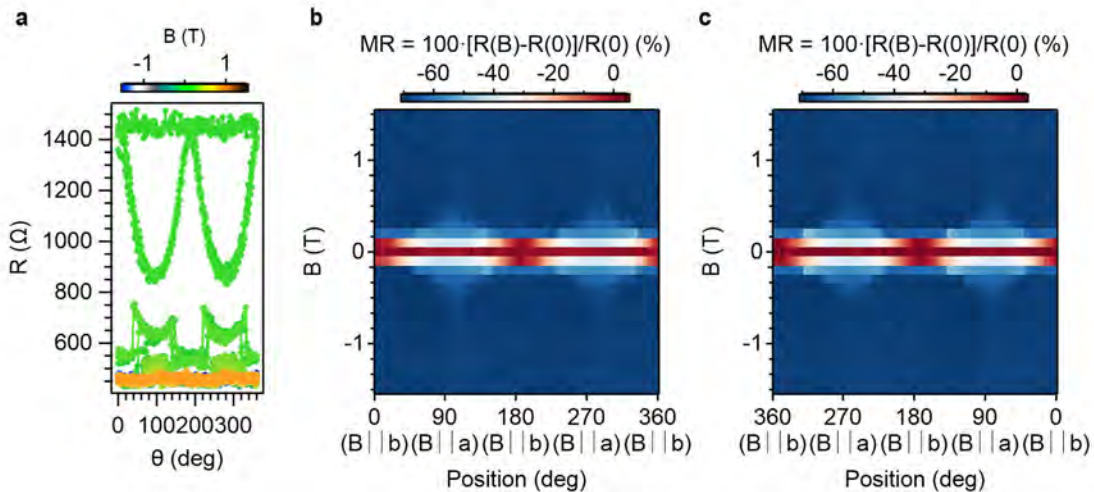
Figure S.117.- Resistance dependence as a function of the angle for different magnetic fields (a) and 2D plots of the magnetoresistance as a function of the angle between the magnetic field and the direction of the current in the vdWH from 0º to 360º (b) and viceversa (c) at 10 K. Rotation in the *a-b* plane.
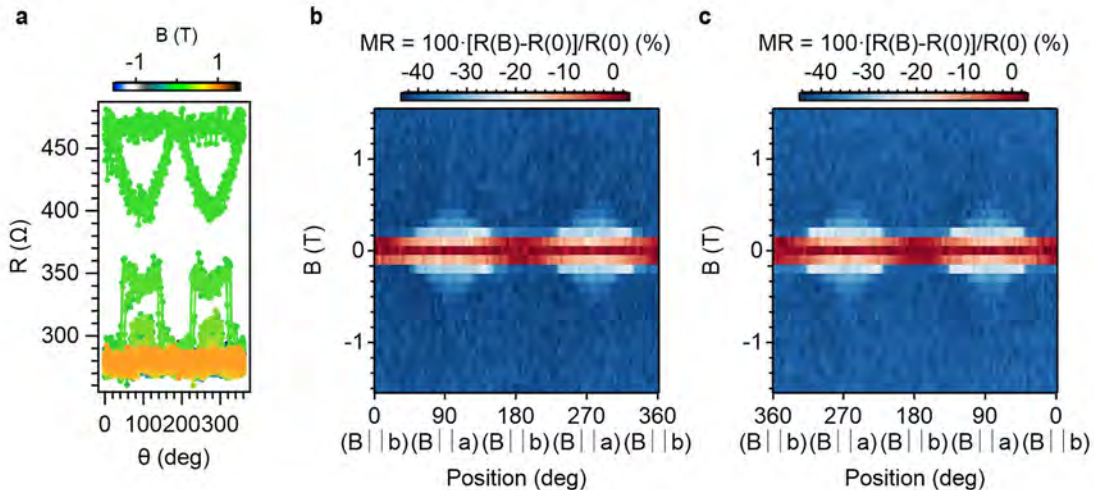
Figure S.118.- Resistance dependence as a function of the angle for different magnetic fields (a) and 2D plots of the magnetoresistance as a function of the angle between the magnetic field and the direction of the current in the vdWH from 0º to 360º (b) and viceversa (c) at 20 K. Rotation in the *a-b* plane.
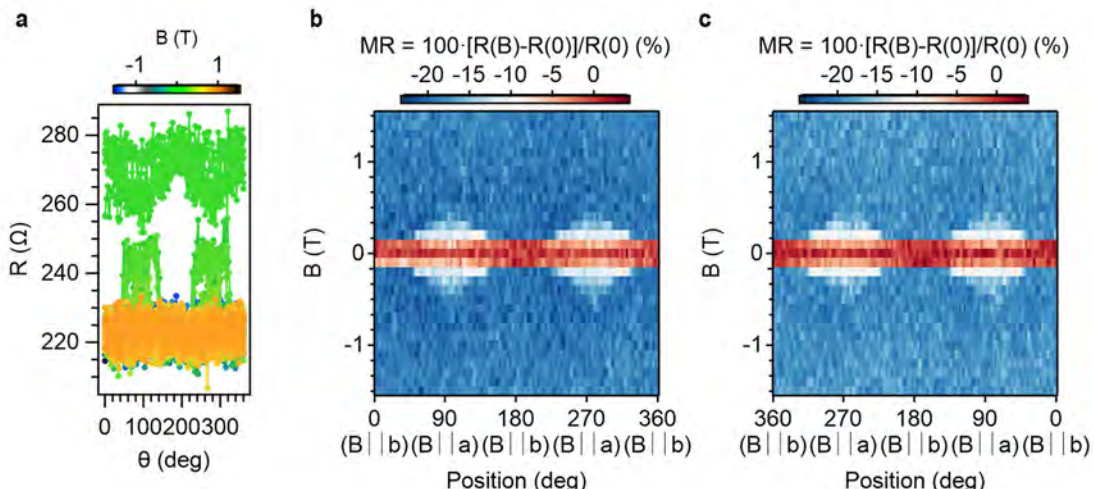
Figure S.119.- Resistance dependence as a function of the angle for different magnetic fields (a) and 2D plots of the magnetoresistance as a function of the angle between the magnetic field and the direction of the current in the vdWH from 0º to 360º (b) and viceversa (c) at 30 K. Rotation in the *a-b* plane.
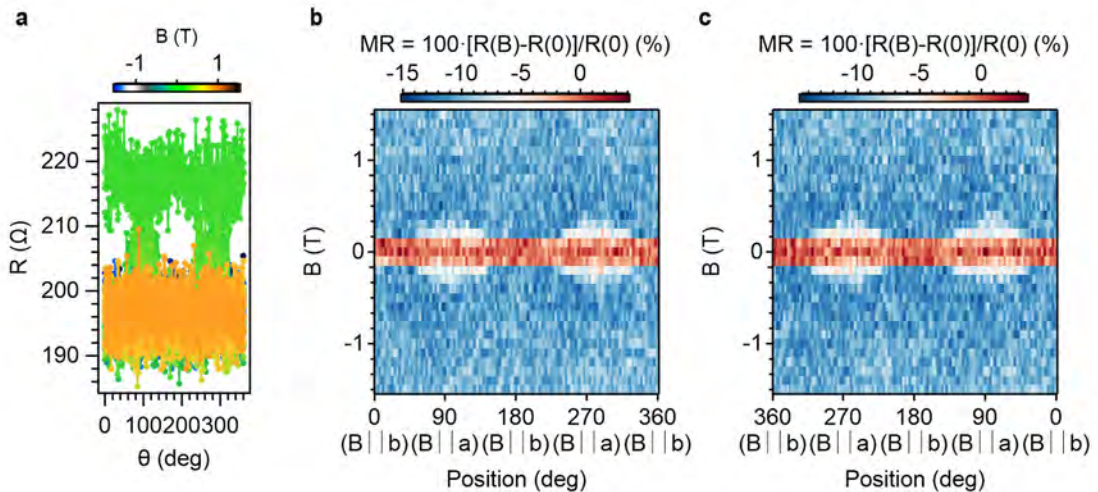
Figure S.120.- Resistance dependence as a function of the angle for different magnetic fields (a) and 2D plots of the magnetoresistance as a function of the angle between the magnetic field and the direction of the current in the vdWH from 0º to 360º (b) and viceversa (c) at 40 K. Rotation in the *a-b* plane.
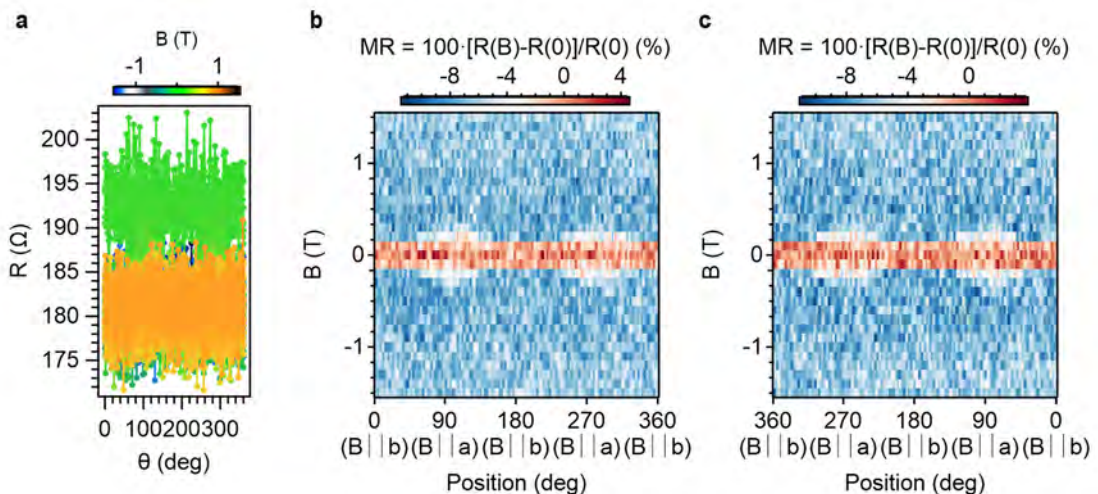

Figure S.121.- Resistance dependence as a function of the angle for different magnetic fields (a) and 2D plots of the magnetoresistance as a function of the angle between the magnetic field and the direction of the current in the vdWH from 0º to 360º (b) and viceversa (c) at 50 K. Rotation in the *a-b* plane.
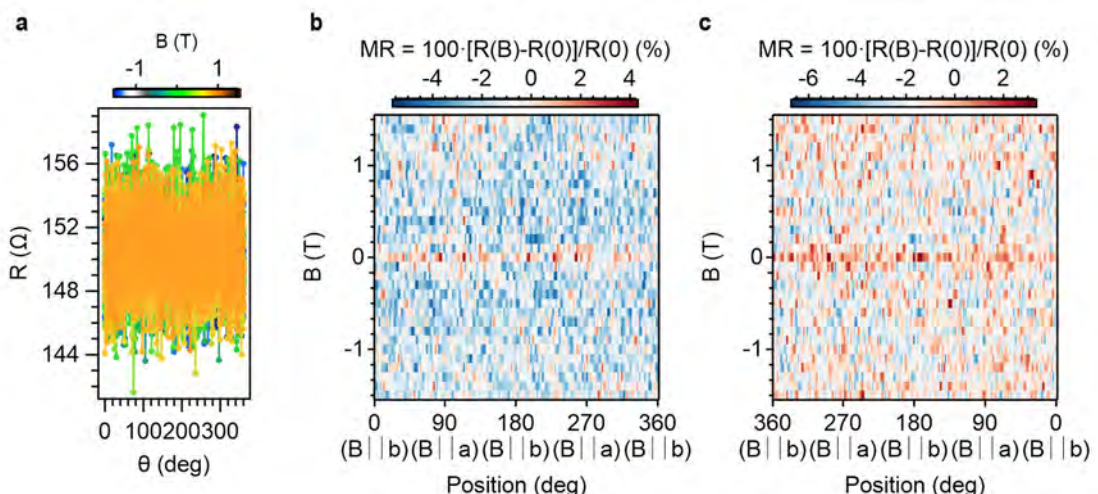
Figure S.122.- Resistance dependence as a function of the angle for different magnetic fields (a) and 2D plots of the magnetoresistance as a function of the angle between the magnetic field and the direction of the current in the vdWH from 0º to 360º (b) and viceversa (c) at 100 K. Rotation in the *a-b* plane.
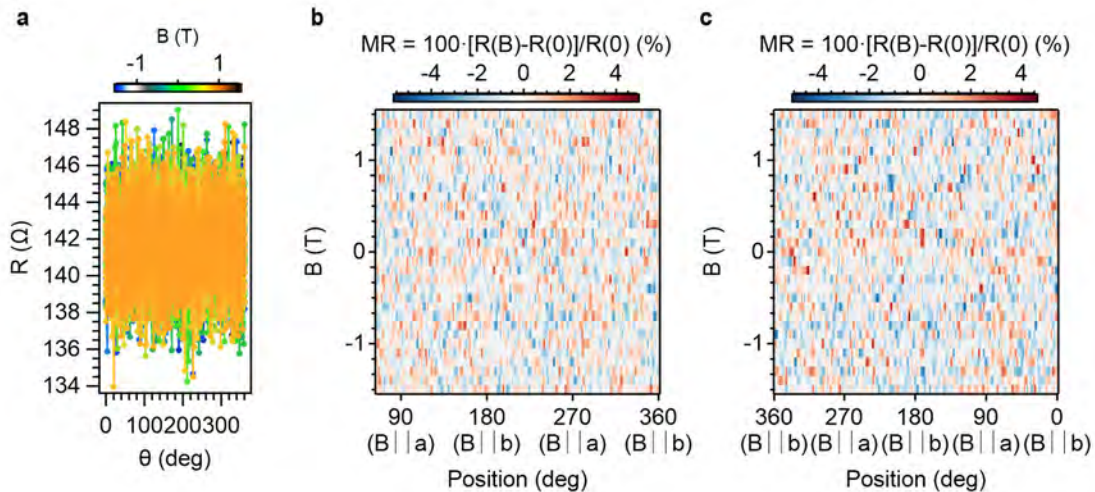
Figure S.123.- Resistance dependence as a function of the angle for different magnetic fields (a) and 2D plots of the magnetoresistance as a function of the angle between the magnetic field and the direction of the current in the vdWH from 0o to 360o (b) and viceversa (c) at 150 K. Rotation in the *a-b* plane.
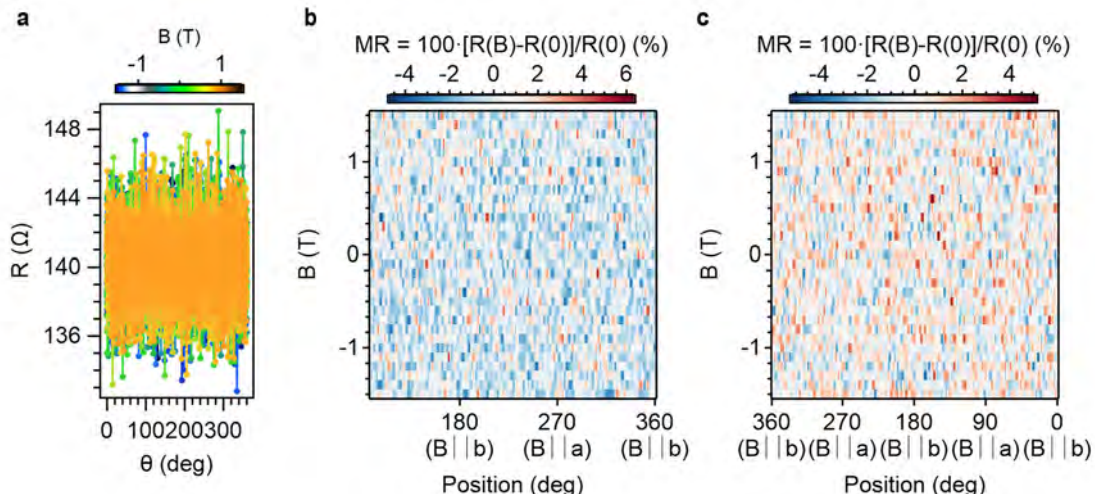

Figure S.124.- Resistance dependence as a function of the angle for different magnetic fields (a) and 2D plots of the magnetoresistance as a function of the angle between the magnetic field and the direction of the current in the vdWH from 0o to 360o (b) and viceversa (c) at 200 K. Rotation in the *a-b* plane.

3.4.12. Device B.6. (CrSBr bilayer).
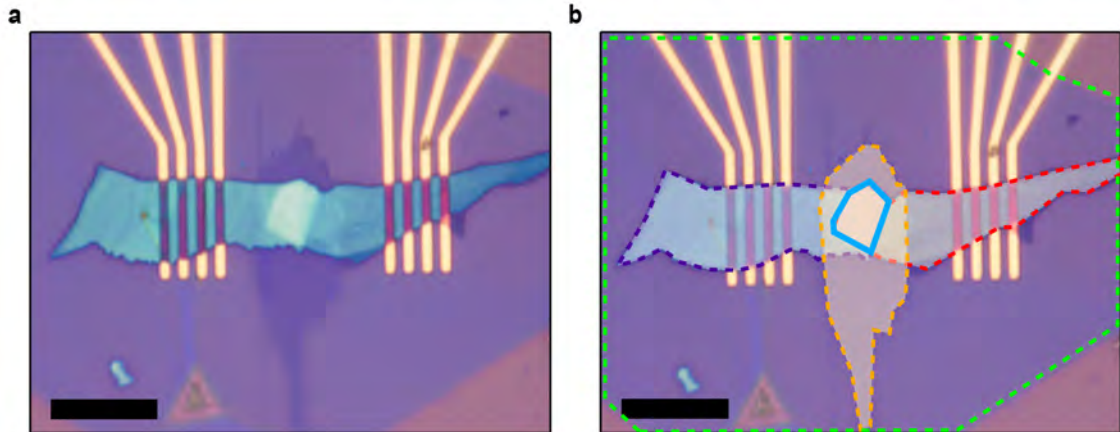
Figure S.125.- Optical picture of the device. For simplicity, the top NbSe$_2$ contact has been highlighted in red, the bottom NbSe$_2$ contact in purple and the CrSBr barrier in orange. h-BN is marked in green. The junction (blue area) is the overlapped area formed by the three different materials. Scale bar: 10 μm.
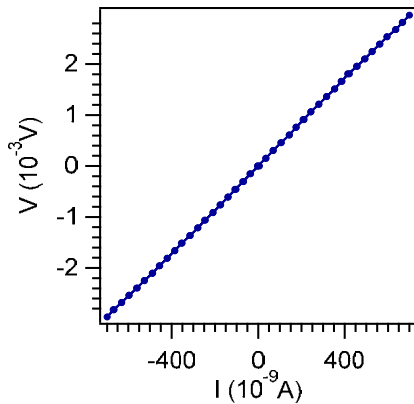
Figure S.126.- DC IV curve for the junction area at 10 K.
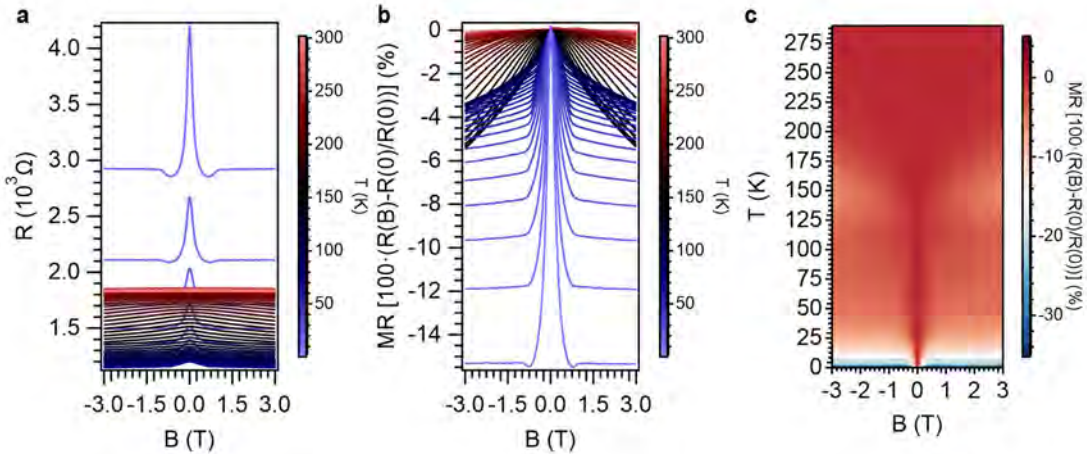
Figure S.127.- a) Resistance as a function of the magnetic field for different temperatures. b) Calculated magnetoresistance as a function of the magnetic field for different temperatures. c) Resistance plot as a function of temperature and magnetic field. Field parallel to the *a* axis.
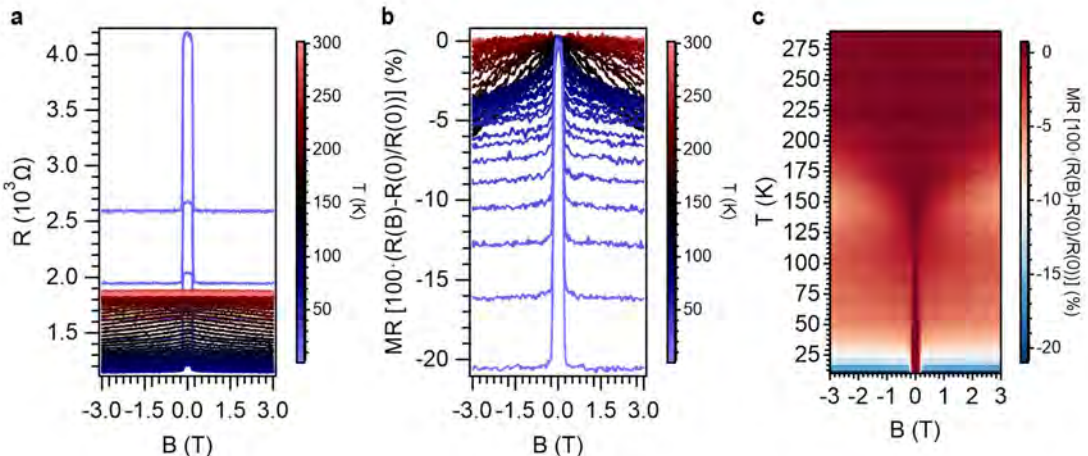
Figure S.128.- a) Resistance as a function of the magnetic field for different temperatures. b) Calculated magnetoresistance as a function of the magnetic field for different temperatures. c) Resistance plot as a function of temperature and magnetic field. Field parallel to the *b* axis.
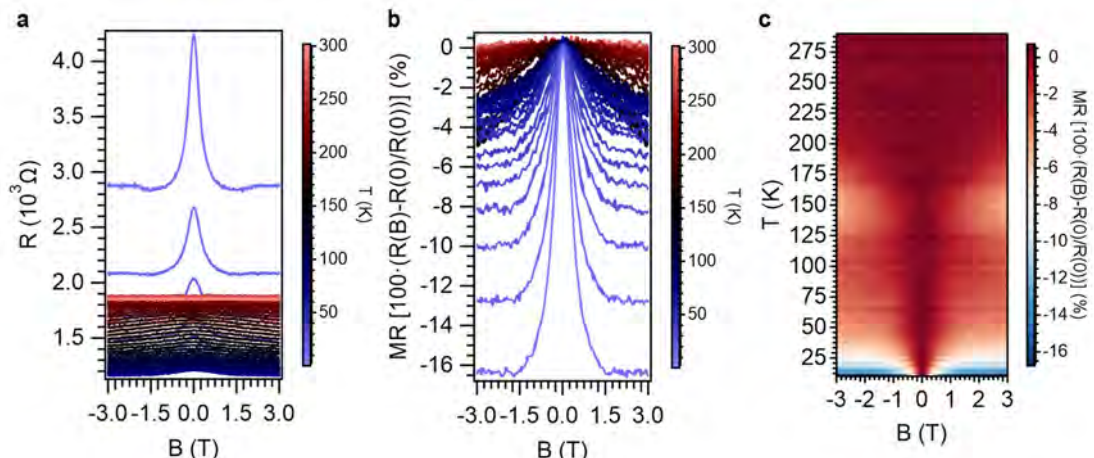
Figure S.129.- a) Resistance as a function of the magnetic field for different temperatures. b) Calculated magnetoresistance as a function of the magnetic field for different temperatures. c) Resistance plot as a function of temperature and magnetic field. Field parallel to the *c* axis.
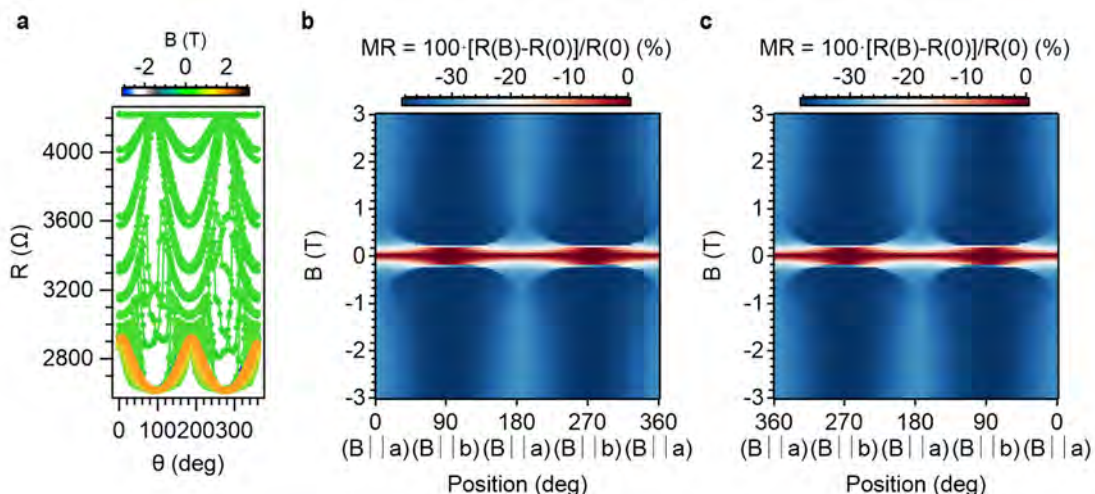

Figure S.130.- Resistance dependence as a function of the angle for different magnetic fields (a) and 2D plots of the magnetoresistance as a function of the angle between the magnetic field and the direction of the current in the vdWH from 0º to 360º (b) and viceversa (c) at 10 K. Rotation in the a-b plane.

60
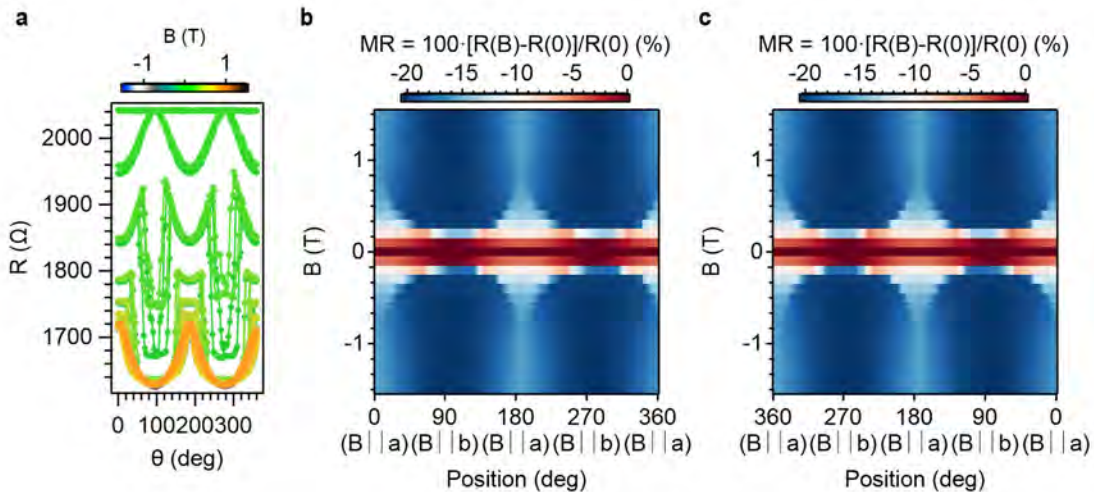
Figure S.131.- Resistance dependence as a function of the angle for different magnetic fields (a) and 2D plots of the magnetoresistance as a function of the angle between the magnetic field and the direction of the current in the vdWH from 0º to 360º (b) and viceversa (c) at 20 K. Rotation in the a-b plane.
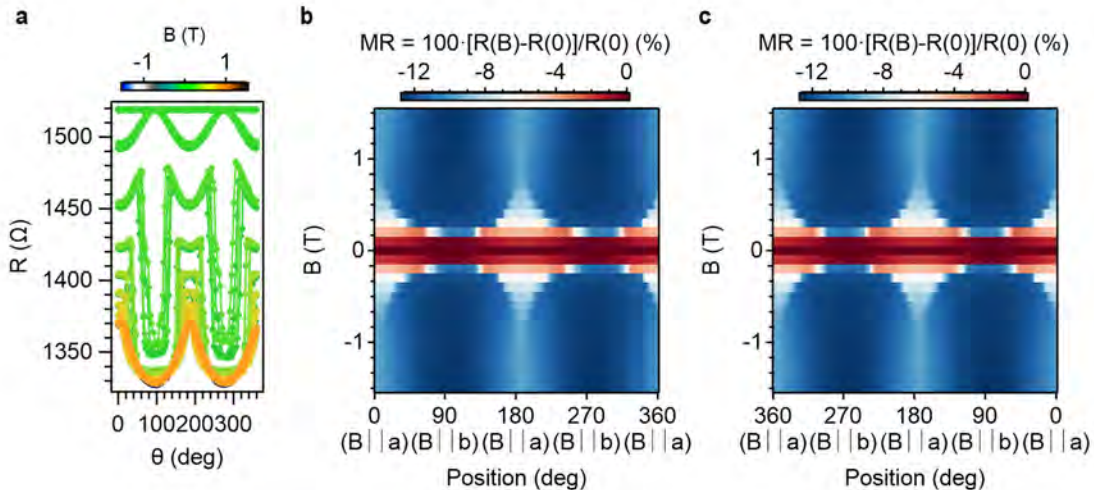
Figure S.132.- Resistance dependence as a function of the angle for different magnetic fields (a) and 2D plots of the magnetoresistance as a function of the angle between the magnetic field and the direction of the current in the vdWH from 0º to 360º (b) and viceversa (c) at 30 K. Rotation in the a-b plane.
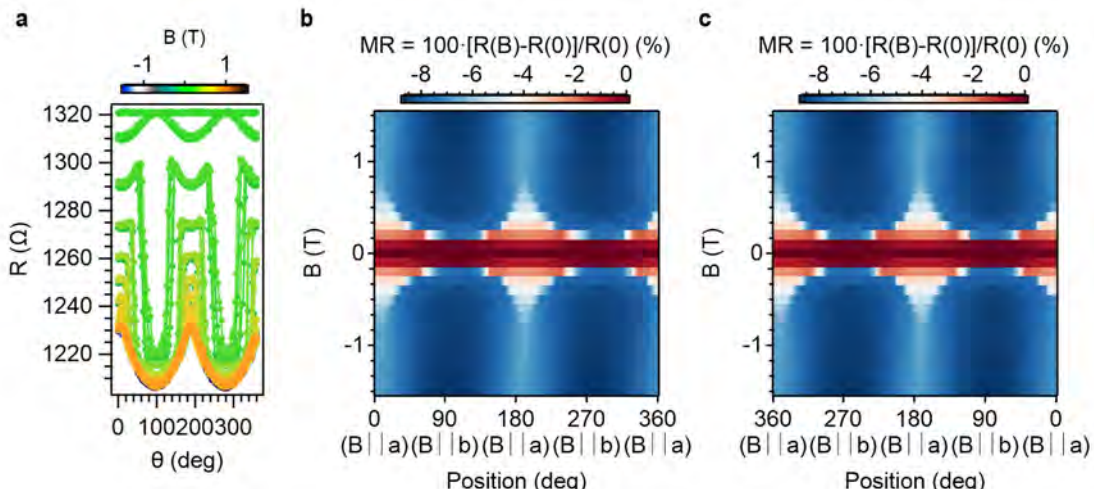
Figure S.133.- Resistance dependence as a function of the angle for different magnetic fields (a) and 2D plots of the magnetoresistance as a function of the angle between the magnetic field and the direction of the current in the vdWH from 0º to 360º (b) and viceversa (c) at 40 K. Rotation in the a-b plane.
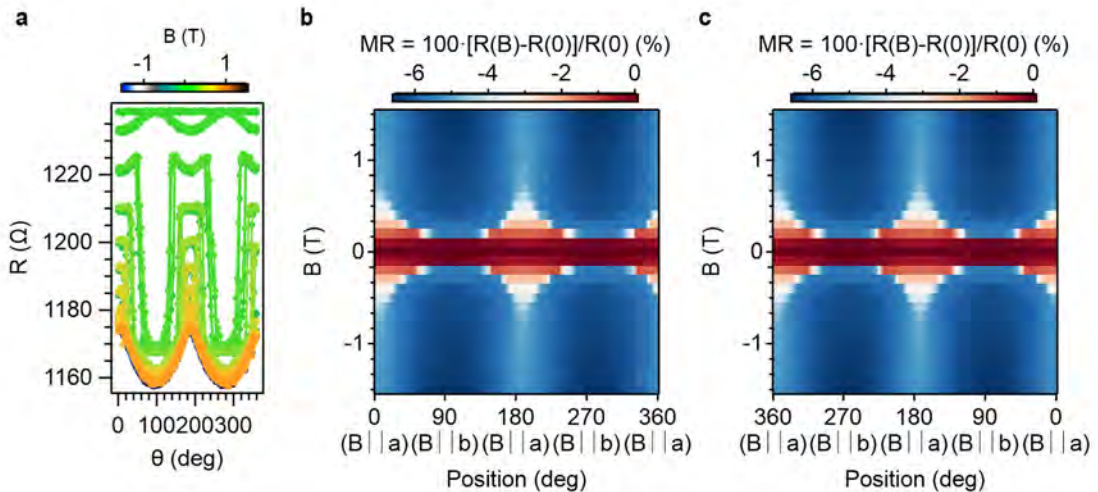
Figure S.134.- Resistance dependence as a function of the angle for different magnetic fields (a) and 2D plots of the magnetoresistance as a function of the angle between the magnetic field and the direction of the current in the vdWH from 0º to 360º (b) and viceversa (c) at 50 K. Rotation in the a-b plane.
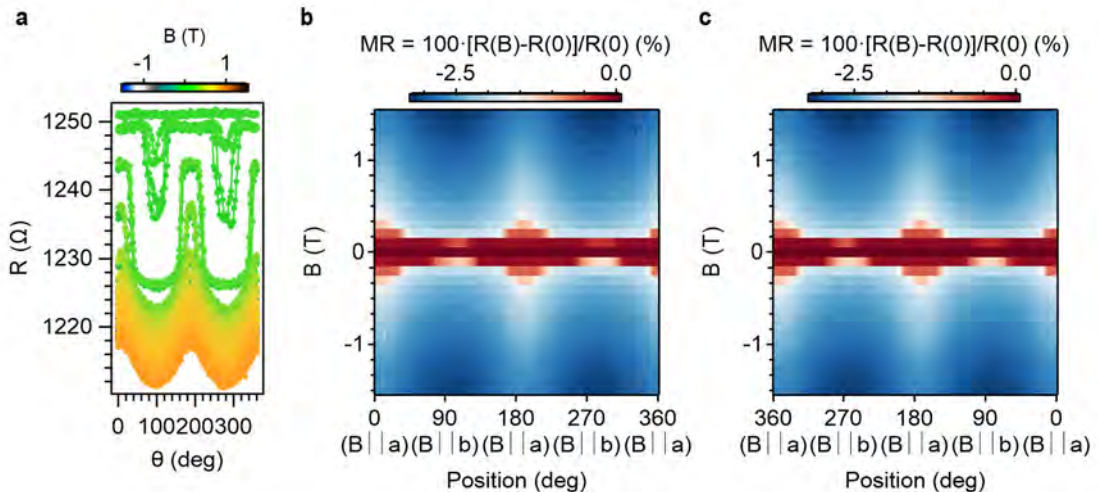
Figure S.135.- Resistance dependence as a function of the angle for different magnetic fields (a) and 2D plots of the magnetoresistance as a function of the angle between the magnetic field and the direction of the current in the vdWH from 0º to 360º (b) and viceversa (c) at 100 K. Rotation in the a-b plane.
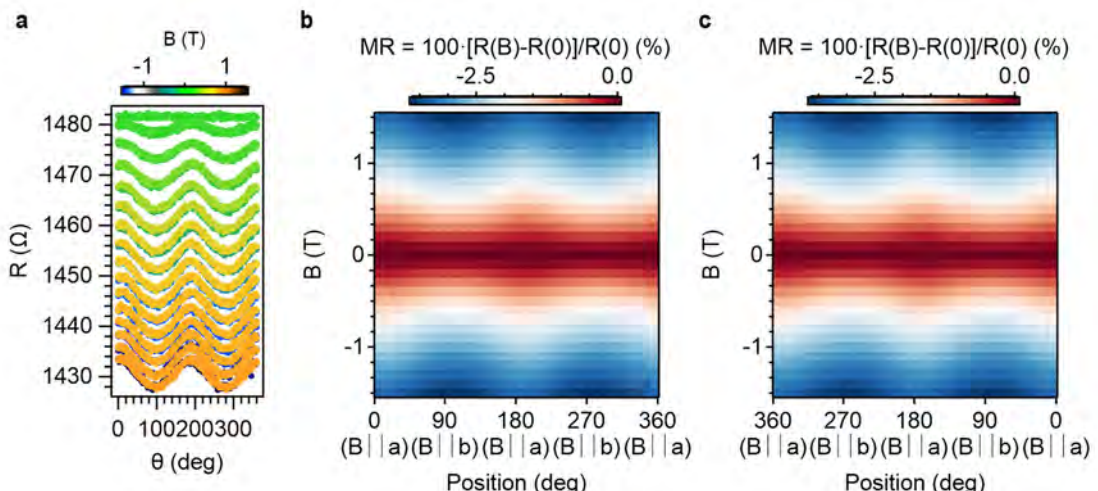

Figure S.136.- Resistance dependence as a function of the angle for different magnetic fields (a) and 2D plots of the magnetoresistance as a function of the angle between the magnetic field and the direction of the current in the vdWH from 0º to 360º (b) and viceversa (c) at 150 K. Rotation in the a-b plane.

62
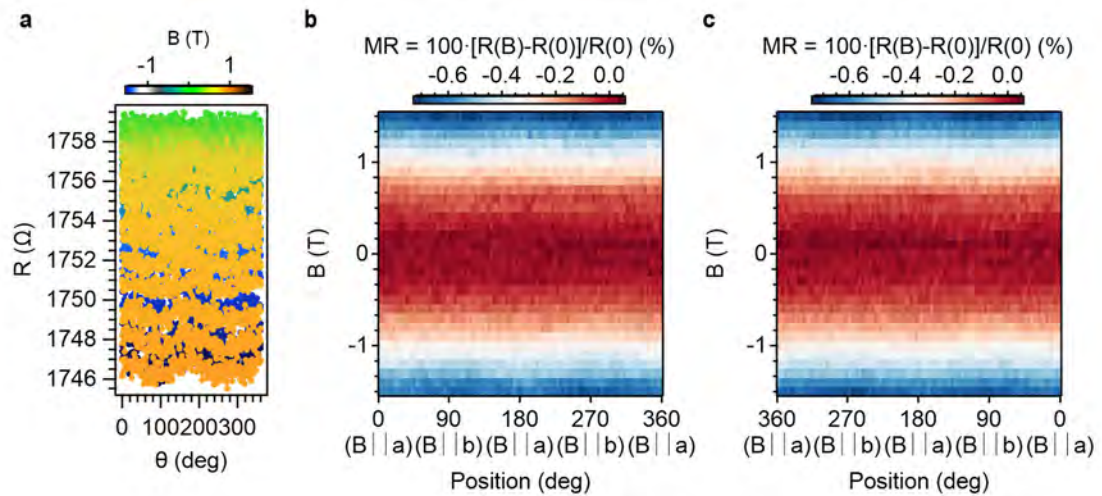
Figure S.137.- Resistance dependence as a function of the angle for different magnetic fields (a) and 2D plots of the magnetoresistance as a function of the angle between the magnetic field and the direction of the current in the vdWH from 0º to 360º (b) and viceversa (c) at 200 K. Rotation in the a-b plane.

3.4.13. Device B.7. (CrSBr bilayer).
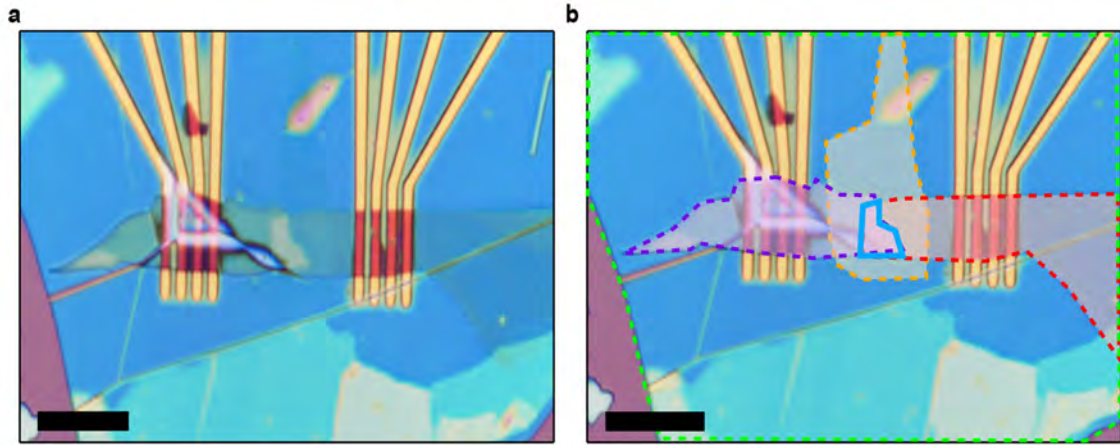
Figure S.138.- Optical picture of the device. For simplicity, the top NbSe$_2$ contact has been highlighted in red, the bottom NbSe$_2$ contact in purple and the CrSBr barrier in orange. h-BN is marked in green. The junction (blue area) is the overlapped area formed by the three different materials. Scale bar: 10 μm.
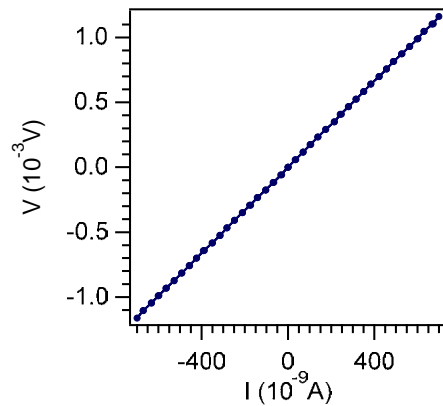
Figure S.139.- DC IV curve for the junction area at 10 K.
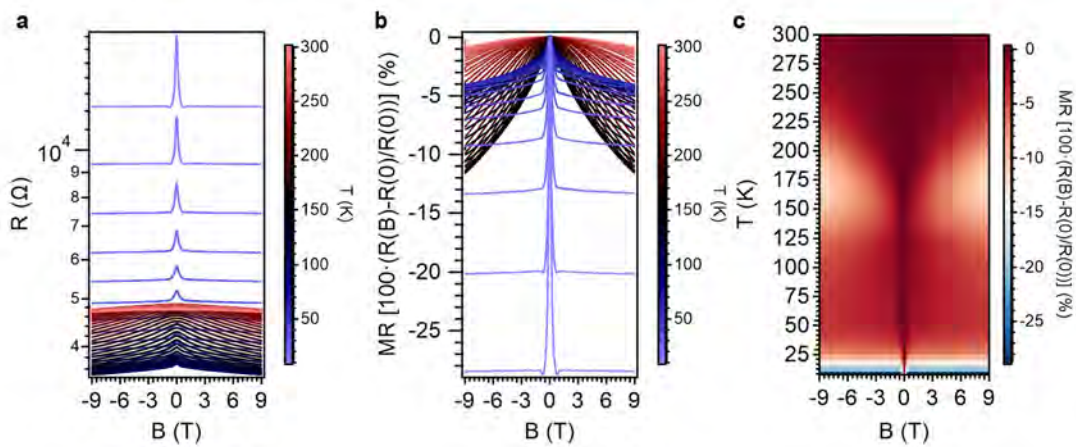
Figure S.140.- a) Resistance as a function of the magnetic field for different temperatures. b) Calculated magnetoresistance as a function of the magnetic field for different temperatures. c) Resistance plot as a function of temperature and magnetic field. Field parallel to the *a* axis.
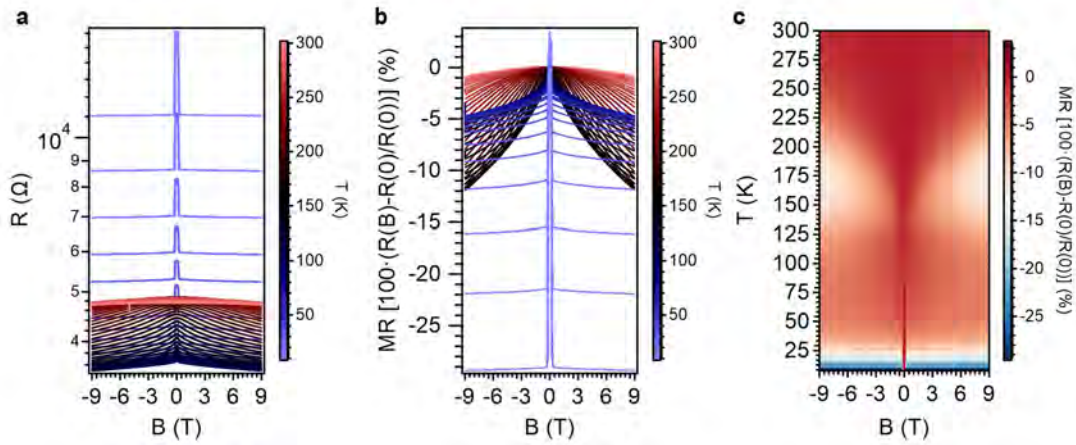
Figure S.141.- a) Resistance (log) as a function of the magnetic field for different temperatures. b) Calculated magnetoresistance as a function of the magnetic field for different temperatures. c) Resistance plot as a function of temperature and magnetic field. Field parallel to the *b* axis.
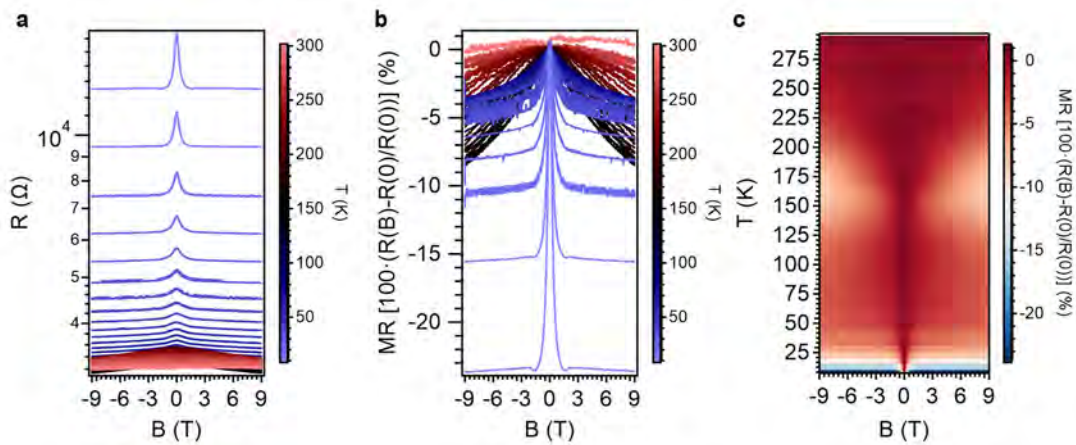
Figure S.142.- a) Resistance (log) as a function of the magnetic field for different temperatures. b) Calculated magnetoresistance as a function of the magnetic field for different temperatures. c) Resistance plot as a function of temperature and magnetic field. Field parallel to the *c* axis.

3.4.14. Device C.1. (CrSBr trilayer).
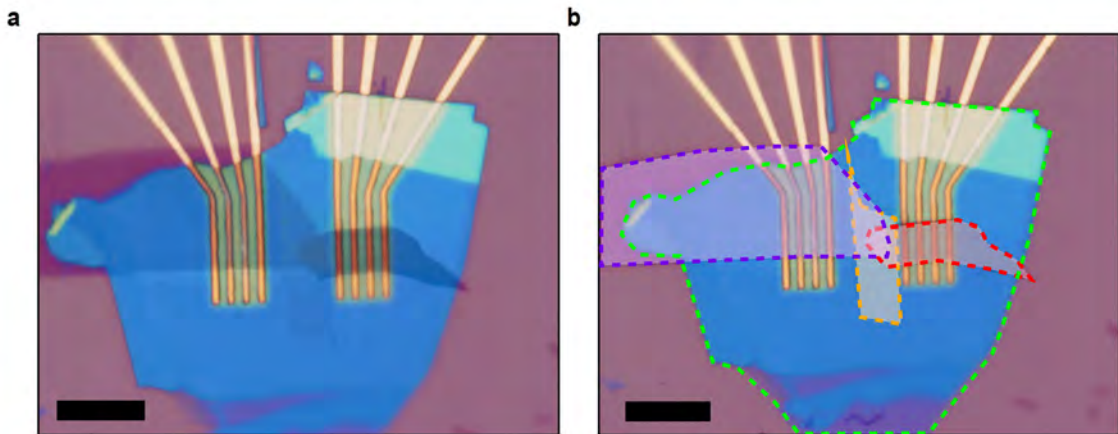
Figure S.143.- Optical picture of the device. For simplicity, the top graphite contact has been highlighted in red, the bottom graphite contact in purple and the CrSBr barrier in orange. h-BN is marked in green. The junction (blue area) is the overlapped area formed by the three different materials. Scale bar: 10 μm.
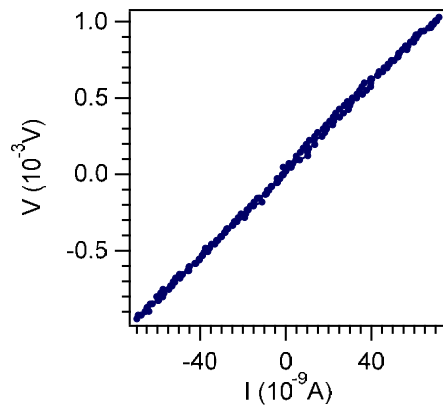
Figure S.144.- DC IV curve for the junction area at 2 K.
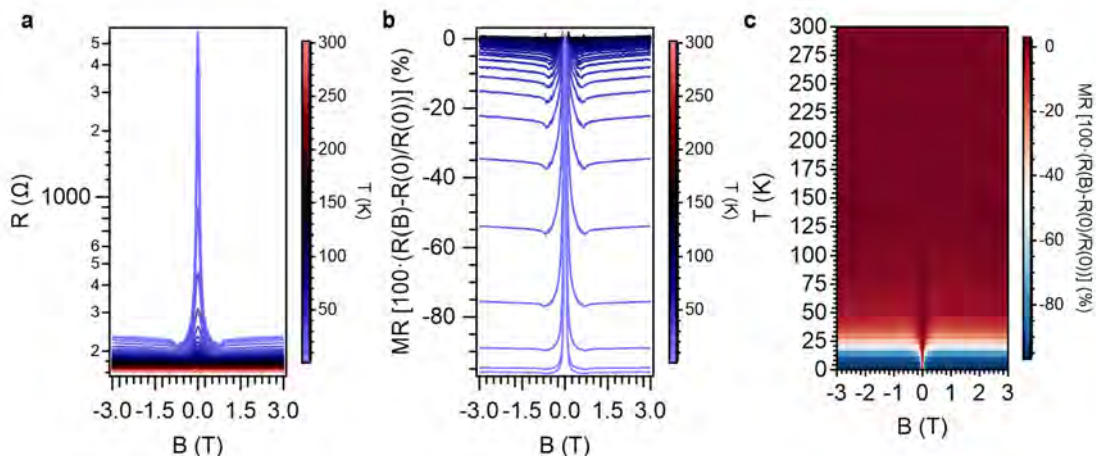
Figure S.145.- a) Resistance (log) as a function of the magnetic field for different temperatures. b) Calculated magnetoresistance as a function of the magnetic field for different temperatures. c) Resistance plot as a function of temperature and magnetic field. Field parallel to the *a* axis.
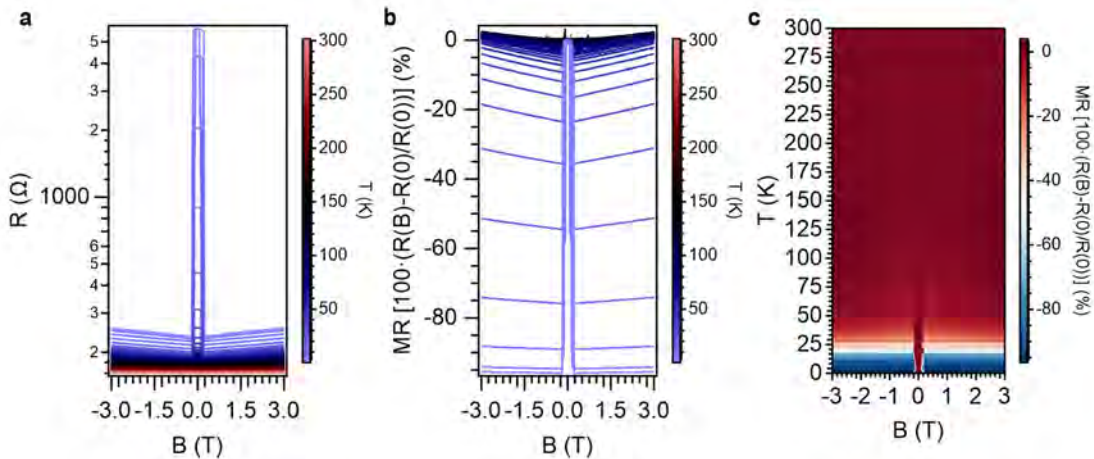
Figure S.146.- a) Resistance as a function of the magnetic field for different temperatures. b) Calculated magnetoresistance as a function of the magnetic field for different temperatures. c) Resistance plot as a function of temperature and magnetic field. Field parallel to the *b* axis.
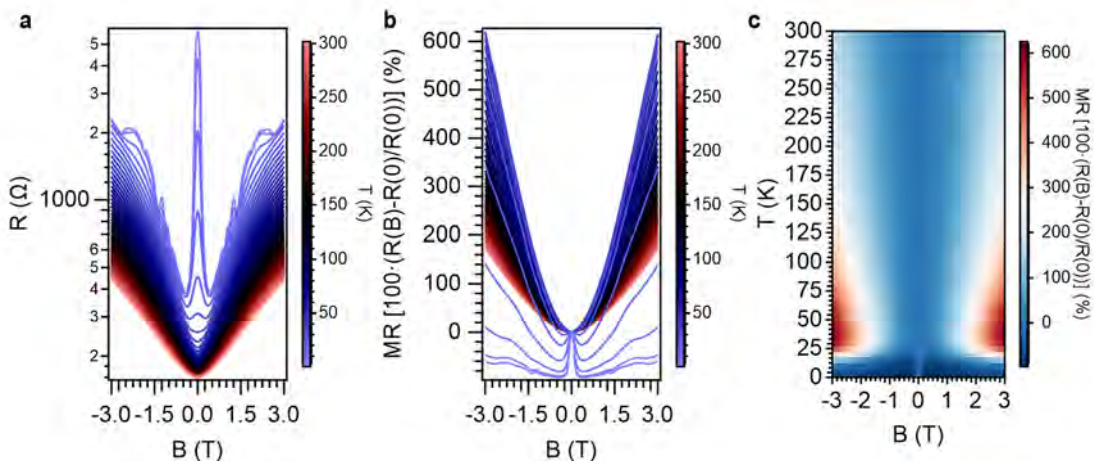
Figure S.147.- a) Resistance as a function of the magnetic field for different temperatures. b) Calculated magnetoresistance as a function of the magnetic field for different temperatures. c) Resistance plot as a function of temperature and magnetic field. Field parallel to the *c* axis.
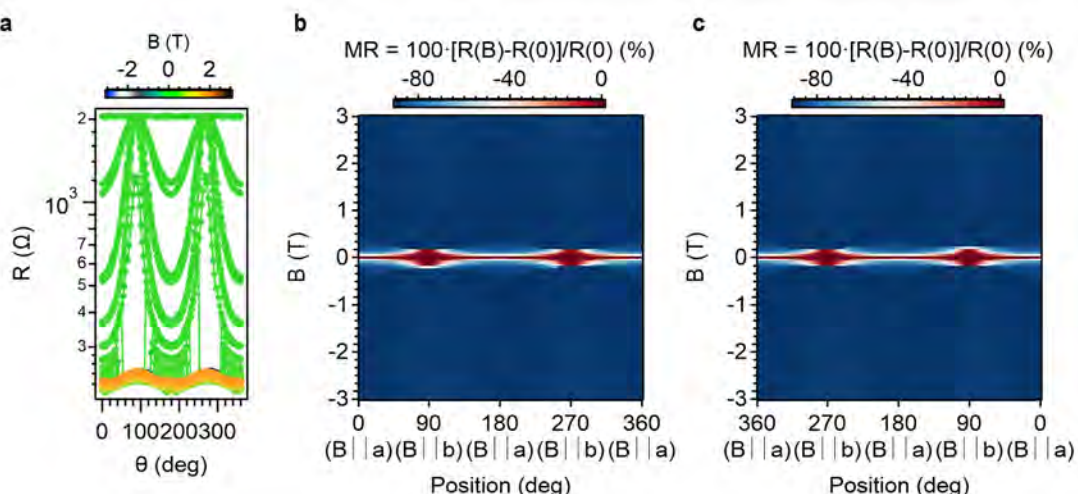
Figure S.148.- Resistance dependence (log) as a function of the angle for different magnetic fields (a) and 2D plots of the magnetoresistance as a function of the angle between the magnetic field and the direction of the current in the vdWH from 0º to 360º (b) and viceversa (c) at 10 K. Rotation in the *a-b* plane.
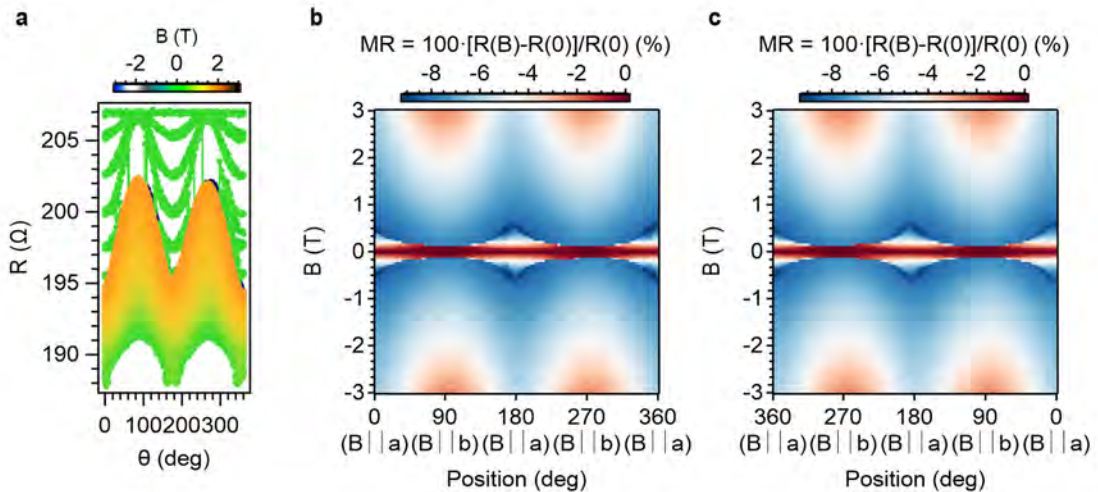
**Figure S.149.-** Resistance dependence (log) as a function of the angle for different magnetic fields (a) and 2D plots of the magnetoresistance as a function of the angle between the magnetic field and the direction of the current in the vdWH from 0º to 360º (b) and viceversa (c) at 50 K. Rotation in the *a-b* plane.
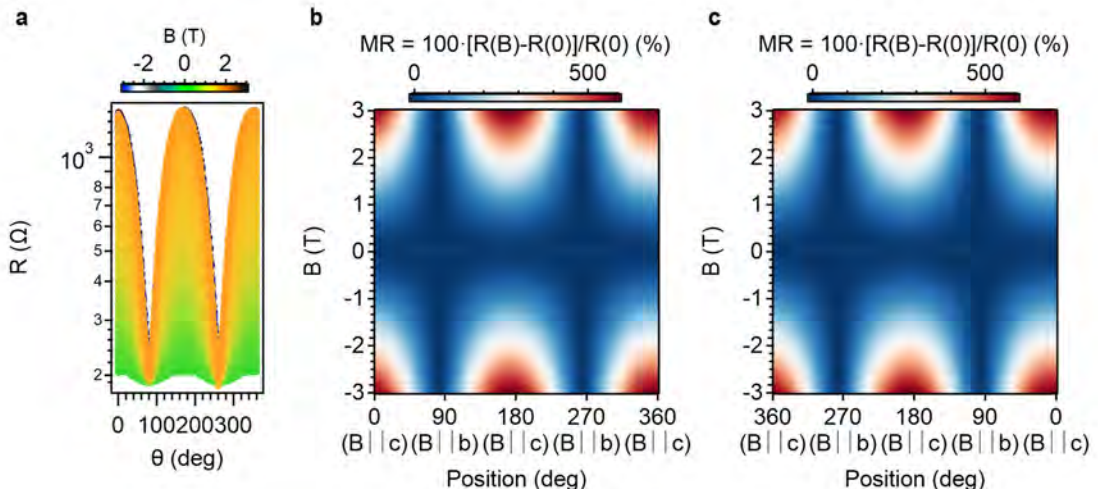
Figure S.150.- Resistance dependence (log) as a function of the angle for different magnetic fields (a) and 2D plots of the magnetoresistance as a function of the angle between the magnetic field and the direction of the current in the vdWH from 0º to 360º (b) and viceversa (c) at 10 K. Rotation in the *c-b* plane.
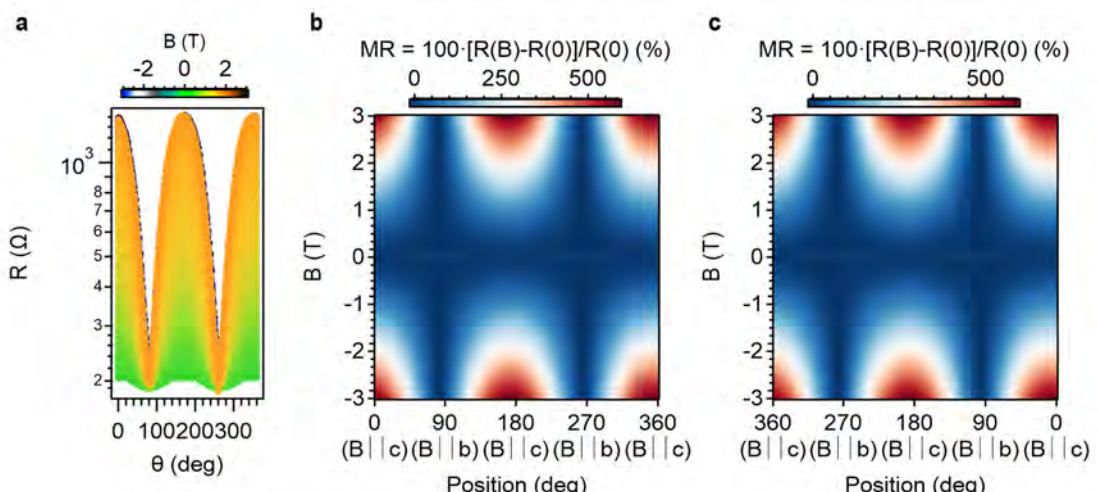
Figure S.151.- Resistance dependence (log) as a function of the angle for different magnetic fields (a) and 2D plots of the magnetoresistance as a function of the angle between the magnetic field and the direction of the current in the vdWH from 0º to 360º (b) and viceversa (c) at 50 K. Rotation in the *c-b* plane.

3.5. Transport mechanism.

In this section, different transport mechanisms are considered, as an energy-activated Arrenhius law or other transport mechanism as variable range hopping or nearest-neighbor hopping. The conductance takes the form:[17]

$$G = G_0 \exp\left(-\frac{T_0}{T}\right)^x$$

being G_0 the residual conductance, T_0 the characteristic hopping temperature and x the hopping exponent. G_0 can be temperature independent or of the form $G_0 = AT^{-m}$, where A is a constant and m varies from 0.8 to 1 (we did not find significant changes by varying m from 0.8 to 1 and we show the results for m = 1).[17,18] The exponent x determines the scaling behavior. We consider the cases of x = 1/2 (Efros-Shklovskii VRH), x = 1/3 (2D-VRH), x = 1/4 (3D-VRH) and x = 1 (nearest-neighbor-hopping, NNH). We note that, formally, the analysis with x = 1 takes the same expression as the Arrhenius analysis.

In all models, a clear tendency change in the slopes can be observed at *ca.* 150 K, when the CrSBr orders magnetically and at low-temperatures, at *ca.* 40 K, attributed to the spin-freezing.[10,14]
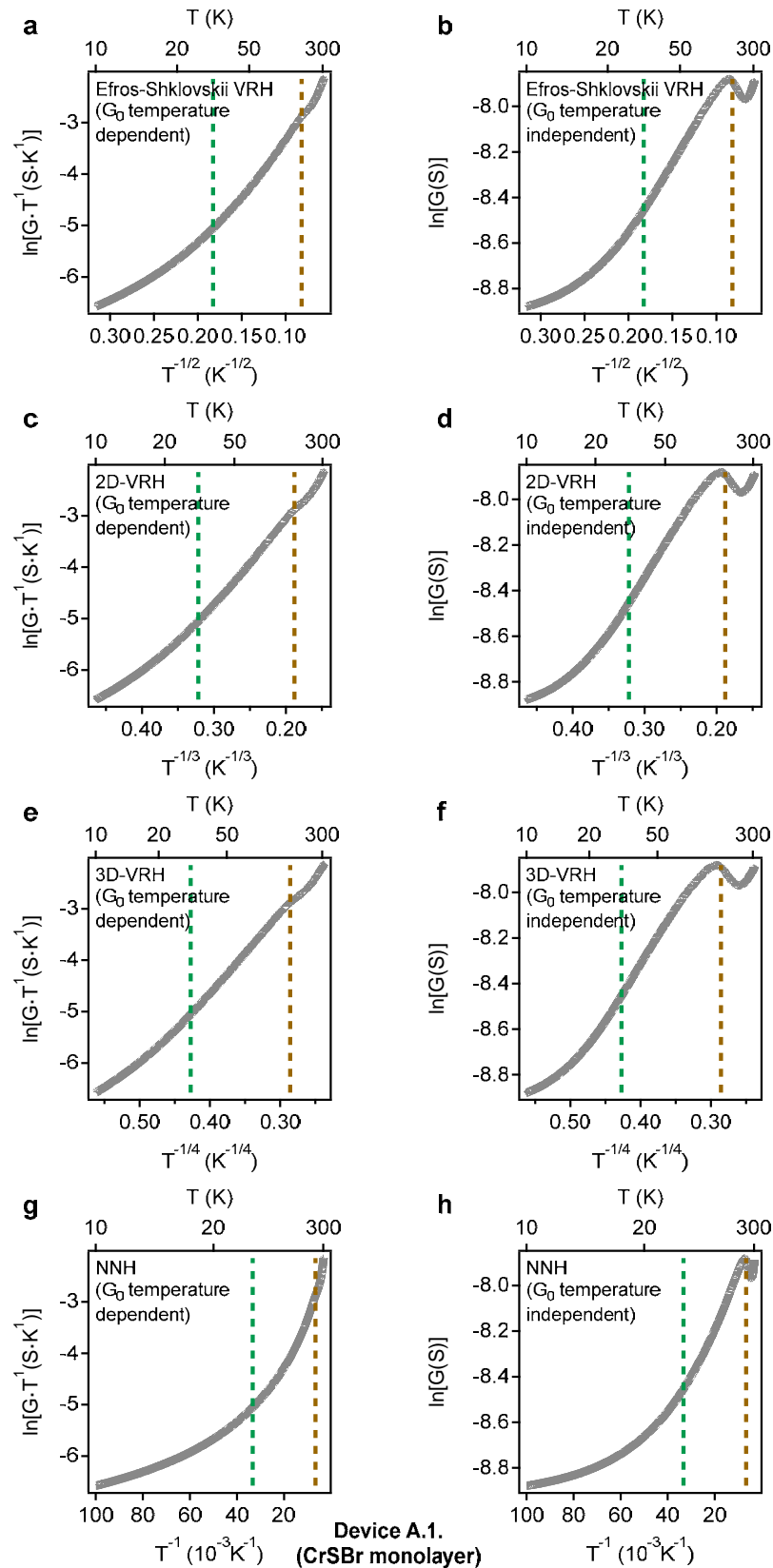
Figure S.152.- Transport mechanisms considered for the device A.1. while sweeping the temperature from 10 K to 300 K. (a-b) Efros-Shklovskii, (c-d) 2D-VRH, (e-f) 3D-VRH and (g-h) NNH.
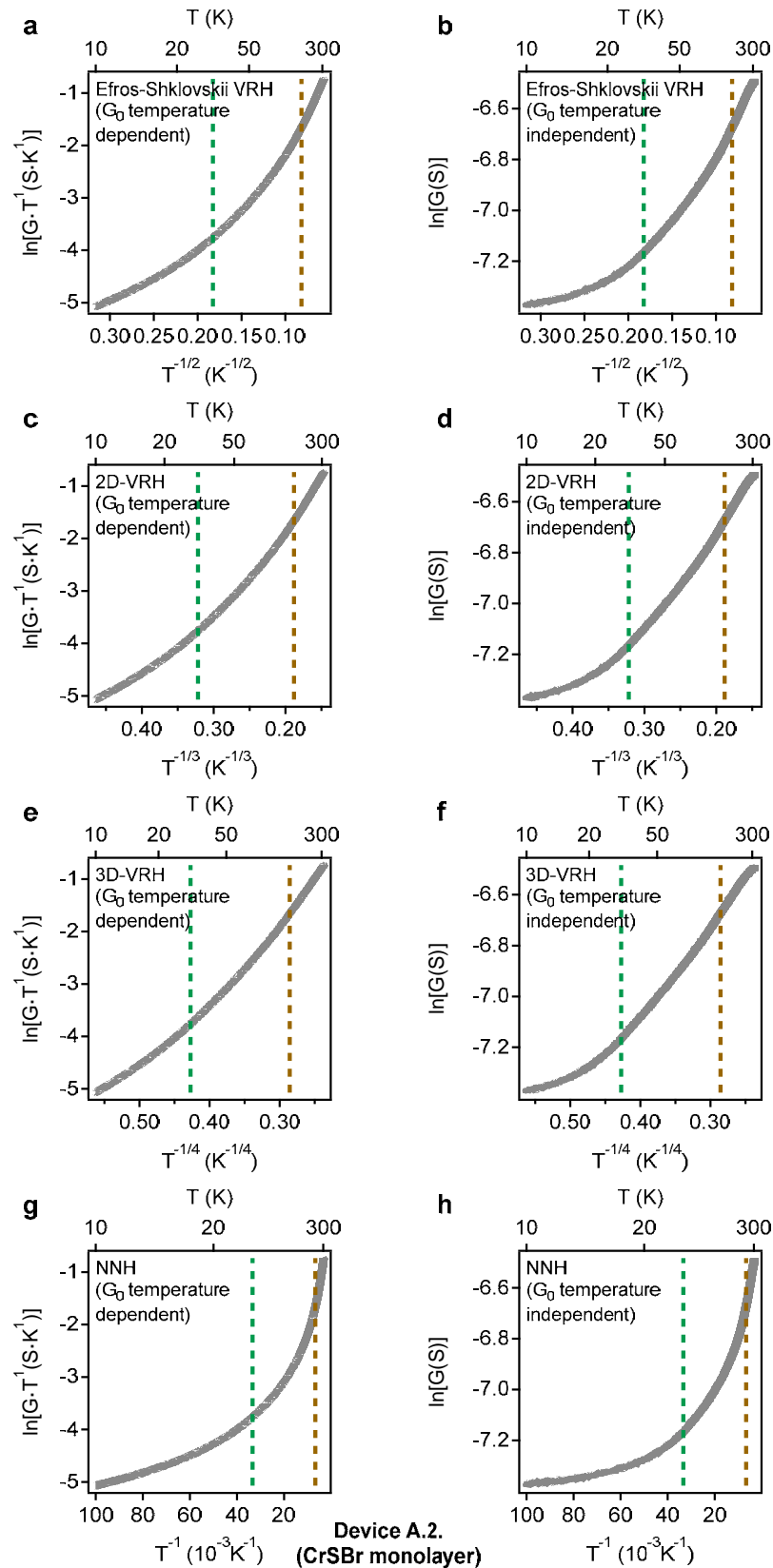
Figure S.153.- Transport mechanisms considered for the device A.2. while sweeping the temperature from 10 K to 300 K. (a-b) Efros-Shklovskii, (c-d) 2D-VRH, (e-f) 3D-VRH and (g-h) NNH.
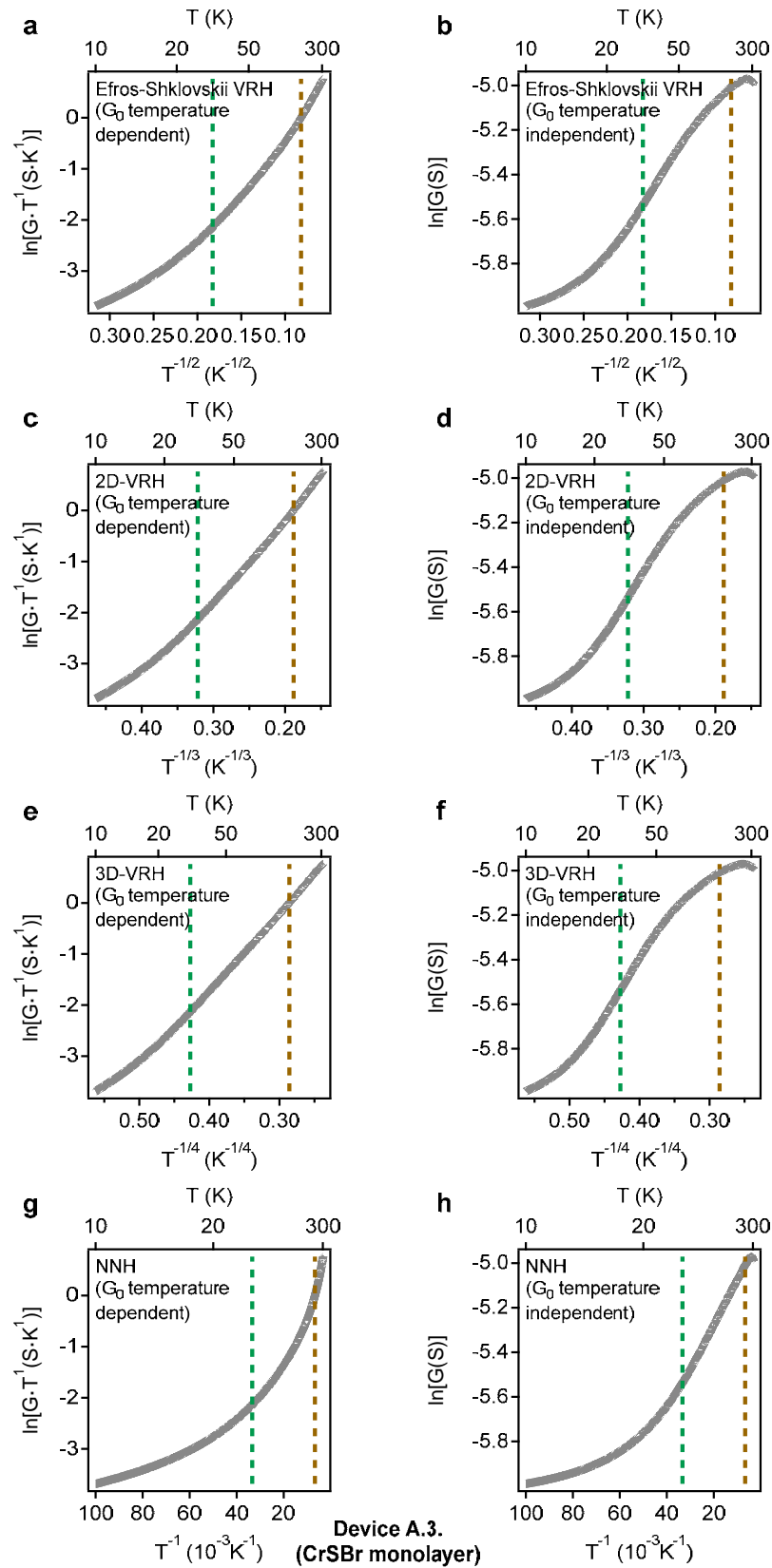
Figure S.154.- Transport mechanisms considered for the device A.3. while sweeping the temperature from 10 K to 300 K. (a-b) Efros-Shklovskii, (c-d) 2D-VRH, (e-f) 3D-VRH and (g-h) NNH.
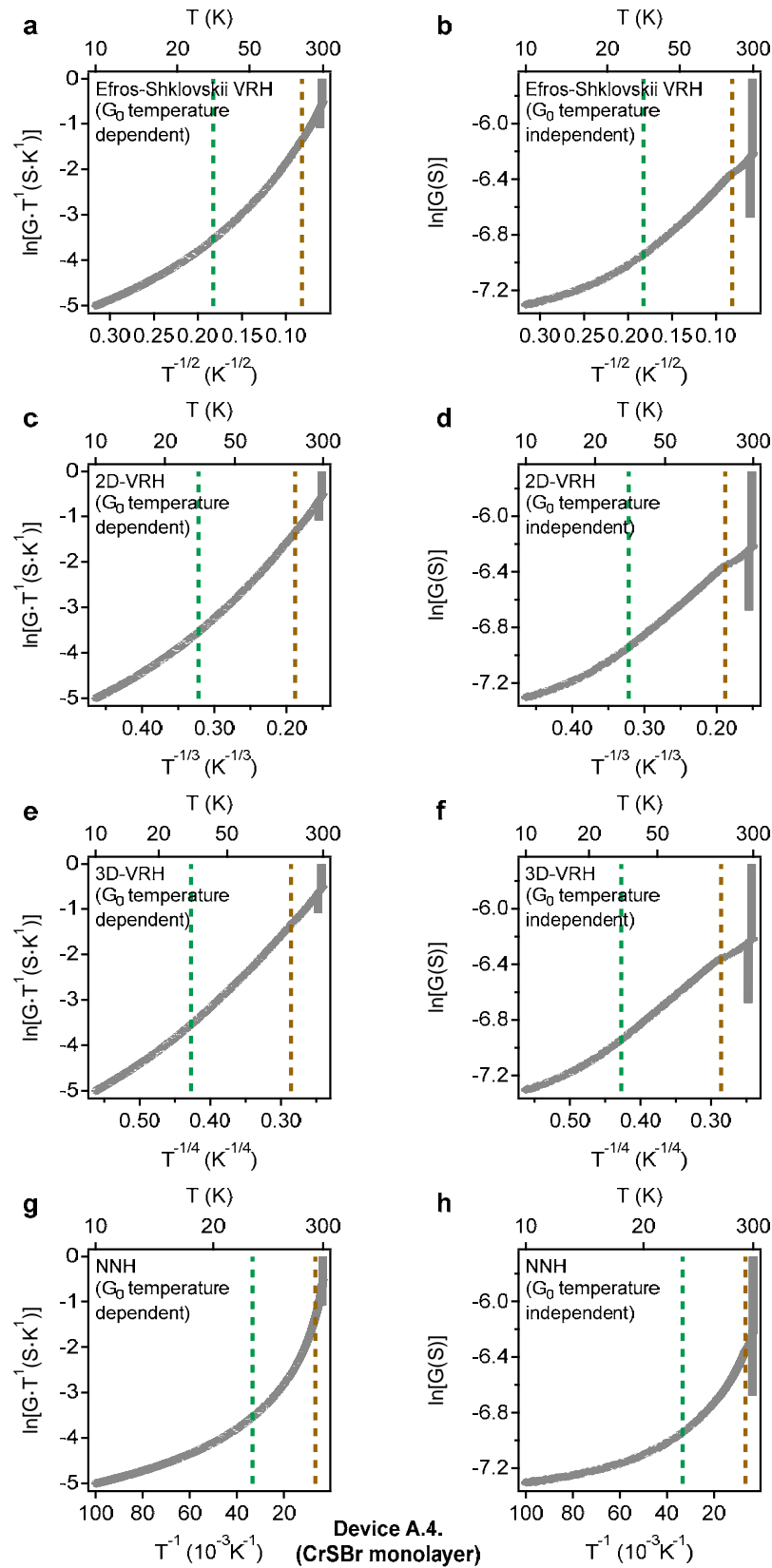
Figure S.155.- Transport mechanisms considered for the device A.4. while sweeping the temperature from 10 K to 300 K. (a-b) Efros-Shklovskii, (c-d) 2D-VRH, (e-f) 3D-VRH and (g-h) NNH.
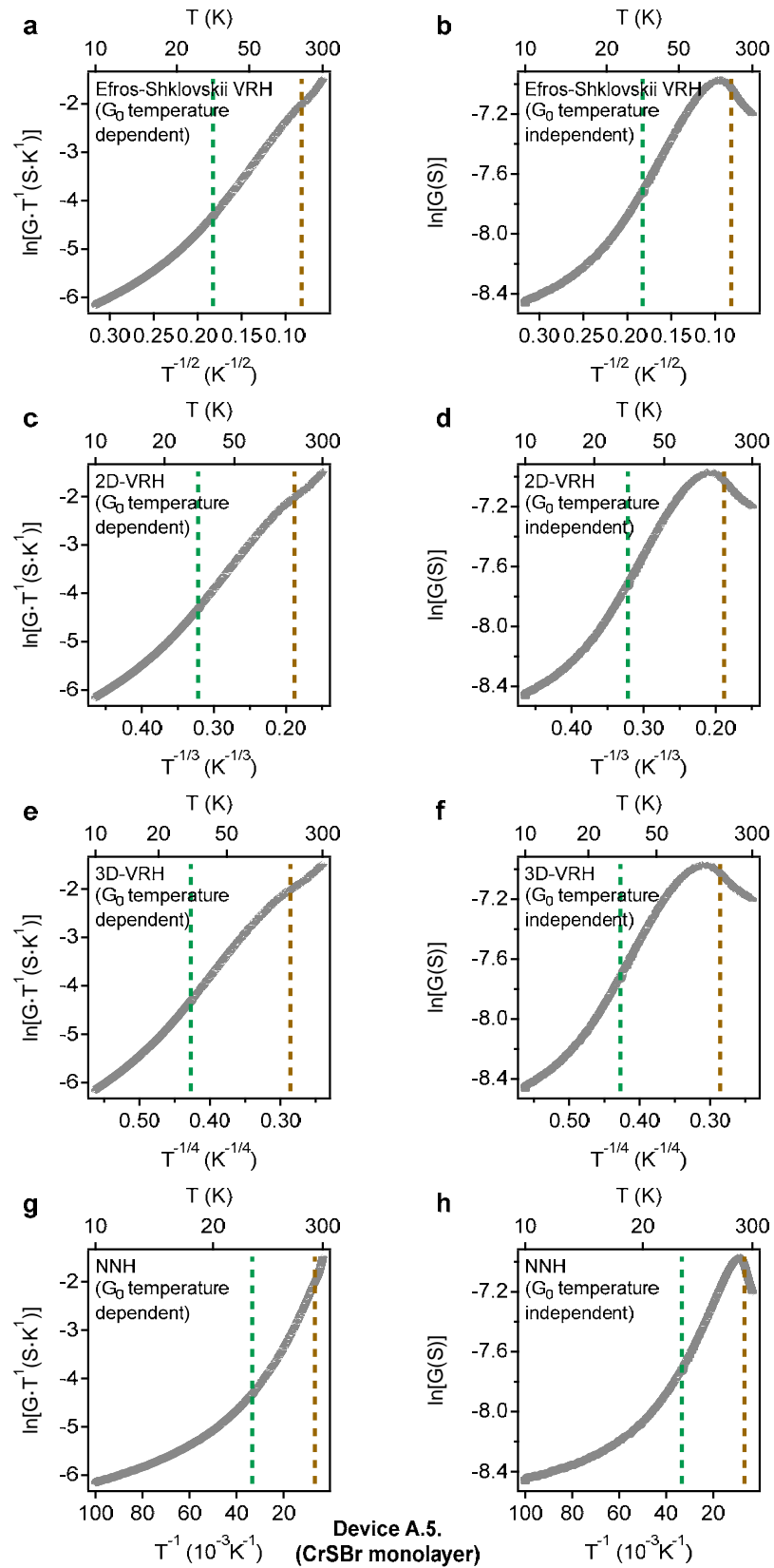
Figure S.156.- Transport mechanisms considered for the device A.5. while sweeping the temperature from 10 K to 300 K. (a-b) Efros-Shklovskii, (c-d) 2D-VRH, (e-f) 3D-VRH and (g-h) NNH.
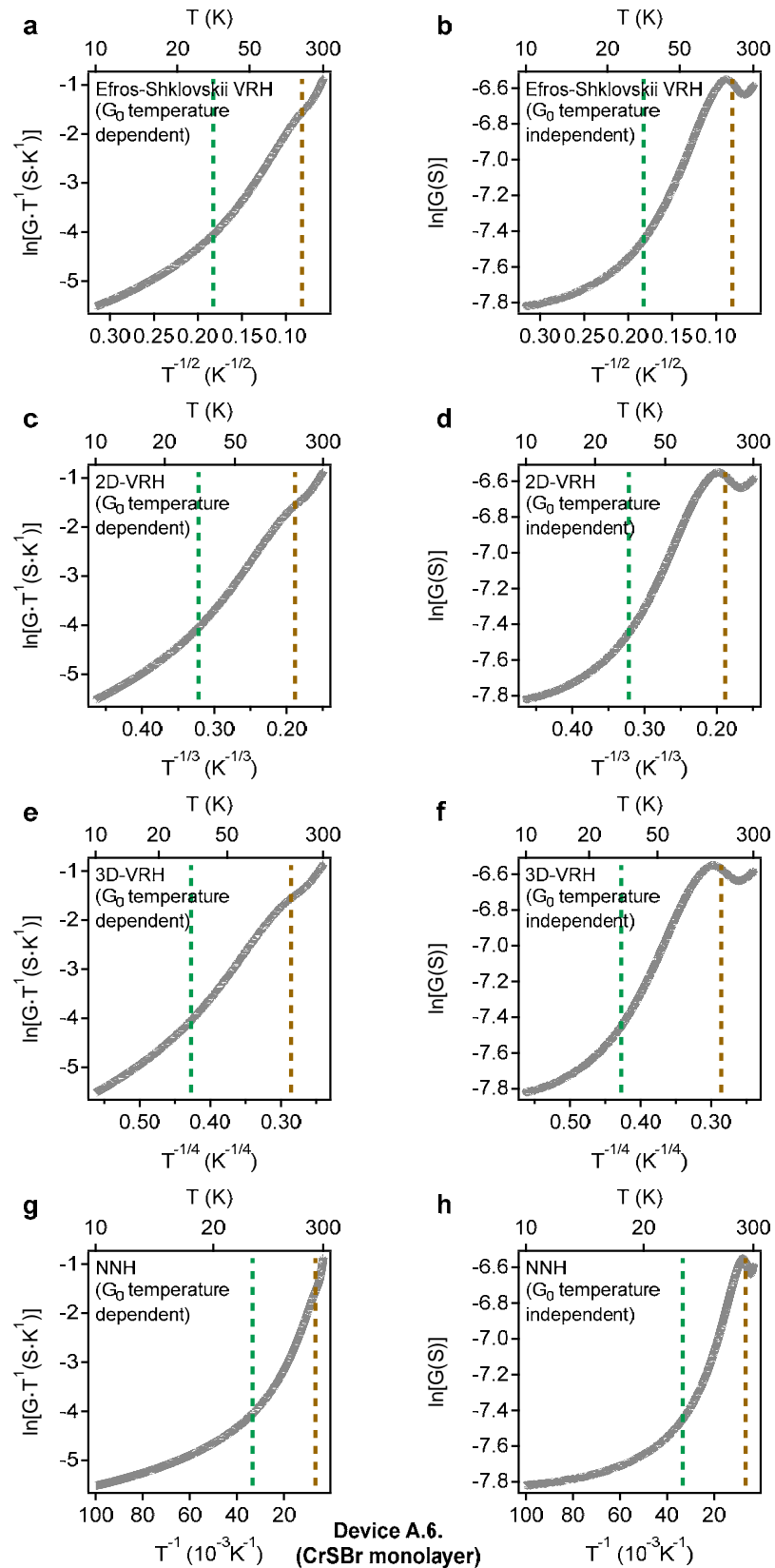
Figure S.157.- Transport mechanisms considered for the device A.6. while sweeping the temperature from 10 K to 300 K. (a-b) Efros-Shklovskii, (c-d) 2D-VRH, (e-f) 3D-VRH and (g-h) NNH.
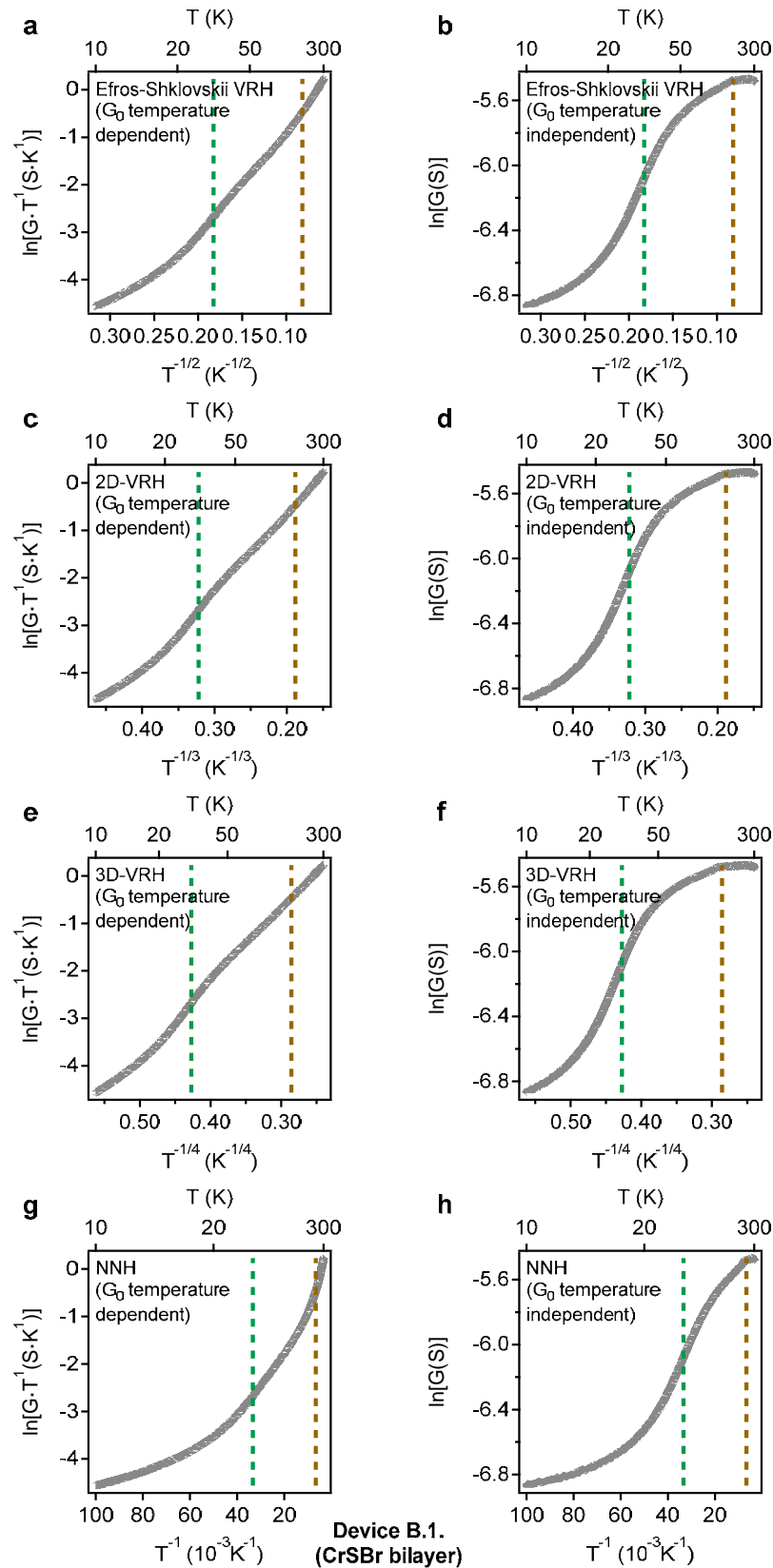
Figure S.158.- Transport mechanisms considered for the device B.1. while sweeping the temperature from 10 K to 300 K. (a-b) Efros-Shklovskii, (c-d) 2D-VRH, (e-f) 3D-VRH and (g-h) NNH.
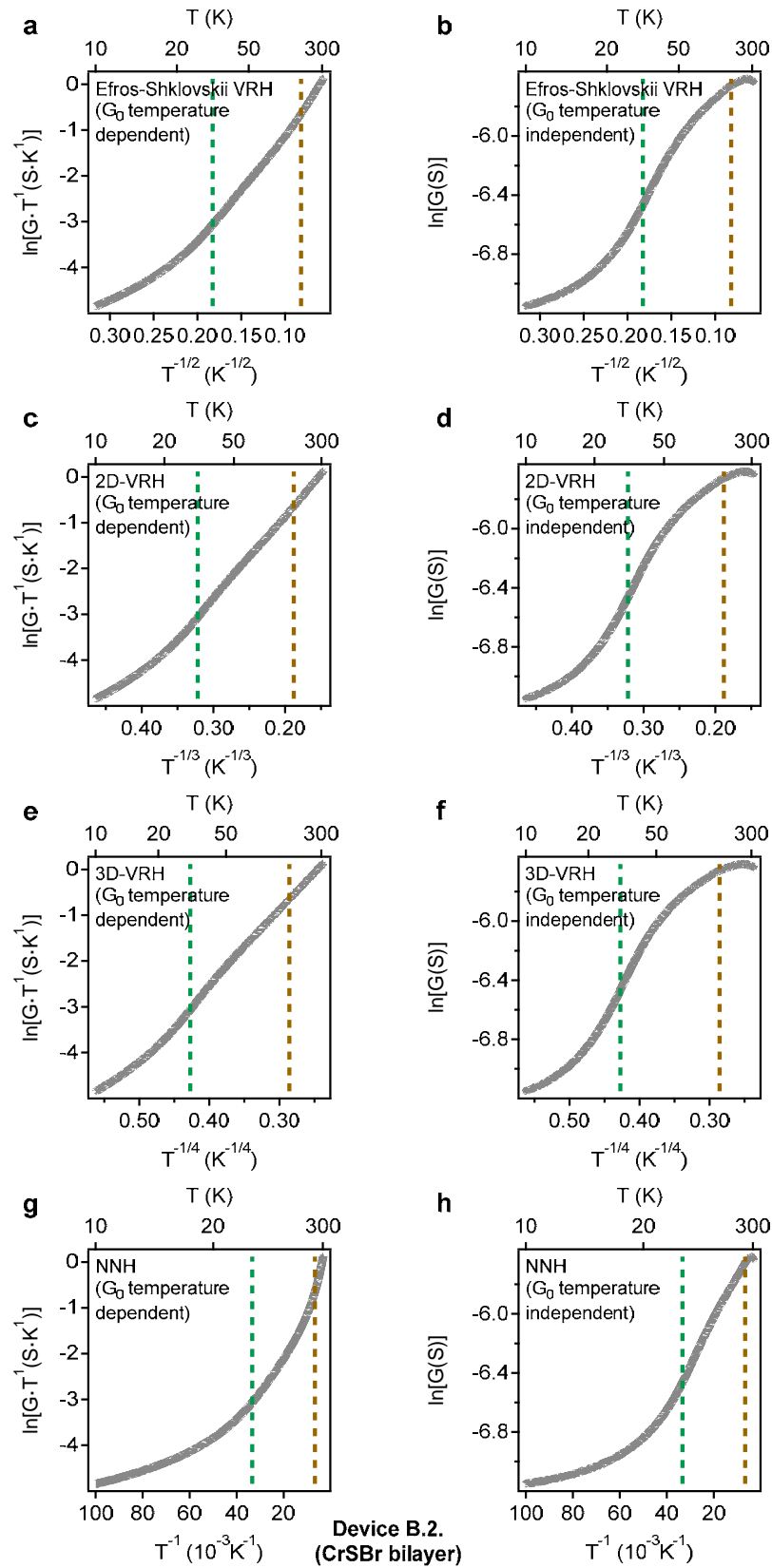
Figure S.159.- Transport mechanisms considered for the device B.2. while sweeping the temperature from 10 K to 300 K. (a-b) Efros-Shklovskii, (c-d) 2D-VRH, (e-f) 3D-VRH and (g-h) NNH.
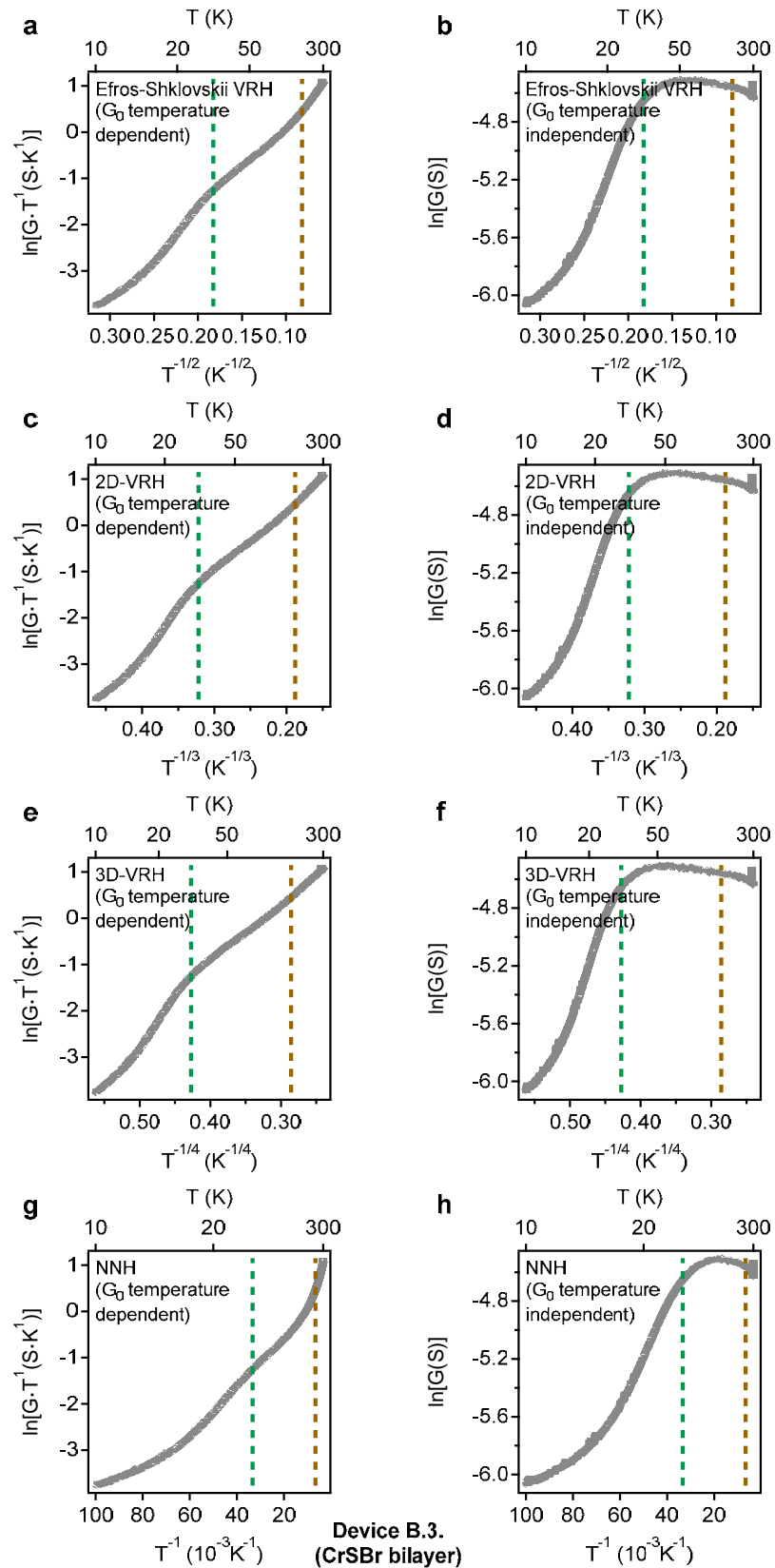
Figure S.160.- Transport mechanisms considered for the device B.3. while sweeping the temperature from 10 K to 300 K. (a-b) Efros-Shklovskii, (c-d) 2D-VRH, (e-f) 3D-VRH and (g-h) NNH.
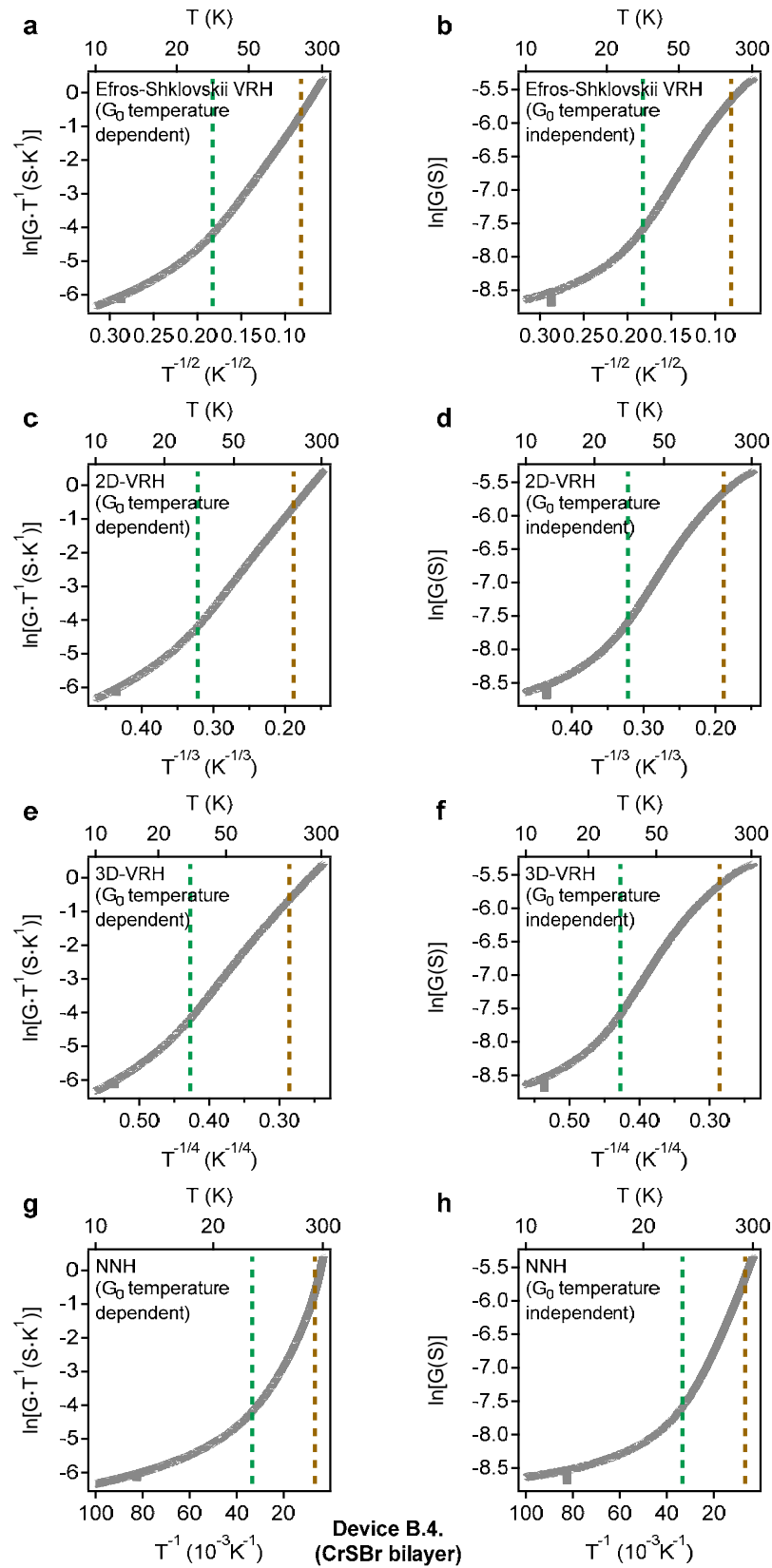
Figure S.161.- Transport mechanisms considered for the device B.4. while sweeping the temperature from 10 K to 300 K. (a-b) Efros-Shklovskii, (c-d) 2D-VRH, (e-f) 3D-VRH and (g-h) NNH.
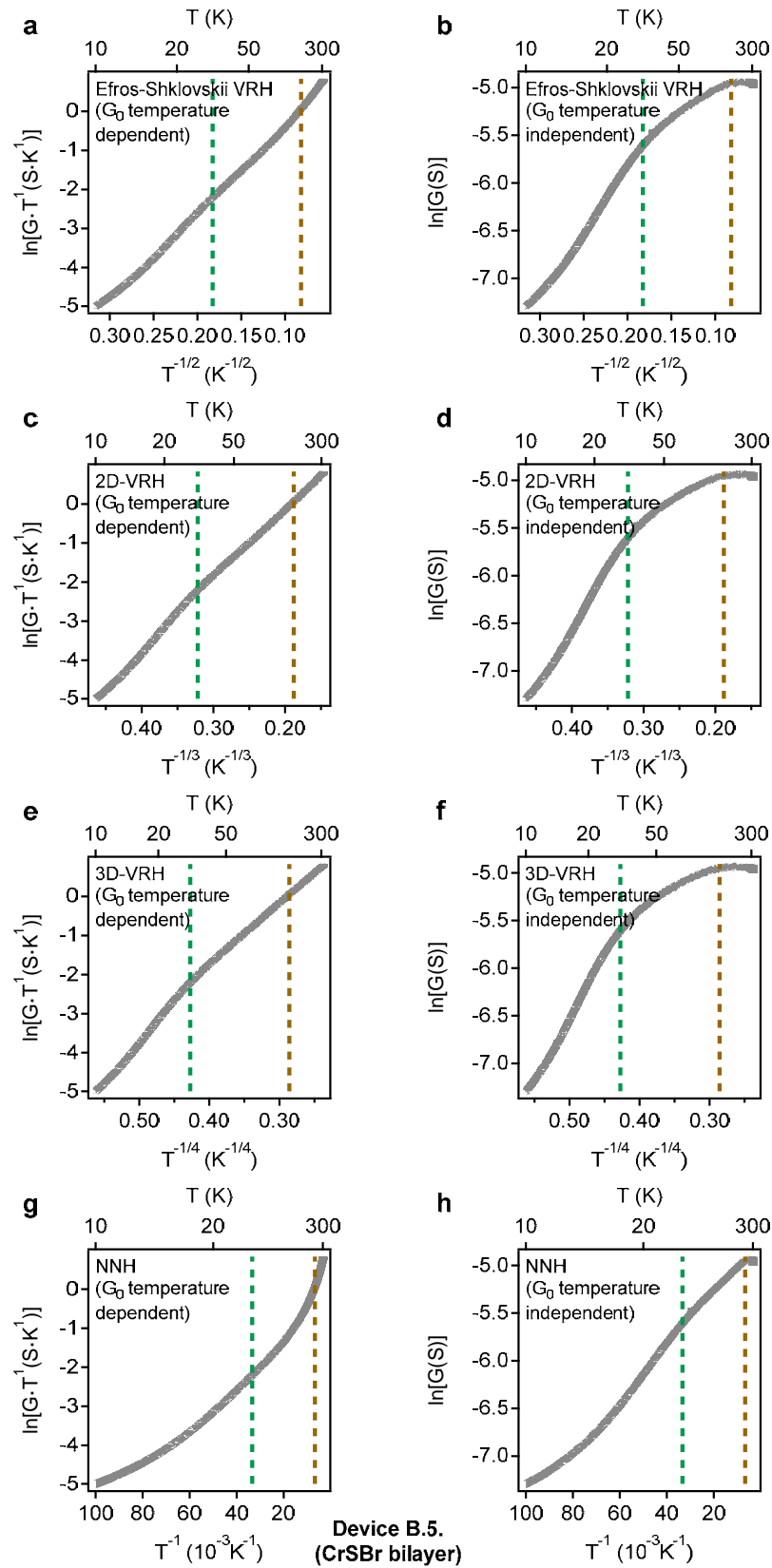
Figure S.162.- Transport mechanisms considered for the device B.5. while sweeping the temperature from 10 K to 300 K. (a-b) Efros-Shklovskii, (c-d) 2D-VRH, (e-f) 3D-VRH and (g-h) NNH.
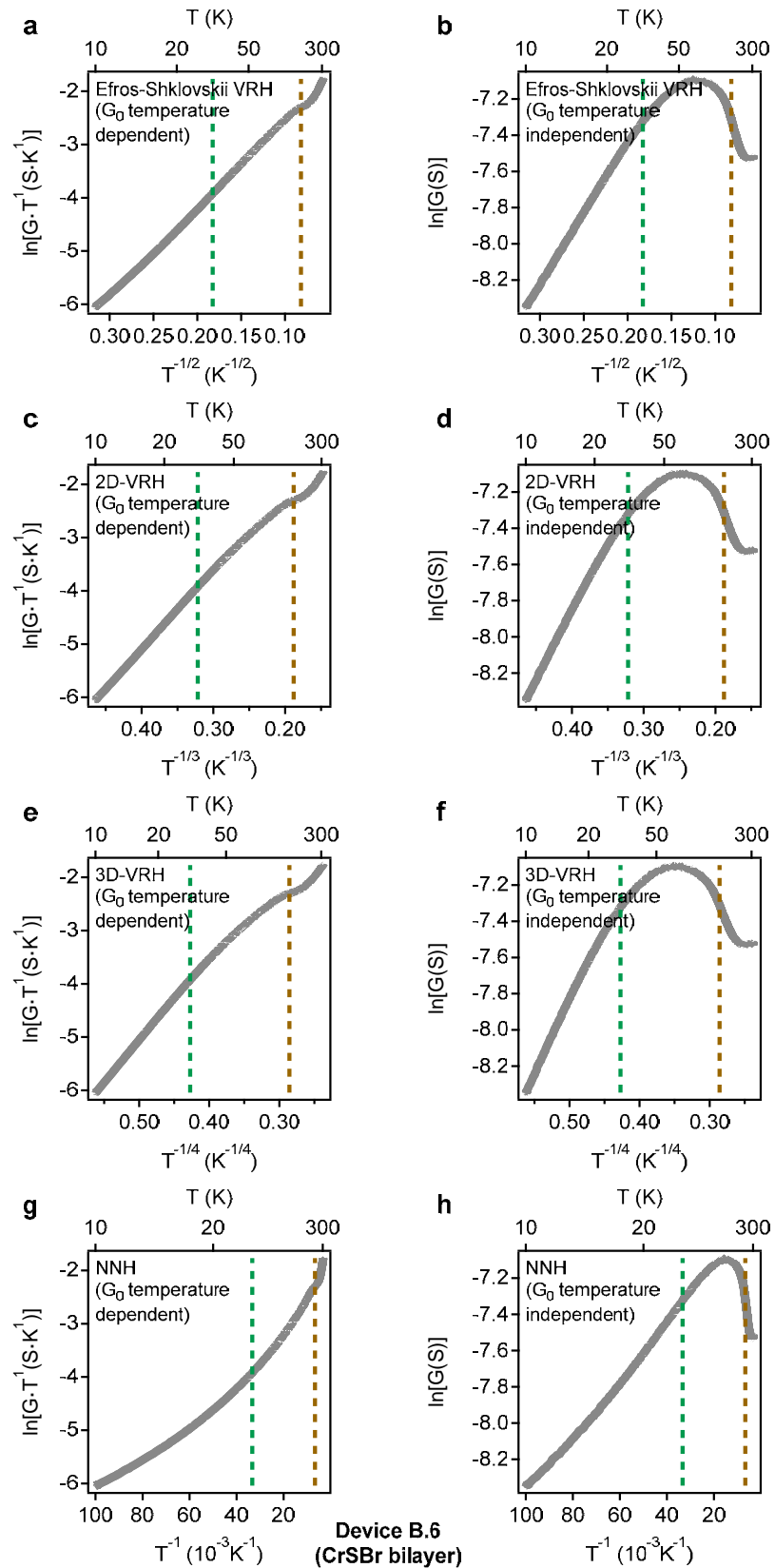
Figure S.163.- Transport mechanisms considered for the device B.6. while sweeping the temperature from 10 K to 300 K. (a-b) Efros-Shklovskii, (c-d) 2D-VRH, (e-f) 3D-VRH and (g-h) NNH.
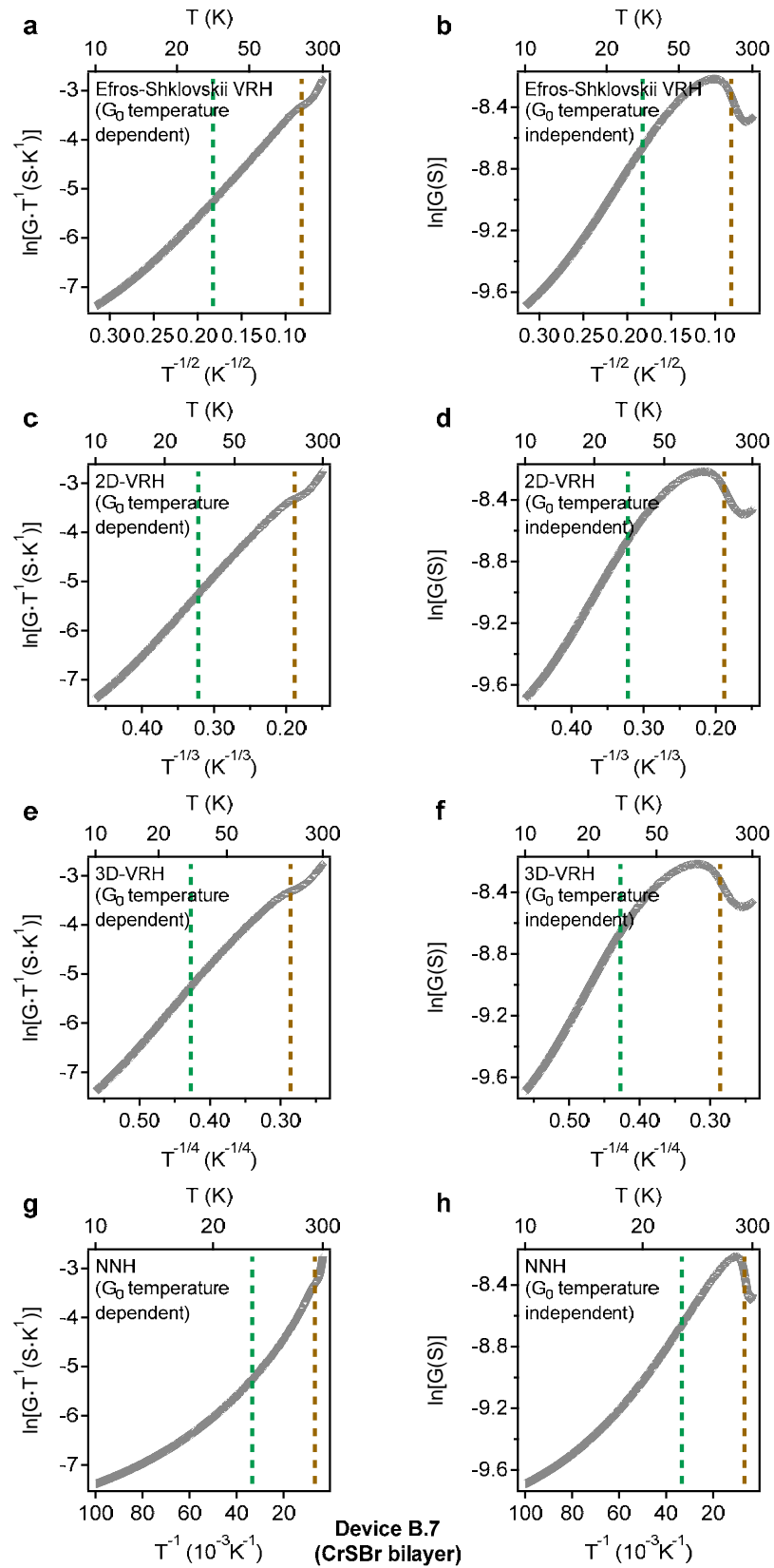
Figure S.164.- Transport mechanisms considered for the device B.7. while sweeping the temperature from 10 K to 300 K. (a-b) Efros-Shklovskii, (c-d) 2D-VRH, (e-f) 3D-VRH and (g-h) NNH.
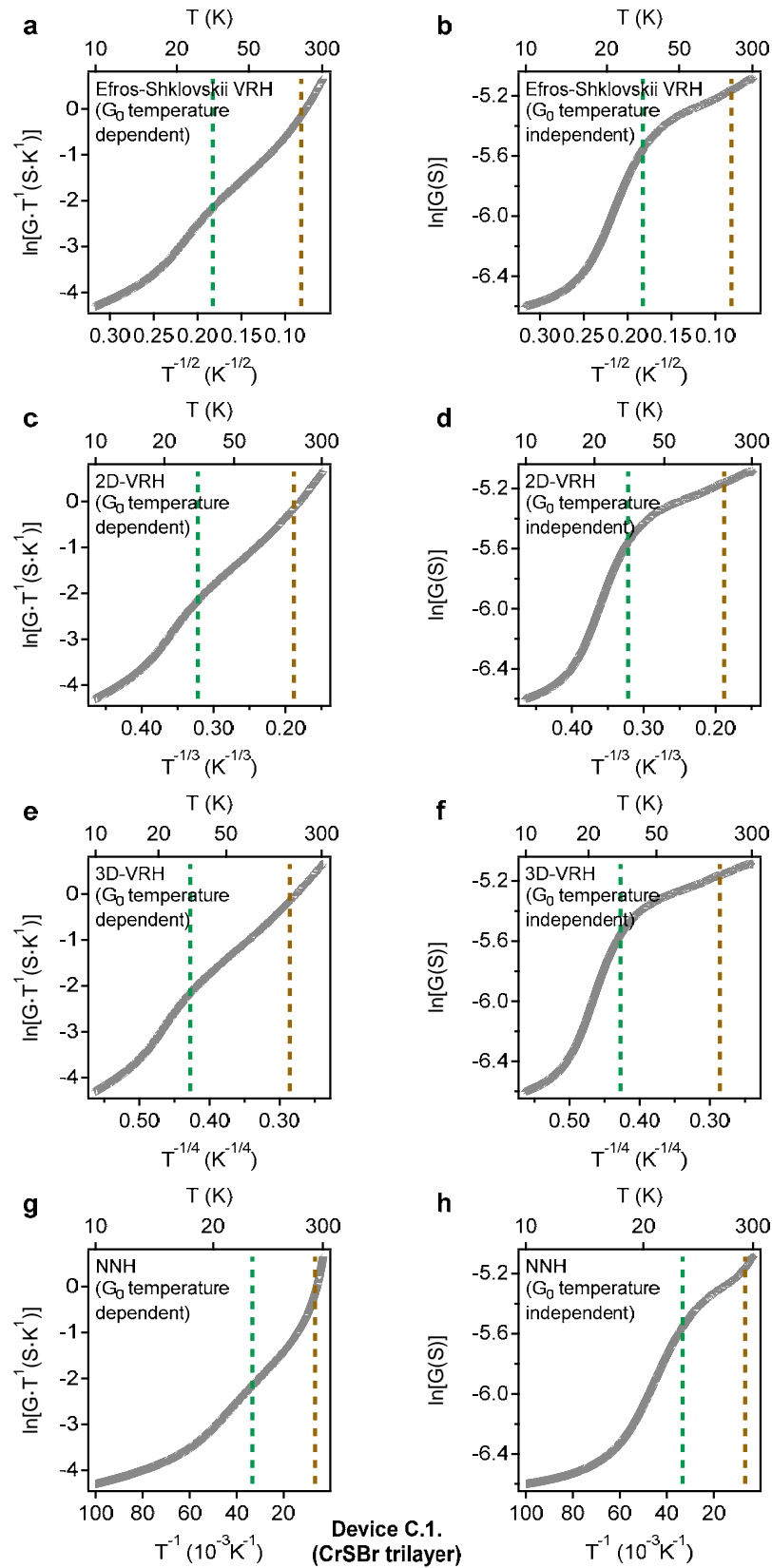
Figure S.165.- Transport mechanisms considered for the device C.1. while sweeping the temperature from 10 K to 300 K. (a-b) Efros-Shklovskii, (c-d) 2D-VRH, (e-f) 3D-VRH and (g-h) NNH.

4.- Theoretical calculations.

To compute isotropic exchange parameters, we performed DFT+U calculations including spin-orbit coupling (SOC) by using fully-relativistic pseudopotentials. We constructed a tight-binding Hamiltonian expressed in the highly localized basis of Wannier functions, as represented in Eq .1:

$$|\mathbf{R}n\rangle = \frac{V}{(2\pi)^3} \int_{BZ} d\mathbf{k} e^{-i\mathbf{k}\cdot\mathbf{R}} \sum_{m=1}^{J} U_{mn}^{(\mathbf{k})} |\psi_{m\mathbf{k}}\rangle \tag{1}$$

The results were mapped to the exchange Hamiltonian as specified in Eq. 2 using Green's functions method as implemented in the TB2J package.[19]

$$\hat{H} = -\sum_{<ij>} \hat{\vec{S_i}} \cdot J_1 \cdot \hat{\vec{S_j}} - \sum_{<<ij>>} \hat{\vec{S_i}} \cdot J_2 \cdot \hat{\vec{S_j}} - \sum_{<<<ij>>>} \hat{\vec{S_i}} \cdot J_3 \cdot \hat{\vec{S_j}} \tag{2}$$

where J_i is an isotropic exchange parameter for first (J_1), second (J_2) and third (J_3) nearest-neighbors. Then, we calculated the evolution of J-values with temperature for three values of Hubbard U (3 eV, 5 eV in **Figure S.167** and 4 eV in the main text **Figure 4c**). We found the ratio J_1/J_3 for U=4 eV (1.07) closer to the fitted values of the exchange Hamiltonian from inelastic neutron scattering measurements (1.14) by Sheie *et al.*[20]

The anisotropy arises from spin orbit coupling term and crystal field. In a recent work about the 2D CrSBr, the importance of considering effect of magnetic dipole-dipole interaction on anisotropy has been proved.[21] We calculate the shape anisotropy, which arises from dipole-dipole interactions following the classical approach:

$$E = \frac{\mu_0}{8\pi} \sum_{i \neq j} \frac{1}{|\vec{r_{ij}}|^3} \left(\vec{m_i} \cdot \vec{m_j} - \frac{3(\vec{m_i} \cdot \vec{r_{ij}})(\vec{m_j} \cdot \vec{r_{ij}})}{|\vec{r_{ij}}|^2} \right) \tag{4}$$

where r_{ij} is a vector between two magnetic atoms, m_i - magnetic moment of Cr atom, arising from its spin.

SOC, shape and total anisotropy with respect to the energy of the monolayer with spins aligned along b direction are shown in **Table S.4** for the structure corresponding to T = 10 K. We estimate the magnetic field needed to switch the spin directions from the easy-axis direction (b) based on anisotropy energy differences. We find that with magnetic field of magnitude 0.3 T applied along the direction of the a axis, it is possible to switch the direction of magnetization from the easy-axis direction. Moreover, one could direct the magnetization out-of-plane as well by applying magnetic field of magnitude 0.8 T along the c-axis direction. Total anisotropy between a and b directions is governed by the SOC term, while for the case of switching between b and c shape anisotropy is of the same magnitude as the SOC one. It shows the typical behavior of shape anisotropy in 2D systems as it tends to align spins in plane.

In order to calculate SOC anisotropy from the total energy differencies through DFT we need to carefully converge energies with respect to the k-mesh and kinetic energy cut-off up to 30x30x1 and 190 Ry, respectively.

Shape anisotropy originates from dipole-dipole interactions. Hereafter, we calculate the dipole-dipole energy of the monolayer of the size NxNx1, where N is the number of unit cell`s replication along each crystallographic axis (a, b, c) for each spin direction (e_a, e_b, e_c). Dipole-dipole energy per atom (which basically has the same sense as energy per volume, because there is a certain amount of volume corresponds to each atom) for each spin direction (E_a, E_b, E_c) were defined as $E_i = e_i / (2N^2)$ (since each unit cell has two magnetic Cr atoms in it). Difference in dipole-dipole energy between two directions ($E_a - E_b$ or $E_c - E_b$) reachs saturation value with increasing N. Example of the energy difference dependencies over N is shown in **Figure S.166**. We used the N=100 for the calculations.
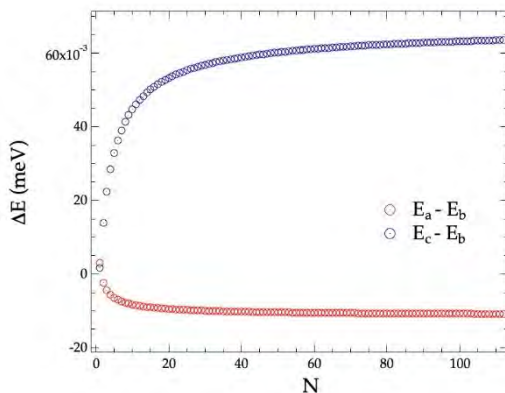
Figure S.166.- Shape energy difference Ea - Eb(red) and Ec - Eb(blue) dependencies on the sample size N.

Next step is to evaluate magnetic field necessary to reorient spin's directions. Hereafter, we are discussing the case with a magnetic field applied in the a direction. One could consider two states of the monolayer system: with spins along b direction (corresponding total anisotropy energy E_b, total anisotropy energy is a sum of SOC anisotropy energy and shape anisotropy energy) and with spins directed along a direction (corresponding total anisotropy energy E_a). In that case energy of the interaction between magnetic field and magnetic moment associated with spin of Cr^{3+} ion will be 0 for E_b state (**B** perpendicular to magnetic moment), while for the E_a state it will be equal to $-3 \mu_B B$ in the presence of **B** (**B** parallel to the magnetic moment). Thus, it will be necessary to apply a magnetic field along the a direction larger than $(E_a - E_b) / 3\mu_B$ in order to compensate the anisotropic energy difference with zeeman energy and to reorient the spins from b to a. The same scheme was applied for estimating the field necessary for reorienting spin's alignment form b to c direction when the field is applied along c. Following this approach we obtained the energy data presented in **Table S.4**.

Table S.4.- Anisotropy energies (meV/Cr atom) for different spin directions with respect to the easy axis, and required field needed (T) to switch spins from the easy to the medium (B_{ba}) and hard (B_{bc}) axis.

	E_a	E_b	E_c	B_{ba}	B_{bc}
SOC	0.065	0	0.072	0.4	0.4
Shape	-0.011	0	0.063	-	0.4
Total	0.054	0	0.135	0.3	0.8

Isotropic exchange results for Hubbard U of 3 eV and 5 eV
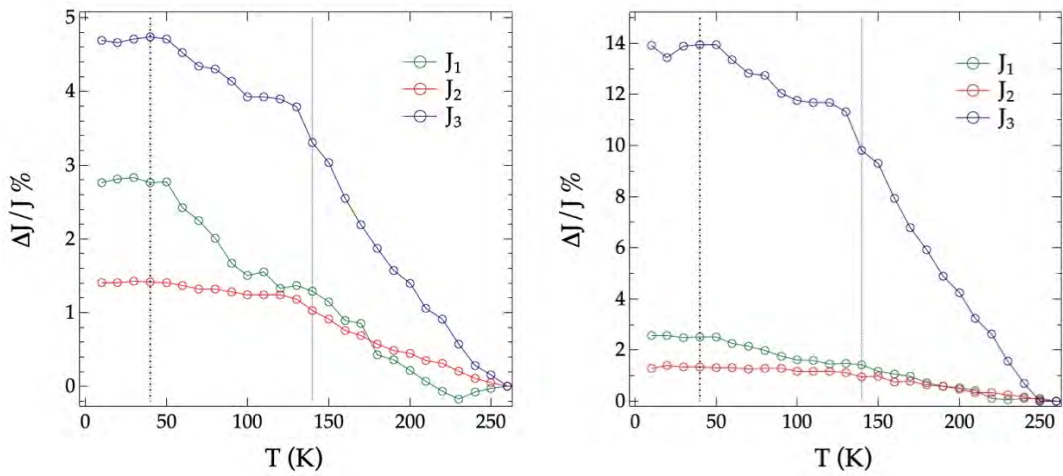
Figure S.167.- Changes in J_1, J_2 and J_3 over temperature for a Hubbard U = 3 eV (left) and U = 5 eV (right).

Structural changes with temperature
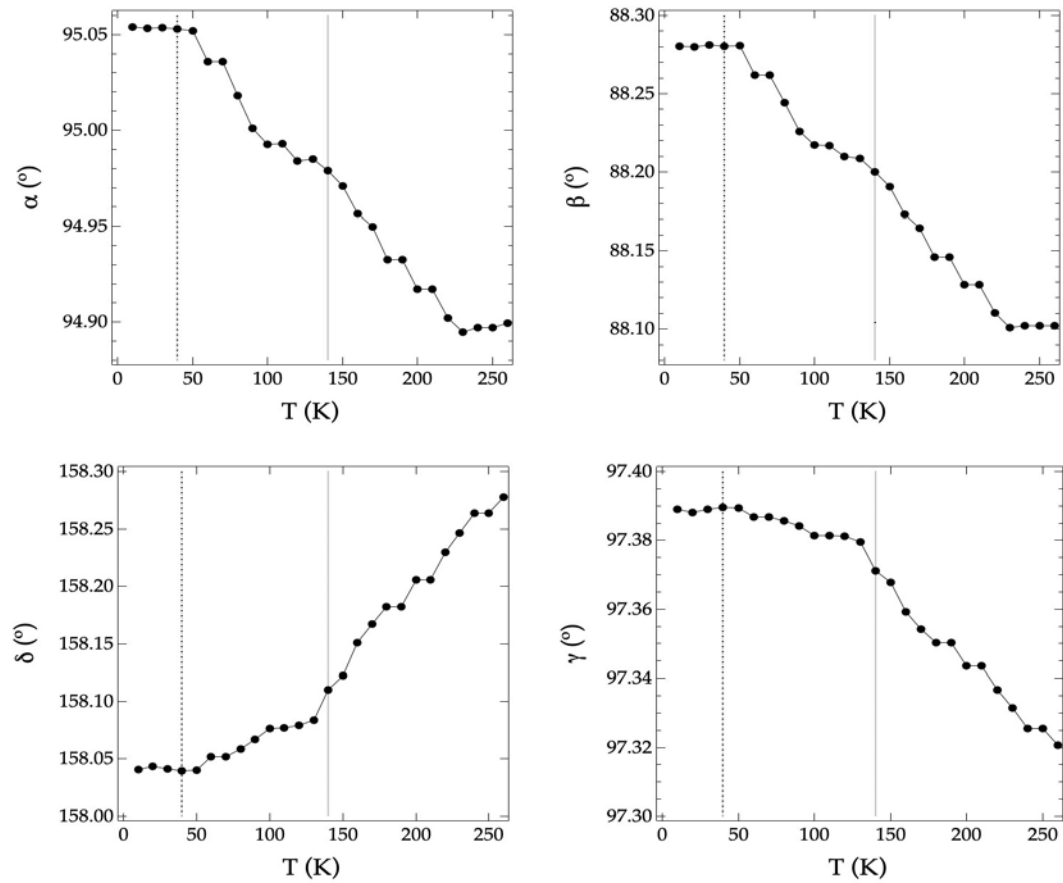
Figure S.168.- Evolution of the angles for different super exchange paths (α, β, γ, δ) in a range of energy from 260 K to 10 K.

Correlation between isotropic J values and corresponding angles
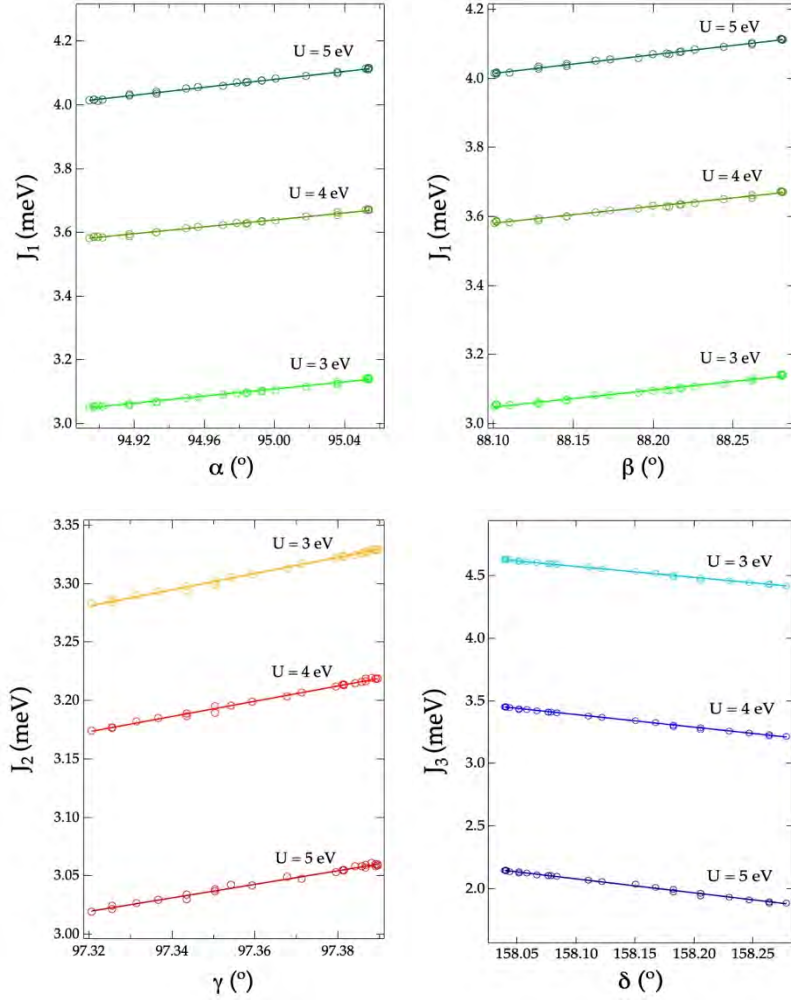
**Figure S.169.** Evolution and linear fit of J_1, J_2 and J_2 for different super exchange path angles (α, β, γ, δ).

Our first-principles results reveal a strong coupling of magnetism and the lattice in single-layer CrSBr, which can be seen as evidence of magnetoelastic coupling since the ordering of magnetic moments and lattice distortion takes place simultaneously. Even at temperatures close to 300 K, we can observe that magnetism is already driving the structure (**Figure 4** and **Figure S.167**). Changes in J_i values are a direct consequence of the structural distortion of the system and the angles that mediate the four super exchange pathways. By cooling down, the lattice parameter *a* increases as it also increases the value of J_1 in the whole set of Hubbard U values. This enhancement of the ferromagnetic coupling along this direction comes from the variation of Cr-Br-Cr (β) and Cr-S-Cr (α) (**Figure S.168**). From experimental data we can observe that β=88.10° and α = 94.90° and they get larger progressively with decreasing temperature, reaching the saturation point at T = 40 K, and thus being β = 88.28° and α = 95.05° in the range 10 K < T < 40 K. The compression of the system along *b* results in a decrease in the Cr-S-Cr angle (δ) along this direction. From experimental data we can extract that by decreasing temperature it also follows a continuous trend and moves from 158.27° at 260 K to 158.04° at the saturation temperature T* (**Figure S.168**). As the lattice parameter *b* is compressed, δ moves further away from an antiferromagnetic behavior, and thus enhancing its ferromagnetic coupling as it is shown by the evolution of J_3 for the whole set of Hubbard U. Finally, elongation of *a*, and the compression of both *b* and *c* have a direct influence in the change of the Cr-S-Cr angle along c (γ). This angle

varies continuously from 97.32˚ at 260 K to 97.38˚ at T* and keeping it constant below it and to 10 K (Fig. S168). The evolution of J_1, J_2 and J_3 with respect to the angles (α, β, γ, δ) along the different super exchange pathways is reported in **Figure S.169**, showing a clear linear tendency that is not dependent on the choice of Hubbard U in the range 3-5 eV.

To further rationalize these findings, we performed a structure optimization for both a nonmagnetic and ferromagnetic configuration (see **Table S.5**). The optimized FM calculation leads to lattice parameters a = 3.54 and b = 4.73 Å, which corresponds to an enhancement of *a* and a compression of *b* from the experimental lattice parameters at 300 K (a = 3.51 and b = 4.77 Å), following the trend reported by López-Paz *et al.*[10] On the other hand, the nonmagnetic configuration provides a compression of both axes (a = 3.34 and b = 4.53 Å). Furthermore, the distance Cr-Cr for the FM configuration is 3.54, 3.61 and 4.73 Å, for first-, second- and third-neighbors, respectively, which agrees well with the experimental distances of 3.51, 3.58 and 4.77 Å. This kind of behavior has already been observed in other chromium-based magnetic materials linked by sulfur atoms.[22,23]

Table S.5.- Lattice parameters in Å and angles mediating the four different super-exchange paths (α, β, γ, δ) for nonmagnetic (NM) and ferromagnetic (FM) optimized structures.

	NM structure	FM structure
a (Å)	3.34	3.54
b (Å)	4.57	4.73
α (º)	92.98	95.66
β (º)	80.16	88.94
γ (º)	83.65	97.48
δ (º)	161.50	157.61

5.- References.

1.	Klein, J. *et al.* Atomistic spin textures on-demand in the van der Waals layered magnet CrSBr. *arxiv 2107.00037* (2021).

2.	Beck, J. Uber Chalkogenidhalogenide des Chroms Synthese, Kristallstruktur und Magnetismus von Chromsulfidbromid, CrSBr. *Zeitschrift fur Anorg. und Allg. Chemie* **585**, 157–167 (1990).

3.	Dolomanov, O. V., Bourhis, L. J., Gildea, R. J., Howard, J. A. K. & Puschmann, H. OLEX2 : a complete structure solution, refinement and analysis program. *J. Appl. Crystallogr.* **42**, 339–341 (2009).

4.	Telford, E. J. *et al.* Layered Antiferromagnetism Induces Large Negative Magnetoresistance in the van der Waals Semiconductor CrSBr. *Adv. Mater.* **32**, 2003240 (2020).

5.	Göser, O., Paul, W. & Kahle, H. G. Magnetic properties of CrSBr. *J. Magn. Magn. Mater.* **92**, 129–136 (1990).

6.	Zhang, J. *et al.* Magnetoelastic coupling in the incommensurate antiferromagnetic phase of FeOCl. *Phys. Rev. B - Condens. Matter Mater. Phys.* **86**, 1–5 (2012).

7.	Schönleber, A. *et al.* Phase transition, crystal structure, and magnetic order in VOCl. *Phys. Rev. B - Condens. Matter Mater. Phys.* **80**, 1–7 (2009).

8.	Shaz, M. *et al.* Spin-Peierls transition in TiOCl. *Phys. Rev. B - Condens. Matter Mater. Phys.* **71**, 3–6 (2005).

9.	Angelkort, J., Wölfel, A., Schönleber, A., Van Smaalen, S. & Kremer, R. K. Observation of strong magnetoelastic coupling in a first-order phase transition of CrOCl. *Phys. Rev. B - Condens. Matter Mater. Phys.* **80**, 1–6 (2009).

10.	López-Paz, S. A. *et al.* Dynamic Magnetic Crossover at the Origin of the Hidden-Order in van der Waals Antiferromagnet CrSBr. *arxiv 2203.11785* 1–12 (2022).

11.	Boix-Constant, C. *et al.* Out-of-Plane Transport of 1T-TaS 2 /Graphene-Based van der Waals Heterostructures. *ACS Nano* **15**, 11898–11907 (2021).

12.	Huang, B. *et al.* Layer-dependent ferromagnetism in a van der Waals crystal down to the monolayer limit. *Nature* **546**, 270–273 (2017).

13.	Telford, E. J. *et al.* Coupling between magnetic order and charge transport in a two-dimensional magnetic semiconductor. *Nat. Mater.* (2022) doi:10.1038/s41563-022-01245-x.

14.	Wu, F. *et al.* Quasi-1D Electronic Transport in a 2D Magnetic Semiconductor. *Adv. Mater.* 2109759 (2022) doi:10.1002/adma.202109759.

15.	Klein, D. R. *et al.* Enhancement of interlayer exchange in an ultrathin two-dimensional magnet. *Nat. Phys.* **15**, 1255–1260 (2019).

16.	Boix-Constant, C., Mañas-Valero, S., Córdoba, R. & Coronado, E. Van Der Waals Heterostructures Based on Atomically-Thin Superconductors. *Adv. Electron. Mater.* **7**, 2000987 (2021).

17.	Bedoya-Pinto, A., Prima-García, H., Casanova, F., Coronado, E. & Hueso, L. E. Spin-Polarized Hopping Transport in Magnetically Tunable Rare-Earth Quinolines. *Adv. Electron. Mater.* **1**, 1500065 (2015).

18.	Peng, S. *et al.* Metal-Contact-Induced Transition of Electrical Transport in Monolayer MoS 2 : From Thermally Activated to Variable-Range Hopping. *Adv. Electron. Mater.* **5**, 1900042 (2019).

19.	He, X., Helbig, N., Verstraete, M. J. & Bousquet, E. TB2J: A python package for computing magnetic interaction parameters. *Comput. Phys. Commun.* **264**, (2021).

20.	Scheie, A. *et al.* Spin Waves and Magnetic Exchange Hamiltonian in CrSBr. *Adv. Sci.* **2202467**, 2202467 (2022).

21.	Yang, K., Wang, G., Liu, L., Lu, D. & Wu, H. Triaxial magnetic anisotropy in the two-dimensional ferromagnetic semiconductor CrSBr. *Phys. Rev. B* **104**, 144416 (2021).

22.	Pokharel, G. *et al.* Negative thermal expansion and magnetoelastic coupling in the breathing pyrochlore lattice material LiGaCr4 S8. *Phys. Rev. B* **97**, 1–8 (2018).

23.	Rasch, J. C. E. *et al.* Magnetoelastic coupling in the triangular lattice antiferromagnet CuCrS2. *Phys. Rev. B - Condens. Matter Mater. Phys.* **80**, 1–7 (2009).